The University Of Sheffield.

Development of lithium rich, high nickel content cathodes to increase energy density of lithium-ion batteries

Xiaoqun Shi

May 2025

Registration No:200207423

Supervisor: Prof. Serena Cussen
Prof. Derek Sinclair

This dissertation is submitted for the degree of Master of Philosophy.

Table of Contents

Acknowledgements

I express my gratitude to my supervisor team, consisting of Prof. Serena Cussen, Prof. Derek Sinclair and other considerate team members, including Dr. Sam Booth, Dr. Innes McClelland, Dr. Enrique Sancheze Perez, Dr. Beth IJ Johnston, Katja Kress, and Dr. Misbah Mumtaz. Their assistance and support were vital in enabling me to successfully finish this thesis.

I especially value the Faraday FutureCat project, since being a member of it provides me with several opportunities to engage with other researchers and receive assistance from Dr. Ashok Menon, Jiayi Cen, and other exceptional researchers.

Lastly, I am grateful to my parents for their unwavering personal and financial assistance, which enabled me to pursue my education in Sheffield.

Abstract

Nickel-rich cathodes are anticipated to function as essential components for high-capacity lithium-ion batteries. Though it normally results in more complicated synthesis conditions, increasing the Ni content can substantially enhance the energy density, hence restricting its development. This study presents a straightforward one-step solid-state procedure for synthesising Li-rich and Ni-rich (Li_2NiO_3) materials. The synthesis conditions were thoroughly investigated and analysed. The study revealed that the synthesis circumstances had a significant influence on the electrochemical performance, especially the calcination temperature.

In addition, the study utilises a straightforward microwave-assisted approach. The products obtained by synthesis were analysed using X-ray diffraction, electron microscopy, and galvanostatic electrochemistry. When compared to the original Li_2NiO_3, the Li_2NiO_3 that was exposed to microwaves exhibited a 20% increase in capacity after undergoing 100 cycles at a rate of C/5.

Abbreviations

Li	Lithium
LCO	Lithium cobalt oxide
LNO	Lithium nickel oxide
NMC	$LiNi_xMn_yCo_zO_2$
OCV	Open circuit voltage
DMC	Dimethyl carbonate
EC	Ethylene carbonate
EDX	Energy dispersive X-ray spectroscopy
EVS	Electric vehicles
GCPL	Galvanostatic cycling with potential limitation
ICSD	Inorganic Crystal Structure Database
LIB	Lithium ion battery
NCA	Lithium nickel cobalt aluminium oxide
NMC	Lithium nickel manganese cobalt oxide
PVDF	Polyvinylidene fluoride
CV	Cyclic voltammetry
LFP	Li1–xFePO4
PXRD	Powder X-ray diffraction
SEM	Scanning electron microscopy
BSE	Backscattered electrons
SE	Secondary electrons
ICP-OES	Inductively Coupled Plasma Optical Emission spectroscopy
RT	Room temperature
SEI	Solid-electrolyte interface
TM	Transition metal
dQ/dV	Differential capacity analysis
FWHM	Full width at half maximum
MW	Microwave
NRL	Nickel-rich layered cathode oxide

Chemicals

$LiOH \cdot H_2O$, Sigma Aldrich, ≥98%

$Ni(OH)_2$, Sigma Aldrich, ≥99%

NMP, Alfa Aesar, ≥99%

Super C65, Sigma Aldrich

PVDF, Sigma Aldrich

$LiPF_6$, BASF

Li Sigma Aldrich, ≥99.9%

Separator, Celgard

CR2023, Cambridge Energy Solutions

Chapter 1

Introduction

1.Introduction

Energy storage systems that are reliable and effective are desperately needed as we move into the twenty- first century due to the explosive growth of portable electronics and information technologies. Furthermore, in recent years, exhaust gas from conventional internal combustion vehicles has been the primary source of PM 2.5(Particulate matter with aerodynamic diameter smaller than 2.5 μm , also known as fine particulate matter, is a major air pollutant with significant health and environmental impacts.). People must continually look for reliable sources of sustainable and clean energy because fossil fuels and coal are gradually running out. As a result, lithium-ion batteries have become the face of green energy and secondary batteries.

Advancements in energy storage devices and materials are crucial for the transition from diesel or petrol engines to more environmentally friendly electric vehicles, playing a significant role in addressing the urgent climate crisis. Energy storage markets have seen significant growth since the introduction of rechargeable lithium-ion batteries in 1991 by Sony. This breakthrough led to a revolution in the portable electronics industry and paved the way for the increasing adoption of electric vehicles in the transportation sector.[1]

There are still obstacles that need to be overcome in lithium-ion batteries to assure their increased use in electric vehicles, especially with consumer concerns about the limited driving range and high cost. Significant research efforts are now focused on enhancing energy and power densities, optimising battery efficiency, addressing supply-chain limitations, ensuring safety, and improving the recycling of battery packs. Cathodes with a high nickel content offer an advantageous prospect due to their ability to produce greater energy densities and reduced costs by eliminating the need for costly and harmful cobalt. Cathode active materials (CAMs) with higher nickel content

have gained more interest for electric vehicle (EV) applications. This is because they are cheaper, more readily available, and more abundant compared to cobalt.

These CAMs are typically in the form of lithium nickel-manganese-cobalt (NMC) or lithium nickel-cobalt-aluminum (NCA) oxide CAMs.[2] Modern nickel-rich cathodes, which are considered the most advanced, often contain a high proportion of nickel, often surpassing 80%. These cathodes belong to the NMC/NCA family, with $LiNiO_2$ (LNO) being the purest form of nickel-rich cathode that has gained significant attention.

In the following sections, we will examine the fundamental principles behind the operation of lithium-ion batteries, with a specific emphasis on the current status of the cathode materials. The main aim of this project is to advance the development of cathodes with a high nickel content.[3] Specifically, the focus is on creating stable cathodes with a high nickel content that are rich in lithium.

1.1 Introduction to lithium-ion batteries (LIBs)

Lithium-ion batteries (LIBs) function as energy storage devices by converting chemical energy into electrical energy, with the initial chemical energy stored in the materials comprising the electrodes. These electrodes typically consist of crystalline materials, where redox reactions facilitate the conversion of chemical energy into electrical energy.[4] This principle, involving energy conversion through redox reactions, is common across various battery technologies, including lead-acid batteries, nickel-metal hydride (Ni-MH), and nickel-cadmium (Ni-Cd) batteries, which are well-suited for high-power applications such as power tools.[4]

However, LIBs offer significantly higher energy densities compared to earlier battery technologies, as illustrated in Fig1.1. Their superior volumetric energy density (measured in Wh L^{-1}) and gravimetric energy density (measured in Wh kg^{-1}) enable the production of smaller and lighter batteries, a key attribute of advanced energy storage systems and a primary driver of LIBs' widespread adoption and popularity.[5]

These enhanced energy densities stem from the unique properties of lithium ions, which give LIBs their name. Lithium ions are small, lightweight, and highly electropositive, with a low Li^0/Li^+ redox potential of -3.04 V versus the standard hydrogen electrode. These characteristics combine to deliver higher specific capacities and operating voltages compared to older battery technologies. The product of specific capacity and operating voltage ultimately results in the high energy storage capabilities of LIBs, making them a cornerstone of modern energy storage advancements.

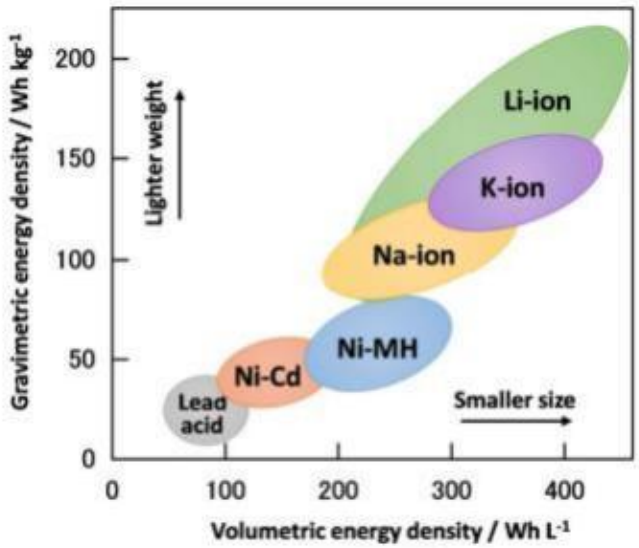

Fig1.1 Comparison of the gravimetric and volumetric energy density of batteries. Reprinted with permission from ref 5.Copyright 2018 John Wiley and Sons.

Since their commercialization, lithium-ion batteries have become ubiquitous in modern life. Global policies are now more focused than ever on reducing greenhouse gas emissions as well as the adaptation and financial aspects accompanying such efforts with the signing of the Paris Agreement by 195 United Nations member states in 2016.[6] Larger-scale applications such as EVs and stationary energy storage have emerged as excellent opportunities for advancements in lithium-ion battery technology. This is reflected in the growth of the LIB market from 2006 to 2016, approximately doubling every five years with new market growth driven by demand from electric vehicles and stationary energy applications, as shown in Fig 1.2.[7] The global LIB market is projected to experience substantial growth, with its valuation anticipated to rise from USD 70.7 billion in 2023 to

approximately USD 307.8 billion by 2032[8], reflecting a compound annual growth rate (CAGR) of 18.3% over the forecast period spanning 2023 to 2033. This robust expansion underscores the increasing reliance on LIBs across a wide range of industries and applications. [8,9] These larger-scale applications, particularly in the EV sector, have provided a significant impetus for the development of higher energy density systems.

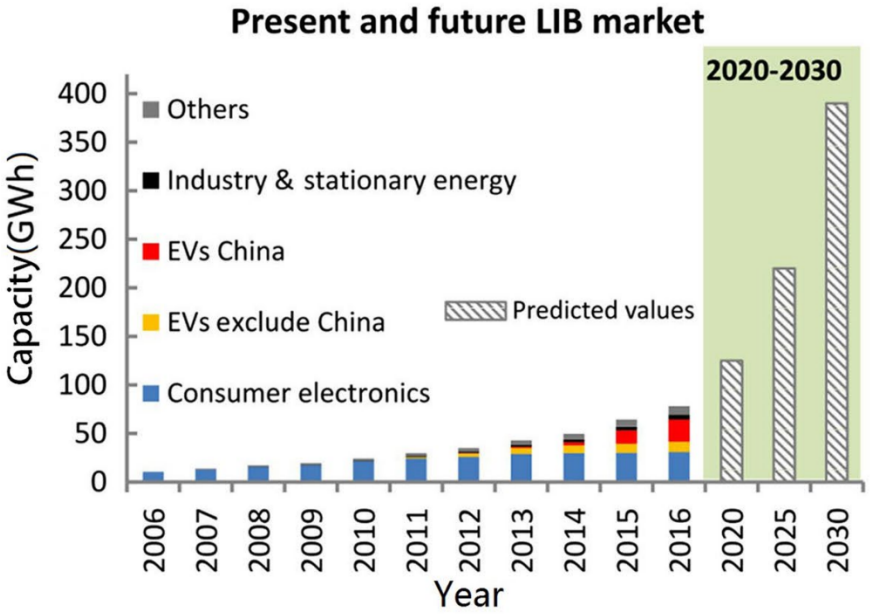

Fig1.2 The current and projected future market share of lithium-ion battery (LIB) technologies and their capacity spans several key sectors, including consumer electronics, electric vehicles (EVs), industrial applications, stationary energy storage (large-scale storage), and miscellaneous other uses. Reprinted with permission from ref 7. Copyright 2019, Springer Nature Limited.

LIBs have become a fundamental component of contemporary technology, playing a pivotal role in powering devices such as smartphones, laptops, EVs, and renewable energy storage systems. The high market demand for LIBs is driven by their exceptional energy storage capacity relative to their compact size, as well as their ability to undergo numerous charge-discharge cycles without significant degradation. These characteristics not only enhance their efficiency but also render them highly adaptable to diverse applications, solidifying their position as a critical technology in the transition toward sustainable energy solutions.[10] For EVs to appeal to the majority of consumers,

they must offer characteristics that are at least as good as, if not superior to, traditional internal combustion engine vehicles. For instance, current LIB technology for EVs faces issues related to cost, range, charging speed, lifespan, reliability, and limited charging infrastructure. Many of these challenges can be addressed through increased research and development efforts, which will inevitably reduce costs, while material development can deliver safer and more reliable batteries with higher energy and power densities, as well as longer lifespans.

1.2 Working principles of lithium-ion batteries

A LIB comprises several key components, including the cathode, anode, a separator, electrolyte, current collectors, and a casing. As a form of secondary battery technology, LIBs leverage the reversibility of redox reactions, enabling them to be repeatedly discharged and recharged during operation. This characteristic not only allows for multiple usage cycles but also significantly extends the battery's operational lifespan. The fundamental mechanism of LIBs relies on the reversible intercalation and deintercalation of Li^+ ions within the primary electrode materials. To ensure optimal performance, the intercalation process should induce minimal structural alterations in the electrodes, thereby mitigating lattice strain and instability that could otherwise result in irreversible damage to the lattice structure.[10]

During the discharge process, when the battery is connected to an external circuit, Li^+ ions are released from the high-energy state of the anode and migrate through the Li^+ ions conductive electrolyte, typically composed of $LiPF_6$ salt dissolved in a carbonate-based solvent. These ions subsequently intercalate into the cathode, transitioning to a lower energy state. Concurrently, to preserve charge neutrality, electrons are extracted from the anode alongside the Li^+ ions. These electrons, acting as negative charge carriers, traverse the external circuit to the cathode, generating the electrical current required to power connected devices. When the Li^+ ion reservoir in the anode is exhausted, the application of an external current initiates the reverse process, facilitating the recharging of the battery.

The discharge mechanism is illustrated in Figure 1.3, which depicts a LIB configuration featuring a lithiated graphite anode and a $LiCoO_2$ cathode—a design commonly employed in mobile phone batteries. This configuration exemplifies the practical application of LIB technology in consumer electronics.

The electrode reactions are as follows:

$$\text{Positive: } LiCoO_2 \longrightarrow xLi^+ + xe^- + Li_{1-x}CoO_2 \quad (1.1)$$

$$\text{Negative: } xLi^+ + xe^- + 6C \longrightarrow Li_xC_6 \quad (1.2)$$

$$\text{Overall: } LiCoO_2 + 6C \longrightarrow Li_xC_6 + Li_{1-x}CoO_2 \quad (1.3)$$

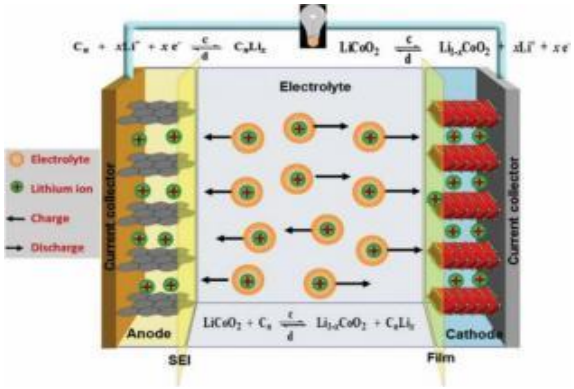

Fig.1.3 Schematic model of a rechargeable lithium-ion battery showing the ionic motion and (de)intercalation of lithium ions and the concurrent electron transport.Reprinted with permission from ref 2. Copyright 2016, Royal Society of Chemistry.

The energy density of a battery cell is governed by two key parameters: specific capacity and cell voltage. The specific capacity of an electrode material is primarily influenced by its mass and the maximum number of Li^+ ions that can be reversibly extracted or inserted per formula unit, which directly corresponds to the number of electrons available to participate in the external circuit. The theoretical specific capacity, denoted as $Q_{theoretical}$ and expressed in milliampere-hours per gram

(mAh g^{-1}), can be calculated using Equation 1.4. In this equation, *n* represents the number of electrons transferred (equivalent to the number of Li^+ ions) per formula unit during the discharge process, *F* is the Faraday constant (96485 coulombs per mole, C mol^{-1}), and *Mw* is the molecular weight of the electrode material. The factor 3.6 is included to convert the units from seconds-amperes per gram (sA g^{-1}) to milliampere-hours per gram (mAh g^{-1}).

$$Q_{theoretical=\frac{nF}{M_{W\times 3.6}}} \quad (1.4)$$

From the equation presented, it is evident that enhancing the theoretical capacity of an electrode material can be achieved through two primary approaches: reducing the molecular weight (*Mw*) of the electrode or increasing the number of Li^+ ions that can be accommodated per formula unit. Additionally, there is growing interest in exploring alternative multivalent cations, such as Al^{3+} as potential substitutes for Li^+ ions.[11] In such systems, a single multivalent cation can facilitate the transfer of two electrons, thereby maintaining charge neutrality while potentially increasing capacity. The cell voltage, on the other hand, is determined by the difference in electrochemical potential between the anode and cathode. This can be quantified using Equation 1.5, where V represents the open-circuit potential, μA and μC denote the chemical potentials of lithium in the anode and cathode, respectively, and *e* is the elementary charge of an electron.[12] This relationship highlights the direct dependence of cell voltage on the intrinsic electrochemical properties of the electrode materials.

$$V = \frac{\mu A - \mu C}{e} \quad (1.5)$$

By examining Equation 1.5, it becomes clear that achieving a high cell voltage requires the chemical potential of the cathode (μC) to be as low as possible, corresponding to a low-energy state, while the chemical potential of the anode (μA) must be as high as possible, representing a high-energy state. However, optimizing cell voltage is not solely a matter of selecting electrode materials with the largest possible energy gap. The stability window of the electrolyte plays a critical role and must be

carefully considered.[13,14] The electrolyte's ability to remain stable within a specific voltage range is a key factor that cannot be overlooked, as exceeding this window can lead to decomposition or other undesirable reactions, ultimately compromising the battery's performance and safety.

1.3 Routes to high energy density batteries

Enhancing the energy density of LIBs is a pivotal objective in advancing energy storage technologies. Energy density, defined as the energy stored per unit mass or volume, is fundamentally determined by the capacity and voltage of electrode materials, as well as the overall battery design. The specific capacity of an electrode material, which refers to the amount of charge it can store per unit mass (typically measured in milliampere-hours per gram, mAh g^{-1}), is a critical factor. To improve energy density, it is essential to develop electrode materials with higher specific capacities.

Conventional cathode materials such as $LiCoO_2$[15] (140 mAh g^{-1}) and $LiFePO_4$ [16](170 mAh g^{-1}) exhibit relatively low specific capacities. Transitioning to high-capacity materials, such as nickel-rich layered oxides (e.g., $LiNi_{0.8}Co_{0.1}Mn_{0.1}O_2$, ~200 mAh g^{-1})[17] or lithium-rich layered oxides (e.g., $xLi_2MnO_3 \cdot (1\text{-}x)LiMO_2$, >250 mAh g^{-1})[18], can significantly enhance energy density. These materials leverage multiple redox reactions, including transition metal redox (e.g., Ni^{2+}/Ni^{4+}) and oxygen redox activity, to store more charge. Traditional graphite anodes have a theoretical capacity of 372 mAh g^{-1}. Replacing graphite with high-capacity alternatives such as silicon (Si, ~4200 mAh g^{-1})[19] or lithium metal (Li, ~3860 mAh g^{-1})[20] can substantially increase energy density. For instance, silicon forms alloys with lithium to produce Li-Si compounds, enabling significantly higher lithium storage compared to the intercalation mechanism of graphite.

The energy density of a battery is directly proportional to its operating voltage (Equation1.6, where E is energy, Q is capacity, and V is voltage).

$$E = Q \times V \tag{1.6}$$

Therefore, increasing the voltage difference between the cathode and anode can significantly enhance energy density. Developing cathodes with higher redox potentials, such as $LiNi_{0.5}Mn_{1.5}O_4$

[21](4.7 V vs. Li/Li^+) or $LiCoPO_4$ [22](4.8 V vs. Li/Li^+), can elevate the overall cell voltage. However, this requires electrolytes with wider electrochemical stability windows to prevent decomposition at high voltages. Using anodes with lower redox potentials, such as lithium metal (0 V vs. Li/Li^+) or lithium titanate ($Li_4Ti_5O_{12}$, 1.55 V vs. Li/Li^+)[23], can also increase the cell voltage. Nevertheless, lithium metal anodes face challenges related to dendrite formation and safety concerns.

Materials capable of multi-electron redox reactions can store more charge per formula unit, thereby increasing specific capacity. Cathodes like sulfur (S) and anodes like silicon (Si) undergo multi-electron reactions. For example, S reacts with lithium to form Li_2S, involving a two-electron transfer per atom, resulting in a high theoretical capacity of 1675 mAh g^{-1}.[24] Lithium-rich layered oxides utilize both transition metal and oxygen redox reactions, enabling the extraction of multiple lithium ions per formula unit and significantly enhancing capacity.

Nickel-rich layered oxides, such as $LiNi_{0.8}Co_{0.1}Mn_{0.1}O_2$ (NCM811) and $LiNi_{0.8}Co_{0.15}Al_{0.05}O_2$ (NCA)[25,26], have garnered attention due to their high specific capacities and relatively high operating voltages. The theoretical capacity of these materials is directly linked to the redox activity of nickel (Ni^{2+}/Ni^{4+}), which provides a higher capacity contribution compared to cobalt (Co^{3+}/Co^{4+}) and manganese (Mn^{3+}/Mn^{4+}). The increased nickel content enhances the material's capacity, as nickel can deliver more electrons per formula unit during charge-discharge processes. Additionally, the concept of lithium-rich layered oxides ($Li_{1+x}M_{1-x}O_2$, $0 < x \leq 0.33$)[27] offers new possibilities for increasing capacity through additional anion redox activity.

Despite the theoretical promise of high-nickel lithium-rich oxides, several challenges must be addressed to fully realize their potential. These include stabilizing oxygen redox activity, preventing cation mixing, and mitigating voltage hysteresis. Future research should focus on understanding the fundamental mechanisms governing the electrochemical behavior of these materials, particularly the interplay between nickel and oxygen redox processes, to design high-performance cathodes for next-generation LIBs.

In summary, the development of high-nickel lithium-rich oxides represents a promising pathway to achieving higher energy densities in LIBs. By leveraging the synergistic effects of high nickel and lithium content, these materials offer a means to overcome the limitations of conventional cathode materials and meet the growing demand for advanced energy storage solutions.

1.4 Exploration of cathode materials

The main challenges facing LIBs remain their high cost and the irreversible capacity degradation of the positive electrode under high-voltage operation. Enhancements in the utilization of cathode materials such as $LiNi_{1/3}Co_{1/3}Mn_{1/3}O_2$, $LiMn_2O_4$, $LiFePO_4$ are expected to play a pivotal role in reducing the cost of lithium-ion batteries.[3,4,28] In addition, the low weight of lithium, along with its high electropositivity, provides benefits over previous secondary battery technologies in terms of energy-to-mass ratio and energy-to-volume ratio, as shown in Figure 1.4.[28,29]

LIBs are composed of a cathode (positive electrode), an anode (negative electrode), a separator, and an electrolyte. A separator physically isolates the positive and negative electrodes to prevent short-circuiting. The electrolyte functions as an ionic conductor, enabling the shuttling of lithium ions between them during charge and discharge cycles.[30,31]

Figure 1.4 presents a comparative chart that displays the capacity of several positive and negative electrode materials, as well as their potential in relation to lithium (versus Li/Li^+). It is evident from the figure that the positive electrode material has a significantly lower specific capacity than the negative electrode. The electrochemical potential between cathode materials and lithium is significantly greater than that of other negative electrodes. This characteristic plays a crucial role in determining the energy density of lithium-ion batteries, as it is strongly linked to the cathode material.[29]

Diffusion dynamics of lithium ions and electron transport capabilities are involved in the charging and discharging processes of lithium-ion batteries. Li^+ ions typically migrate more quickly in graphite negative electrodes in organic electrolytes. By contrast, the positive electrode typically

consists of a semiconductor material that contains transition metal lithium oxide and has a relatively low lithium ion diffusion coefficient.[30] The positive electrode material thus becomes the deficit of the overall electrochemical power of the lithium-ion when taking the rate control principle in electrochemical reactions into consideration. The cathode material often constitutes the most expensive and heaviest component of lithium-ion batteries, making it the primary factor influencing their performance from a materials perspective. Additionally, as the electrolyte decomposes at the limiting potential, a solid electrolyte interface (SEI) forms on the electrode surface. This process consumes Li^+ ions within the system, leading to irreversible capacity losses during charge and discharge cycles. The cathode material also significantly contributes to capacity degradation. Therefore, the development of high-performance cathode materials is crucial for enhancing the electrochemical performance of lithium-ion batteries.[32–34]

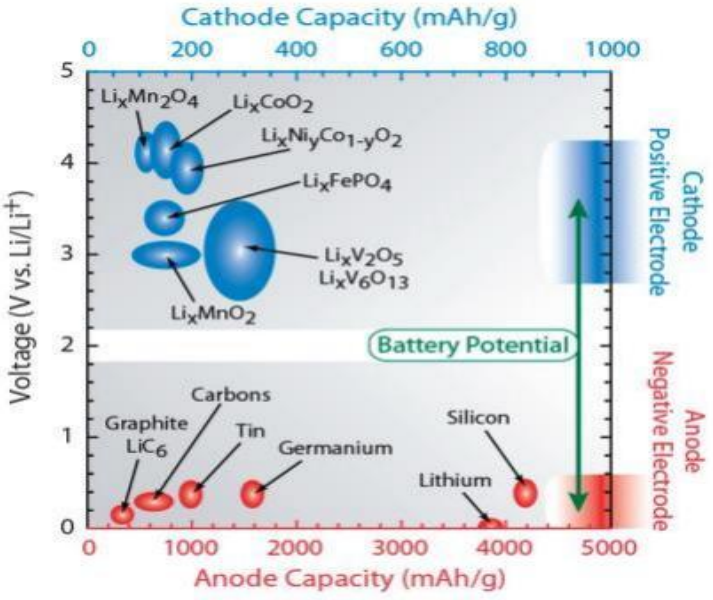

Fig1.4 Diagram showing the lithium-ion capacity and electrochemical reduction potentials related to lithium metal for conventional anode (red axis) and cathode materials (blue axis). Reprinted with permission from ref 29. Copyright 2021, under Creative Commons CC BY 4.0 license.

1.5 Cathode Materials for LIBS

Since the cathode material is the only source of lithium ions in the battery system, it usually needs to fulfil the following requirements.[35–37] The Fermi level and the potential energy of lithium-ion are minimised. The cathode materials should be well-compatible with the electrolyte within the designated voltage range.[36] The material undergoes minimal structural change during the charge and discharge process (the deintercalation of lithium ions), allowing for the reversible deintercalation of the greatest number of lithium ions.[37] The material demonstrates a notably fast lithium-ion diffusion rate, which is indicative of superior electronic and ionic conductivity. Furthermore, it is essential for cathode materials to exhibit outstanding thermal stability and to be feasibly synthesized at a cost-effective price point. In light of these considerations, researchers have conducted extensive investigations.

After decades of extensive research and experimentation, several materials have emerged as prominent cathode candidates or hold significant potential for future exploration. These materials can be classified into three distinct categories based on their structural configurations: one-dimensional tunnel structures, exemplified by olivine-type lithium iron phosphate ($LiFePO_4$)[38]; two-dimensional layered materials, such as lithium cobalt oxide ($LiCoO_2$)[15] with an α-$NaFeO_2$-type structure; and three-dimensional framework structures, including spinel-type lithium manganate ($LiMn_2O_4$)[39]. Each category exhibits unique structural and electrochemical properties that make them suitable for various applications in energy storage systems.[40]

1.5.1 Olivine $LiMPO_4$ (M=transition metal) materials

Research on $LiMPO_4$ cathode materials dates back to the 1980s, but significant advancements in the development and investigation of these compounds have primarily occurred over the past two decades. Among the diverse range of cathode materials, $LiFePO_4$ first discovered by Goodenough and his team, has emerged as a highly promising candidate. In contrast to traditional transition metal oxides incorporating cobalt, nickel, or vanadium, $LiFePO_4$, as an iron-based material, presents notable

benefits, including lower environmental toxicity, cost-effectiveness, and the widespread natural abundance of iron. Furthermore, $LiFePO_4$ fulfils several essential criteria for lithium-ion battery cathodes: it supports reversible delithiation at a potential of 3.50 V relative to Li/Li^+ and boasts a high theoretical capacity of 170 mAh g^{-1}. Additionally, this compound is recognized for its eco-friendly properties and exceptional stability, even under extreme conditions such as overcharging or deep discharge.[41–43]

The predominant technique for producing $LiFePO_4$ is the solid-state approach, typically employing ball milling or manual mixing, followed by calcination in a tubular furnace under an inert atmosphere. In addition, pure $LiFePO_4$ can be obtained using sol-gel, hydrothermal, and other chemical processes.[16,38]

Figure 1.5 illustrates a typical olivine structure, $LiFePO_4$, which is part of the orthorhombic crystal system with Pnma space group. The unit cell characteristics of the material are as follows: a = 0.469 nm, b =1.033 nm, c = 0.601 nm.[38] Within the $LiFePO_4$ lattice, the tetrahedral spaces are filled by P atoms, constituting 1/8 of the available sites. Additionally, ½ of the available octahedral sites are occupied by metal ions (Li and Fe).[44] The FeO_6 octahedra are joined in a zigzag pattern on the 6c plane, with each octahedron sharing vertices with adjacent ones. This layer of transition metal octahedra has the ability to conduct electron transport. The LiO_6 octahedra are joined together by their edges in the direction of the 6-axis.[45]

Various opinions are held regarding the process of charging and discharging in $LiFePO_4$. Goodenough and his team claimed that the "L" type properties of its charge and discharge curve are attributable to a two-phase reaction. Thus, they suggested a model known as the "core-shell structure".[41] Afterwards, using X-ray powder diffraction, Anderson and colleagues found $LiFePO_4$ and $FePO_4$ two phases during the deintercalation process of lithium ions in 2000.[46] In 2004, Srinivasan and colleagues proposed the "shrinking core" model, suggesting that the phase transformation process involves not only two distinct phases but also a partial solid solution region. According to this theory, during the initial stages of discharge, lithium-deficient phases (Li_yFePO_4)

are formed on the surface, which subsequently convert into lithium-rich phases ($Li_{1-x}FePO_4$) as the reaction progresses. Upon complete charging and discharging, the material ultimately reverts to the $LiFePO_4$ phase[47]. By 2006, Chen et al.[48] utilized high-resolution transmission electron microscopy (HRTEM) to study $LiFePO_4$-PO_4 flake crystals, identifying disordered regions within the ac plane and confirming that lithium-ion diffusion primarily occurs along the b-axis. In the same year, Lafont and coworkers conducted electron energy loss spectroscopy (EELS) to analyze the distribution of $LiFePO_4$ and $FePO_4$ phases within individual particles. Their findings did not detect a solid solution phase. However, since the experiments were not performed under in situ conditions, the possibility of a transient solid solution phase could not be conclusively ruled out.[49]

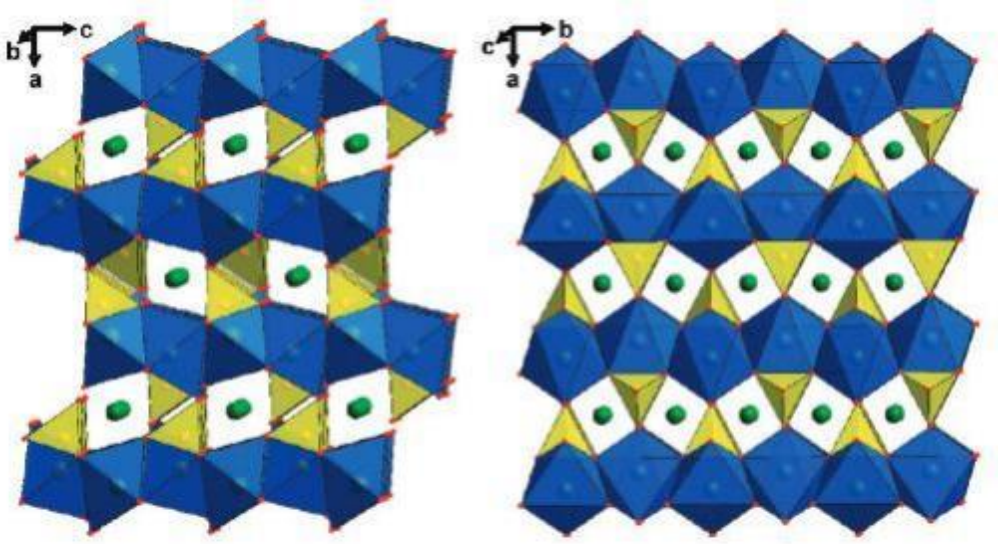

Fig1.5 The crystal structure of $LiFePO_4$, viewed (a) along the b-axis and (b) along the c-axis. The iron octahedra are shown in blue, the phosphate tetrahedra in yellow, and the lithium ions in green. Reprinted with permission from ref 44. Copyright 2012, Royal Society of Chemistry.

In 2011, Gu et al.,[45] discovered the occurrence of interlaced ion detachment in partly charged $LiFePO_4$ nanowires using spherical aberration-corrected annular bright field scanning transmission imaging technology. This discovery contradicts several prior theories of two-phase reactions, which assume a single- phase structure.[45] Subsequently, Suo[44] and colleagues discovered a meticulously arranged $LiFePO_4$/$FePO_4$ interface exhibiting a second-order structure once again,

this time in the $Li_{0.9}Nb_{0.02}FePO_4$ compound along the an axis direction. Additionally, they hold the belief that this particular structure represents one of the places where two phases interface. It can be classified as an intermediate phase or an intrinsic metastable phase. This extends the research on the reaction interface to include the coexistence of three phases: $LiFePO_4$, ordered structure, and $FePO_4$.[44] In 2012, Sun[50] and coworkers studied the formation mechanism of this second-order structure through density of state functional calculations, showing that the entire particle was mainly composed of $LiFePO_4$, $FePO_4$ and a small amount of "second-order" structure caused by kinetic limitations between the two phases. This structure is a thermodynamic metastable structure caused by lithium-ion transport dynamics.[50]

Although $LiFePO_4$ has excellent cycling performance and stability, it still suffers from some major shortcomings: First, low electron conductivity[51] and ion conductivity.[52] In addition, its apparent diffusion coefficient is only about 10^{-10}-10^{-15} cm^2 s^{-1}, resulting in low-rate performance.[52] Besides, the low energy density because of low working voltage, 3.5 V vs. Li/Li^+.[53]

Researchers have made effective attempts in three aspects: coating the material surface with activated carbon[54], ion-doping high-valence metal ions[55] and controlling particle size to improve electronic and ion conductivity.[56,57]

1.5.1 $LiMnPO_4$

Researchers have identified alternative olivine-type materials, such as $LiMnPO_4$[58], $LiCoPO_4$[39], and $LiNiPO_4$[59], to address the issue of $LiFePO_4$'s low energy density. Based on Mehwish et al. [59]'s research, the platform potential of $LiNiPO_4$ is 5.20 V, which indicates a high level of promise for the platform[58]. $LiMnPO_4$ and $LiCoPO_4$ have greater operating potentials compared to Li/Li^+ (4.10 V and 4.80 V, respectively), resulting in higher energy density.[39] Although $LiMnPO_4$ has higher operating potentials, its shortcomings are more prominent: it has worse electron and ion conductivity.[58,60] It also has a larger bandgap and worse rate performance.[61] In addition, it has a Jahn-Teller effect caused by Mn^{3+}.[62]

To address the aforementioned problems, researchers implemented modification techniques akin to those used for $LiFePO_4$. Wang et al. synthesised $LiMnPO_4$ nanocrystals using the polyol polymerization process. The material exhibited a specific capacity of 113 mAh g^{-1} at a 1 Crate and demonstrated stable cycling for 200 cycles, unaffected by the Jahn-Teller effect.[60] Chenet al. found that incorporating a small amount of Mg can change the volume change rate between the delithiated state and the lithium-inserted state from 9. 5% reduced to 7. 8%, and can also stabilize the delithiated phase of Jahn-Teller distortion.[63] One of the most ideal strategies is doping $LiMnPO_4$ with Fe. This structure can release an actual amount of electricity (160-165 mAh g^{-1}) that is close to the theoretical specific capacity (170 mAh g^{-1}) and has good rate performance.[64]

The extremely low electron and ion conductivities of the $LiMPO_4$ class compounds are determined by their inherent structural makeup. To some degree, this intrinsic flaw can be improved through the employment of nanosynthesis technology, high-valent metal ion doping, and conductive carbon material coating. Nevertheless, $LiFePO_4$ and similar materials face challenges in establishing a strong competitive position in the cathode market.

1.5.2 AB_2O_4 Spinel materials

Spinel lithium manganese oxide ($LiMn_2O_4$) has received much attention and has been commercialized early. In 1983, it was pioneered explored by Thackeray et al.[65] The theoretical capacity of this material is 148 mAh g^{-1}, the actual reversible capacity can reach to 100-120 mAh g^{-1}.[66] Since its creation, scientists have identified the following benefits: because the transition metal is entirely constituted of manganese and there is a plentiful supply of this element, the manufacturing cost of the metal is inexpensive. It is safer since its oxidation property is low and its decomposition temperature is high. Consequently, $LiMn_2O_4$ exhibits cheap cost, stability, and favourable electrical and lithium conductivity characteristics.[67]

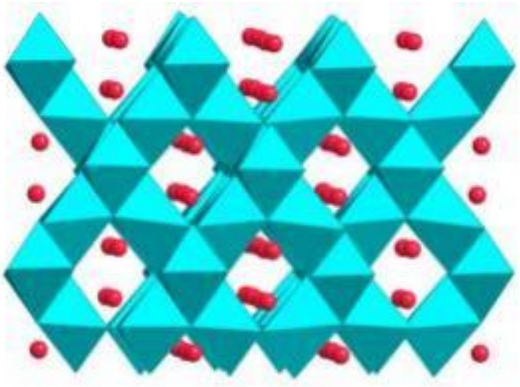

Fig1.6 The crystal structure of spinel $LiMn_2O_4$.(blue: transition metal ions; red: Li ions). Reprinted with permission from ref 68. Copyright 2015, Springer Nature Limited.

The solid-state method is the predominant technique used to synthesise $LiMn_2O_4$ with a spinel crystal structure. $LiMn_2O_4$ is classified as a member of the cubic crystal system, with a group structure denoted as Fd3m. Figure 1.6 demonstrates that Mn occupies 16d sites within the octahedra. However, 1/4 of these sites are found in the lithium layer, resulting in a 1/4 vacancy in this particular layer of Mn.[39] 1/8 of Li occupies the tetrahedral 8a position in the Li layer, which is connected with the empty octahedra in the Mn layer. The remaining empty tetrahedra are connected to the octahedra through a coplanar arrangement, forming a three- dimensional lithium-ion diffusion channel.[68] The oxygen atoms are located at the 32e position in the crystal lattice and are cubic close packed (ccp). It is worth mentioning that in the framework, the Mn^{3+} layer and the layer without Mn^{3+} are distributed in alternating layers between the ccp oxygen ions, and the distribution ratio is 3:1. Therefore, each layer can ensure that there is enough Mn^{3+} to stabilize the cubic stacking structure when Li^+ is delithiated, making the entire process reversible.[69]

$LiMn_2O_4$ undergoes a typical phase change reaction during its charging and discharging process. $Li_xMn_2O_4$ is given as an example to describe the description of the charging and discharging process.[70] When the value of x is between 0.1 and 0.5, Li is inserted into the γ-MnO_2 phase region. In this range, there is a coexistence of two phases, γ-MnO_2 and $Li_{0.5}Mn_2O_4$, and the corresponding electric potential platform is at 4 V.

When x is greater than 0.5, the insertion of Li^+ forms another pair of two-phase regions, $Li_{0.5}Mn_2O_4$ and $LiMn_2O_4$, at a voltage of around 3.90 V. Li^+ ions in the vicinity of 4 V can effectively preserve the cubic symmetry of the spinel structure and exhibit excellent cycling performance.[70,71]

Nevertheless, if the voltage of the discharge keeps decreasing, Li^+ ions will be placed into the 16c position of the vacant octahedra in the spinel structure at around 3.0 V, resulting in a distortion of the structure. The initial cubic symmetry of $LiMn_2O_4$ will undergo a transformation to a tetragonal symmetry, resulting in the formation of $Li_2Mn_2O_4$. Additionally, the valence state of Mn will shift from +3.5 to +3.0, leading to the occurrence of significant Jahn-Teller effects. This alteration in structure and valence state will result in a decline in cycle performance due to the development of surface cracks.[72]

1.6.3 $LiMO_2$ layered materials

$LiMO_2$ (M=Mn, Fe, Co, etc.) is a typical two-dimensional layered structure cathode material. It is mainly composed of lithium transition metal oxides with high redox potential. Most of the structures belong to the α- $NaFeO_2$ layered salt.[72,73]

1.5.3.1 $LiCoO_2$

Since Goodenough et al. first reported lithium cobalt oxide $LiCoO_2$ in 1980, this material has attracted much attention.[56] The theoretical capacity of $LiCoO_2$ is 274 $mAhg^{-1}$, while it can generally reversibly inserted 0. 5 Li in 2.5-4.2V vs.Li/Li^+, so the actual capacity is only 130-140 $mAhg^{-1}$.[57] $LiCoO_2$ crystallizes in a layered α- $NaFeO_2$ structur with space group of $R\bar{3}m$ consists of alternating layers of edge-sharing LiO_6 and CoO_6 octahedra stacked along the c-axis.

Nevertheless, the oxygen atoms are stacked and organised in various manners. The high-temperature synthetic phase is organised in a configuration that is a structure that is stable according to thermodynamics. The oxygen atoms are densely arranged in the (001) crystallographic direction of the ABCABC structure.[74]

On the contrary, the low temperature synthetic phase is an O2 array, which is a metastable structure. The arrangement order of O atoms along the (001) direction is ABACABAC.[75–77] During the electrochemical cycle, the rearranging of Co and O ions in various structural arrangements will result in the formation of new phases as the Li content changes.

Furthermore, apart from the insufficient availability of Co resources, the high cost, high toxicity, and poor actual specific capacity, another significant drawback of $LiCoO_2$ is its capacity attenuation. The reasons for oxygen loss, decomposition of electrolyte, and solubility of Co in conventional electrolyte occur when the amount of lithium removal surpasses 0.7 due to an unstable structure and the development of a lithium-poor phase.[15,78–80] To enhance the reversible and stable deintercalation of Li^+ from the layered Li_xCoO_2, techniques such as doping and coating are commonly employed. According to Cho et al., the application of metal oxides and phosphates as a coating can enhance the cycling performance of Li_xCoO_2.[81] ZrO_2 can mitigate the rise in volume during the charging process and enhance the upper limit voltage of lithium cobalt oxide (Li_xCoO_2), hence enhancing the stability of the battery cycle and increasing its reversible specific capacity to around 170 mAh g^{-1}.

Although researchers have currently invested a lot of energy in studying various modification, and even improving the reaction with by-product of electrolytic liquid.[63,82] Nevertheless, the use of stacked $LiCoO_2$ in large-scale energy storage is limited because of its exorbitant cost, severe toxicity, and inadequate safety measures.

1.5.3.2 $LiNiO_2$

Lithium nickel oxide ($LiNiO_2$) has also been listed as a reliable substitute of lithium cobalt oxide because of its relatively low cost, higher reversible specific capacity (200 mAh g^{-1}) and better environmental compatibility.[83]

The charge and discharge process of $Li_{(1-x)}Ni_{(1+x)}O_2$ is relatively complex, including three single-phase processes and three two-phase processes: H1 ($0<x<0.15$)↔H1+M($0.15<x<0.25$)↔M ($0.25<x< 0.5$)↔M+H2 ($0.5<x<0.57$)↔H2 ($0.5<x<0.68$)↔H2+H3 ($x<0.68$). H represents hexagonal crystal system, and M represents monoclinic crystal system.[84,85]

Nevertheless, achieving the stoichiometric composition of $LiNiO_2$ is challenging, especially when synthesised under high-pressure oxygen conditions. $LiNiO_2$ shares a similar layered structure with $LiCoO_2$, featuring alternating layers of Li and Ni atoms. However, due to the comparable ionic radii of Li^+ and Ni^{2+} , cation mixing often occurs, where some Ni occupies Li sites (and vice versa), leading to structural disorder. This interlayer mixing can impede Li-ion diffusion and negatively affectelectrochemical performance.

The compound produced using traditional preparation conditions typically exhibits non-stoichiometric characteristics and is known as $Li_{(1-x)}Ni_{(1+x)}O_2$. The instabilities of the Ni^{3+} ion, which are more likely to change into Ni^{2+} and have some Li^+ loss, are a major factor in the easy formation of non-stoichiometric lithium nickel oxide.[86] Owing to the identical effective ionic radii of Ni^{2+} and Li^+(Ni^{3+}= 0.56 Å, Ni^{2+} = 0.69 Å, Li^+ = 0.76 Å). Nickel ions with a charge of +2 have a greater tendency to occupy the 3b position, which is normally inhabited by lithium ions. As a result , it is quite likely for a crystal lattice to have a combination of different types of cation sites. [87] During the charging process, Ni^{2+} ions will undergo oxidation and become Ni^{3+} ions, which have a smaller ion radius. This change in ion size causes disorder in the occupation of Ni^{2+} and Li^+ ions, resulting in a decrease in the available space for some 3b positions. As a consequence, the diffusion of Li^+ ions within the structure is hindered. In addition, the chaotic occupation will also result in permanent decline in capacity throughout the initial cycle.[62]

Given the mentioned problems, the researchers attempted to substitute the Ni^{3+} ions with Co^{3+} ions in a material known as $LiNi_{(1-x)}Co_xO_2$.[88] This substitution aimed to enhance the material's resistance to oxidation and prevent the development of Ni^{2+}. A higher degree of structural stability can be achieved by adding a little quantity of Al to the material and slightly adjusting the Co and Ni ratios, resulting in $LiNi_{0.8}Co_{0.15}Al_{0.05}O_2$(NCA).[89] NCA has advanced towards commercialization due to its reduced cation mixing, increased thermal stability, and high specific capacity resulting from its 80% nickel concentration. Nevertheless, the safety concerns arising from the discharge of excessive O_2 have consistently been a significant issue.

1.5.4 High Nickel Cathode Materials

The nickel-rich layered cathode oxide (NRL) can be defined where the nickel component is equal to or more than 0.5. The NRL materials have a specific capacity of around 200 mAh g^{-1} and demonstrate excellent compatibility with the electrolyte. The energy density of NRL reaches 800Wh kg^{-1}, which is higher than that of $LiFePO_4$ and $LiCoO_2$.[88]

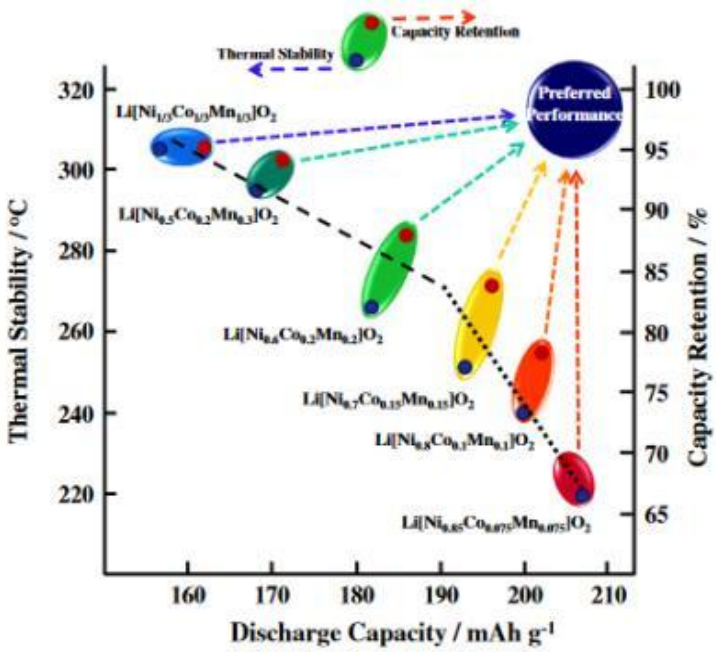

Fig1.7 A map of the relationships between discharge capacity, thermal stability and capacity retention of Li/Li[$Ni_xCo_yMn_z$]O_2. Reprinted with permission from ref 88. Copy right 2022, Royal Society of Chemistry.

From Fig1.7, with the increase of Ni content, the discharge ratio of NRL increases significantly but the thermal stability and cycle performance decrease sharply with the increase of Ni.[90] This behavior is closely related to the electronic structure, particularly the energy band configuration, shown with Figure1.8.

The high specific capacity of NRLs is believed to be associated with their electrical structure. Based on Figure 1.8, it can be observed that the position of Ni^{3+}/Ni^{4+} in the e.g. energy band, which overlaps with the O^{2-} section of the 2p energy band top, is lower than that of t_{2g} of Co^{3+}/Co^{4+}. This indicates that in Ni^{3+}/Ni^{4+}, there are less electrons available for delocalization. The

t_{2g} energy band of Co^{3+}/Co^{4+} largely overlaps with the O^{2-} top 2p energy band. Thus, the +4 valence state of Cobalt can only be observed when it surpasses the delithiation of 0.5 Li^{+} ions. This will unavoidably result in chemical instability and safety issues.[91]

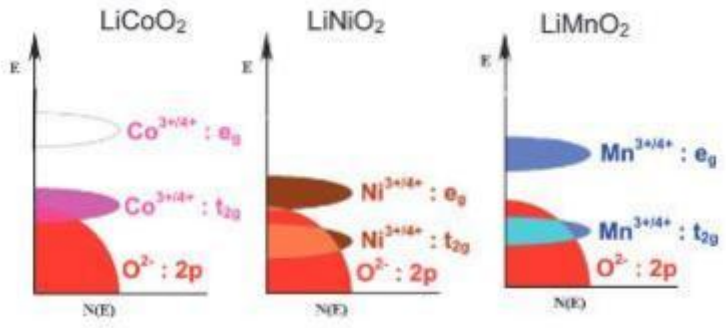

Fig1.8 Comparison of the energy diagrams of $LiCoO_2$, $LiNiO_2$, and $LiMnO_2$.[91] Reprinted with permission from ref 91. Copy right 2008, Royal Society of Chemistry.

On the contrary, the 4+ valence of Ni can be obtained relatively easily in the layered structure, and is accompanied by the escape of more available Li^{+} in the main structure and can obtain a specific capacity of nearly 200 mAh g^{-1}.[88]

Undoubtedly, nickel-rich layered (NRL) materials also face inherent limitations that demand urgent attention. A significant issue is the occurrence of "cation mixing," a phenomenon closely linked to the structural stability of these materials.[92,93] The NRL is a configuration consisting of layers arranged in an O3 type pattern, which is characteristic of a rhombohedral crystal structure. When observed from the [001] crystal axis, the material's stacking pattern is O-Li-O-TM-O-Li-O-TM-O.[84,94] Hence, the structure exhibits distinct TM point (3a) and Li point (3b). Indeed, in the face-centered cubic lattice, the Ni ion undergoes a transition from Ni^{3+} to Ni^{2+} rather than remaining as Ni^{3+} as predicted by the crystal field theory. This transition occurs because Ni^{3+} develops unpaired spin electrons in its orbit, resulting in unpaired spins.[95] As previously stated, the effective ionic radius of Ni^{2+} is 0.69 Å, which is comparable to the effective lattice radius of Li^{+} (0.76 Å). Consequently, Ni^{2+} ions tend to migrate and occupy the 3b sites within the lithium layer. When this mutual

displacement occurs, cation mixing propagates in a domino-like cascade. This disordered crystal phase significantly hinders Li^+ ion diffusion compared to the ordered structure, primarily due to the reduced interlayer spacing of metal elements and the blockage of lithium deintercalation pathways.[88] The rate performance of active materials decreases when the cation mixing increases due to the high activation energy barrier.[84]

1.5.5 Lithium-rich Cathode Materials

Lithium-rich materials are usually manganese based, represented by $xLi_2MnO_3 \cdot (1-x)\ LiMO_2$ ($0 < x < 1$, M = Ni, Co, Mn, Fe and other transition metals and their combinations).[18,27,96]

The lithium-rich material is a layered structure composed of two phases of $LiMO_2$ and Li_2MnO_3.[27,96,97] Among them, Li_2MnO_3 can also be expressed as Li $[Li_{1/3}M_{2/3}]\ O_2$[98] (such as Li $[Li_xM_{1-x}]O_2$ where M = Mn, x = 1/3), which belongs to the single space lattice group C2/m. Li_2MnO_3 adopts a layered structure in which Li layers alternate with transition metal (TM) layers containing a 2:1 ratio of Li:Mn. All Li atoms, including those in both the pure Li and mixed Li-TM layers, occupy octahedral sites.[96,99] The Li^+ ions are surrounded by six Mn^{4+} ions, resulting in the formation of a $LiMn_6$ superlattice structure.

During the initial charging process of lithium rich materials, such as $Li_{1.2}Ni_{0.2}Mn_{0.6}O_2$, there are two clearly defined voltage ranges between 2.0 and 4.8 V. An upward diagonal line separates the voltage range of 2.0 to 4.45 V, during which Ni^{2+} undergoes oxidation to Ni^{4+}, whereas the valence state of Mn^{4+} remains constant.[99] Accordingly, in the first charge of the CV curve, the oxidation process of $Ni^{2+/3+/4+}$ is represented by an oxidation peak around 4.0 V, whereas there is no oxidation peak of Mn near 3.5 V. Due to a difference in migration energy, with each unit of Li^+ having 3.00 eV less energy than the metal layer, Li^+ ions initially leave the octahedral site in the lithium layer to create vacancies.[18] Within the voltage range of 4.45 to 4.6 V, a distinct voltage plateau is observed, indicating the occurrence of the electrochemical activation process of the Li_2MnO_3 phase.

$(Li_2MnO_3 \rightarrow Li_2O + MnO_2)$[101] (1.7)

Li^+ is released from the lithium layer and the metal layer with O_2 oxidation, such as O^{2-}/ O^-or O^{2-}/ O^2. During the discharge process, the transition metal ions occupy the Li^+ vacancies in the bulk crystal lattice, preventing the leached Li^+ from returning to the lattice vacancies. This leads to the first permanent capacity loss.

Consequently, some pre-processing techniques can be employed to induce the activation of the Li_2MnO_3 phase. For example, Rossow etal.[99,102] subjected Li_2MnO_3 to acid treatment, which resulted in the interchange of Li^+ and H^+ ions. This caused a minor amount of Li_2O to be released, leading to the electrochemical activation of MnO_2 and thus lowering the initial irreversible capacity loss. Nevertheless, the acid treatment causes significant damage to the surface of the lithium-rich material, resulting in an unstable cycle performance.

On the other hand, the Mn^{4+} in the activated MnO_2 is reduced to Mn^{3+} [54] at $4.8 \sim 2.0$V, and participates in the electrochemical reaction of the next cycle, corresponding to the Mn redox peak on the CV curve.[102]

1.5.6 Lithium-rich Li_2NiO_3

Beyond $LiNiO_2$ (LNO), the Li-Ni-O phase diagram encompasses several other phases. Rock salt-type lithium nickel oxides with the general formula $Li_yNi_{1-y}O$ can be synthesized, where y is typically less than 0.3. As the value of y increases within the range of 0.3 to 0.6, a rhombohedral layered structure emerges, with LNO corresponding to y = 0.5. On the other hand, compositions with higher lithium content, up to approximately two-thirds, adopt a monoclinic structure. These structural variations are interrelated, as they all originate from the cubic close-packed (ccp) oxygen sublattice. At lower lithium concentrations, lithium and nickel cations are statistically distributed across the available sites. However, as the concentrations of lithium and nickel rise, they segregate into distinct layers to alleviate spatial constraints and optimize the structural arrangement. This results in a hexagonal layered structure ($R\bar{3}m$).[103] Finally, with further increase of y, the hexagonal lattice undergoes a monoclinic distortion, indicating a layered structure with a 2:1 honeycomb arrangement of Ni and Li cations. The most Li-rich member in this solid solution when y goes up to 2/3, $Li_{0.67}Ni_{0.33}O$, can also be written as Li_2NiO_3, emphasizing its isostructural properties with compounds such as Li_2MnO_3 (LMO), the theoretical capacity is around 225 mAh g^{-1}.[103]

Despite the limitations of the previous synthetic methods, which need high temperature and high pressure and are not suitable for large-scale production, a newly discovered synthesis approach that does not require high pressure has demonstrated potential for developing more straightforward ways. This solid-state synthesis still necessitates significant excess quantities of lithium and several lithium salts, however, the resultant product must undergo a washing process. Ultimately, this could result in the advancement of this compound. According to reports, the oxidation state of nickel in Li_2NiO_3 is 4+. Experimental data indicate that Li_2NiO_3 has the lowest conductivity compared to other members of the $Li_yNi_{1-y}O$ family.[78] However, it has also been illustrated that this compound is prone to oxygen deficiency, denoted as $Li_2NiO_{3-\delta}$ where $\delta < 0.135$, resulting in paramagnetism.[78] Therefore,

it is difficult to achieve a fully tetravalent Ni state, which is consistent with the fact that $Li_2NiO_{3-\delta}$ is not a fully insulating material but behaves as an n-type semiconductor.

Electron paramagnetic resonance (EPR) spectroscopy also confirms the presence of Ni^{3+} and Ni^{4+}.[79] Generally, it is difficult to prepare highly oxidised compounds because nickel (Ni) usually has an oxidation state of 3+ or lower. There are only a few compounds where Ni has an oxidation state higher than 3+, such as $BaNiO_3$, $PrNiO_3$, and $KNiIO_6$.[100,104] The existence of Ni^{4+} has been questioned by spectroscopic studies, which suggest that the oxidation state of Ni is actually lower than 4+. This is due to the highly hybridised nature of the Ni and O orbitals, indicating that the lower oxidation state of Ni is compensated by negatively charged oxygen anions (O^{n-}), where the value of n is between 1 and 2.[80–82,105] Li_2NiO_3 is isostructural with Li_2MnO_3 (LMO), a compound that is closely related to CAM and serves as an inactive building block to stabilise lithium and manganese phases, related to compositions such as $Li_{1.2}Mn_{0.54}Co_{0.13}$, and $Ni_{0.13}O_2$.[83–86] Owing to the above- mentioned factors as well as its ease of synthesis, LMO—where 4+ denotes Mn's favourable oxidation state in octahedral coordination—has been the subject of much research. Chemical and electrochemical studies have demonstrated that extracting lithium from LMO not only enhances the specific capacity of LIBs but also diminishes their reversibility.[87–89] The literature contains conflicting debates regarding the redox mechanism, which has recently been investigated using advanced techniques such as X-ray absorption near-edge structure (XANES), differential electrochemical mass spectrometry (DEMS) resonant, and inelastic X-ray scattering (RIXS). These studies have revealed that the removal of lithium during the initial charging process is not balanced by the oxidation of Mn beyond 4+ or by the reversible oxidation/reduction of oxygen within the solid material. Instead, it mostly consists of the permanent release of O_2 (and also CO_2), which is responsible for most of the reported capacity in LMO.[90] Therefore, cycling of Li_2MnO_3 leads to significant degradation of the crystal structure.

Li_2NiO_3 was initially discovered by Bronger and Migeonetal.[106,107] It is synthesised under strongly oxidising circumstances by either subjecting it to a high O_2 partial pressure or applying

high mechanical pressure. However, the non-scalable synthesis methods used to create Li_2NiO_3, limiting its commercial applicability.

Even if a new paper describes a low-pressure synthesis route that requires a significant amount of Li excess and multiple Li salts before solid-state synthesis can wash the product, it still provides a better approach and the opportunity to develop simpler pathways. As stated in Matteo's research, we may utilise a straightforward solid-state method to synthesise Li_2NiO_3 and analyse its crystal and electrical structure.[94,106,107]

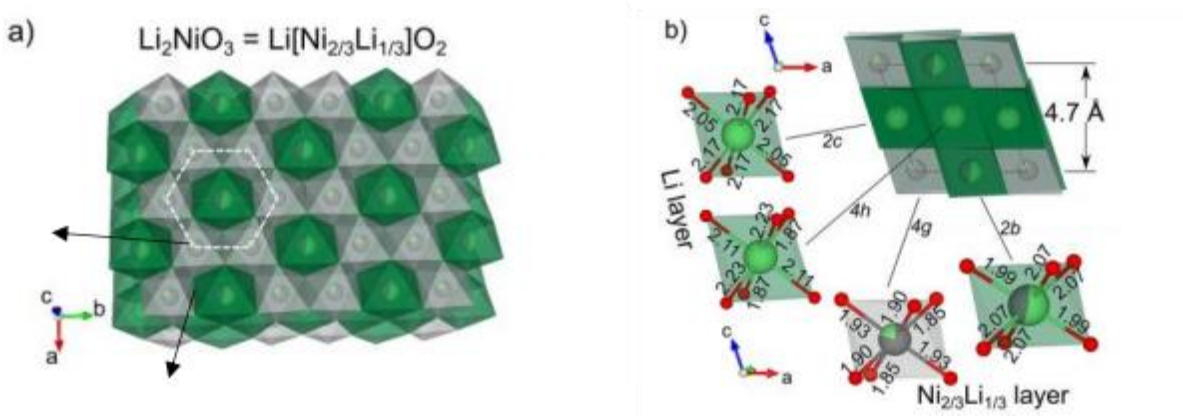

Fig 1.9 The crystal structure of Li_2NiO_3 viewed from different directions. Reprinted with permission from ref 103. Copyright 2020, American Chemical Society.

Li and $Ni_{2/3}Li_{1/3}$ layers are covered within a nearly cubic close-packed oxygen sublattice (see Fig1.9). Therefore, the difference between Li_2NiO_3 and $LiNiO_2$ is clear, $LiNiO_2$ is being built by alternating Ni and Li layers in analogous anion sublattice. However, the Li_2NiO_3 built with $Ni_{2/3}Li_{1/3}$ layers and coulombic repulsion are minimized because of a honeycomb ordering of larger Li^+ cations gathered around by smaller Ni cations (~1:2 ratio, Figure 1.9).[103]

1.5.7 Redox mechanism of Li_2MO_3 (M=transition metal) analogues

The high capacity of the lithium-rich material is resolved into redox of metal cations ($M^n \leftrightarrow M^{n+1}$) and anions($2O^{2-} \leftrightarrow O_2^{2-}$). The overlap of the M(nd)—O(sp) energy band is considered to be the driving force behind the reversible reaction of O_2^{2-}. The redox activity of the anions(O_2^{2-}) in the embedded compounds is clearly identified, explaining the high capacity of the lithium-rich material.[108,109]

Considering the anion redox process, it is necessary to explore the key factor for the stability instead of reoxidation to generating oxygen for O_2^{n-} under high voltage. Li_2MO_3 analogues have been researched for deep understanding formation of O_2^{n-} and balance of oxygen release in layered structure, such as $Li_2Ni_{0.5}Te_{0.5}O_3$[110], $Li_2Fe_{0.5}Sb_{0.5}O_3$[111], Li_2IrO_3[112], $Li_2Ru_{1-y}Sn_yO_3$[108], and $Li_2Fe_{0.28}Te_{0.5}O_3$[113]. $Li_2Ni_{0.5}Te_{0.5}O_3$[110] only has Ni^{+2}/Ni^{+4} redox couple in the reaction with the characteristics of traditional embedded systems. $Li_2Ru_{1-y}Sn_yO_3$[109] involves both anions and cations participating in the redox process without oxygen release while $Li_2Fe_{0.28}Te_{0.5}O_3$[111] only has oxygen release in the redox process. $Li_2Fe_{0.5}Sb_{0.5}O_3$[113] has a more complex redox process, forming peroxide first and then produces oxygen when charging with high voltage.

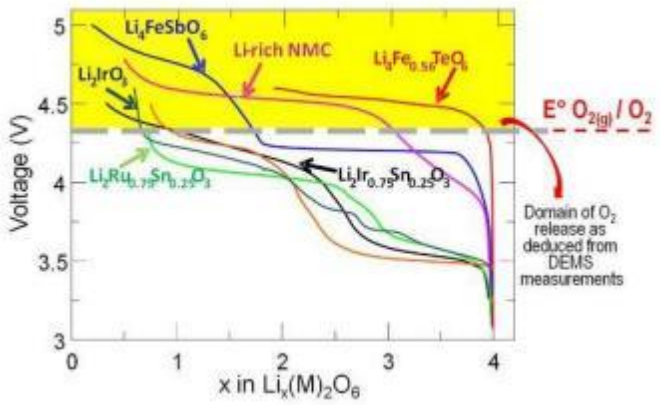

Fig1.10 Charge profiles of Li-rich layered oxide phases. The dashed line corresponds to the O_2/O^{2-} redox couple, and the shaded yellow zone represents the range of potential over which$(O\text{-}O)^{n-}$ are likely to recombine to liberate O_2. Reprinted with permission from ref 10. Electrochem. Soc. 2015, 162 (14), A2490–A2499, under CC BY 4.0 license.

Based on the above phenomenon, it is worth analyzing electrode potential of the O_2/O^{2-} redox couple. According to Fig1.10, the value of the electrode potential of O_2/O^{2-} redox couple for inorganic compounds in aqueous media is nearly to 4.3V vs. Li^+/Li. Therefore, the absence of O_2 evolution during oxidation for Li_2IrO_3[101] and $Li_2Fe_{0.28}Te_{0.5}O_3$[111]is reasonable because their voltage profile falls below the line of electrode potential of O_2/O^{2-}. Compared with $Li_2Fe_{0.5}Sb_{0.5}O_3$[111], whose voltage profile crosses the redox line and indicates the creation of $(O_2)^{n-}$ species.

Despite these studies, no oxygen sublattice distortion due to the formation of O-O perovskite dimers could be observed. $Li_2Ir_{1-y}Sn_yO_3$[109] was successfully synthesized, and its electrochemical performance was systematically evaluated. Unlike the typical S-shaped discharge curve, the discharge profile mirrored the charging curve. Furthermore, no voltage decay was observed during cycling; instead, a rapid decline in capacity was noted. Structural transformations linked to the stepwise voltage changes were examined using X-ray diffraction (XRD) and microscopic techniques. XRD analysis revealed a lithium-induced structural transition from the O3 to the O1 phase during oxidation, a finding corroborated by microscopic studies. For the first time, the presence of O-O dimers was directly observed through annular bright-field scanning transmission electron microscopy (ABF-STEM) imaging, providing experimental evidence that O^{2-} ions actively participate in the redox reactions during the electrode process.[111,113]

Despite these studies, no oxygen sublattice distortion due to the formation of O-O perovskite dimers could be observed. $Li_2Ir_{1-y}Sn_yO_3$[109] was successfully synthesized, and its electrochemical performance was systematically evaluated. Unlike the typical S-shaped discharge curve, the discharge profile mirrored the charging curve. Furthermore, no voltage decay was observed during cycling; instead, a rapid decline in capacity was noted. Structural transformations linked to the stepwise voltage changes were examined using X-ray diffraction (XRD) and microscopic techniques. XRD analysis revealed a lithium-induced structural transition from the O3 to the O1 phase during oxidation, a finding corroborated by microscopic studies. For the first time, the presence of O-O

dimers was directly observed through annular bright-field scanning transmission electron microscopy (ABF-STEM) imaging, providing experimental evidence that O^{2-} ions actively participate in the redox reactions during the electrode process.[111,113]

1.6 Anode materials for LIBS

The negative electrode material currently accounts for about 5%-15% of the battery cost.[118] Based on the mechanisms of storing lithium ions, cathode materials for LIB can be divided to carbon materials with insertion reaction mechanism, alloys such as Si, and Sn with alloying reaction mechanism, and mechanism of conversion reaction for transition metal oxides.[92] Graphite anode, silicon-based anode material, lithium metal anode material and lithium titanate anode material are mostly used nowadays.[119–121]

1.7 Electrolyte for LIBS

The electrolyte should meet the following requirements. It needs a wide electrochemical window to maintain the stability of electrochemical performance in a wide voltage range. It has good compatibility with other parts of the battery, such the electrode materials, the current collectors and separator. It should be safe, non-toxic and non-polluting.[42] Besides, the separator is important because ions in the electrolyte can dissolve or precipitate on the cathode surface and participate in redox reaction on the cathode, resulting in the loss of cathode material.[38]

At present, most of the electrolytes used in commercial lithium batteries are based on $LiPF_6$ EC/DMC, which has good ionic conductivity and electrochemical stability.[122,123]

1.8 Processing: Conventional vs Microwave Heating

The synthesis of nickel-rich cathode materials, such as Li_2NiO_3, is a critical step in determining their electrochemical performance. Traditional solid-state synthesis methods often involve high-temperature calcination and prolonged reaction times, which can lead to challenges in

controlling particle size, morphology, and phase purity.[105,120,121] These factors directly influence the material's capacity, cycling stability, and rate capability. In contrast, microwave-assisted synthesis offers a rapid and energy-efficient alternative, enabling precise control over reaction conditions and promoting uniform heating. This method has been shown to enhance the electrochemical properties of cathode materials by improving crystallinity and reducing defects. Chapter 4 will discuss the advantages and limitations of conventional solid-state synthesis compared to microwave-assisted methods, highlighting the potential of microwave heating for optimizing the performance of nickel-rich cathodes.

1.9 Aims and Objectives

The primary aim of this study is to develop a simple and efficient synthesis route for nickel-rich cathode materials (Li_2NiO_3) with enhanced electrochemical performance. To achieve this, the research focuses on developing a one-step solid-state synthesis method for producing Li-rich and Ni-rich Li_2NiO_3 cathode materials. This approach aims to simplify the synthesis process while maintaining high material quality. The influence of synthesis conditions, such as temperature, time, and atmosphere, on the structural and electrochemical properties of Li_2NiO_3 is thoroughly investigated to identify optimal parameters for maximizing performance.

In addition to conventional synthesis methods, this study explores the use of microwave-assisted synthesis as an innovative alternative. Microwave heating offers the potential to improve the material's capacity and cycling stability by enabling rapid and uniform heating, which can enhance crystallinity and reduce defects. The synthesized materials are characterized using advanced techniques, including X-ray diffraction (XRD), electron microscopy (SEM/TEM), and galvanostatic electrochemical testing, to gain a comprehensive understanding of their structural and electrochemical properties.

The electrochemical performance of microwave-synthesized Li_2NiO_3 is evaluated and compared to that of conventionally synthesized samples, with a particular focus on capacity

retention, rate capability, and long-term cycling stability. By establishing a correlation between synthesis conditions, material properties, and electrochemical performance, this study provides valuable insights for optimizing the production of nickel-rich cathode materials. Ultimately, this research aims to contribute to the development of high-performance lithium-ion batteries by advancing the synthesis and understanding of nickel-rich cathode materials.

References

(1) Kim, J.-H. A Method of Increasing the Energy Density of Layered Ni-Rich $Li[Ni_{1-2x}Co_xMn_x]O_2$ Cathodes (x = 0.05, 0.1, 0.2). *J. Mater. Chem. A* **2019**, 8. https://doi.org/10.1039/C8TA10438G

(2) *Haregewoin, A. M.; Wotango, A. S.; Hwang, B.-J. Electrolyte Additives for Lithium Ion Battery Electrodes: Progress and Perspectives. Energy Environ. Sci. 2016, 9 (6), 1955–1988.* https://doi.org/10.1039/C5EE03874E

(3) Thackeray, M. M.; Wolverton, C.; Isaacs, E. D. Electrical Energy Storage for Transportation—Approaching the Limits of, and Going beyond, Lithium-Ion Batteries. *Energy Environ. Sci.* **2012**, *5* (7), 7854. https://doi.org/10.1039/c2ee21892e.

(4) Manthiram, A. A Reflection on Lithium-Ion Battery Cathode Chemistry. *Nat. Commun.* **2020**, *11* (1), 1550. https://doi.org/10.1038/s41467-020-15355-0.

(5) Anoopkumar, V.; John, B.; Mercy, T. D. Potassium-Ion Batteries: Key to Future Large-Scale Energy Storage? ACS Appl. Energy Mater. 2020, 3 (10), 9478–9492. https://doi.org/10.1021/acsaem.0c01574

(6) Rogelj, J.; Huppmann, D.; Krey, V.; Riahi, K.; Clarke, L.; Gidden, M.; Nicholls, Z.; Meinshausen, M. A New Scenario Logic for the Paris Agreement Long-Term Temperature Goal. *Nature* **2019**, *573* (7774), 357–363. https://doi.org/10.1038/s41586-019-1541-4.

(7) Ding, Y.-L.; Cano, Z.; Yu, A.; Lu, J.; Chen, Z. Automotive Li-Ion Batteries: Current Status and Future Perspectives. *Electrochem. Energy Rev.* **2019**, *2*, 1–28. https://doi.org/10.1007/s41918 018-0022-z.

(8) *Lithium Ion Battery Market*. Market.us. https://market.us/report/lithium-ion-battery-market/ (accessed 2025-02-08).

(9) *Market Research Company - Mordor Intelligence™*. https://www.mordorintelligence.com (accessed 2025-02-09).

(10) Rozier, P.; Tarascon, J. M. Review—Li-Rich Layered Oxide Cathodes for Next-Generation

Li-Ion Batteries: Chances and Challenges. J. Electrochem. Soc. 2015, 162 (14), A2490–A2499. https://doi.org/10.1149/2.0111514jes

(11) Mao, L.; Ai, L.; Li, S.; Hou, Q.; Xie, Y.; Liang, Y.; Xie, J. Improved Electrochemical Properties of Nickel Rich LiNi0.6Co0.2Mn0.2O2 Cathode Materials by Al_2O_3 Coating. *AIP Conference Proceedings* **2018**, *020049*. https://doi.org/10.1063/1.5029766.

(12) Liu, C.; Neale, Z. G.; Cao, G. Understanding Electrochemical Potentials of Cathode Materials in Rechargeable Batteries. *Mater. Today* **2016**, *19* (2), 109–123. https://doi.org/10.1016/j.mattod.2015.10.009.

(13) Chen, L.; Venkatram, S.; Kim, C.; Batra, R.; Chandrasekaran, A.; Ramprasad, R. Electrochemical Stability Window of Polymeric Electrolytes. *Chem. Mater.* **2019**, *31* (12), 4598 4604. https://doi.org/10.1021/acs.chemmater.9b01553.

(14) Wang, A.; Kadam, S.; Li, H.; Shi, S.; Qi, Y. Review on Modeling of the Anode Solid Electrolyte Interphase (SEI) for Lithium-Ion Batteries. *Npj Comput. Mater.* **2018**, *4* (1), 1–26. https://doi.org/10.1038/s41524-018-0064-0.

(15) Wang, H.; Jang, Y.-I.; Huang, B.; Sadoway, D.; Chiang, Y. TEM Study of Electrochemical Cycling-Induced Damage and Disorder in LiCoO2 Cathodes for Rechargeable Lithium Batteries. *J. Electrochem. Soc.* **1999**, *146*, 473–480. https://doi.org/10.1149/1.1391631. (16) Prosini, P. P.; Zane, D.; Pasquali, M. Improved Electrochemical Performance of a $LiFePO_4$-Based Composite Cathode. *Electrochimica Acta* **2001**, *46* (23), 3517–3523. https://doi.org/10.1016/S0013 4686(01)00631-4.

(17) Zhang, B.; Li, L.; Zheng, J. Characterization of Multiple Metals (Cr, Mg) Substituted $LiNi_{0.8}Co_{0.1}Mn_{0.1}O_2$ Cathode Materials for Lithium Ion Battery. *J. Alloys Compd.* **2012**, *520*, 190 194. https://doi.org/10.1016/j.jallcom.2012.01.004.

(18) Amalraj, S.; Sharon, D.; Talianker, M.; Julien, C.; Burlaka, L.; Lavi, R.; Zhecheva, E.; Markovsky, B.; Zinigrad, E.; Kovacheva, D.; Stoyanova, R.; Aurbach, D. Study of the Nanosized Li_2MnO_3: Electrochemical Behavior, Structure, Magnetic Properties, and Vibrational Modes.

Electrochimica Acta **2013**, *97*, 259–270. https://doi.org/10.1016/j.electacta.2013.03.029.

(19) Gu, M.; He, Y.; Zheng, J.; Wang, C. Nanoscale Silicon as Anode for Li-Ion Batteries: The Fundamentals, Promises, and Challenges. *Nano Energy* **2015**, *17*, 366–383. https://doi.org/10.1016/j.nanoen.2015.08.025.

(20) Xu, W.; Wang, J.; Ding, F.; Chen, X.; Nasybulin, E.; Zhang, Y.; Zhang, J.-G. Lithium Metal Anodes for Rechargeable Batteries. *Energy Env. Sci* **2014**, *7* (2), 513–537. https://doi.org/10.1039/C3EE40795K.

(21) Liang, G.; Peterson, V. K.; See, K. W.; Guo, Z.; Pang, W. K. Developing High-Voltage Spinel $LiNi_{0.5}Mn_{1.5}O_4$ Cathodes for High-Energy-Density Lithium-Ion Batteries: Current Achievements and Future Prospects. *J. Mater. Chem. A* **2020**, *8* (31), 15373–15398. https://doi.org/10.1039/D0TA02812F.

(22) Zhang, M.; Garcia-Araez, N.; Hector, A. L. Understanding and Development of Olivine $LiCoPO_4$ Cathode Materials for Lithium-Ion Batteries. *J. Mater. Chem. A* **2018**, *6* (30), 14483 14517. https://doi.org/10.1039/C8TA04063J.

(23) Thackeray, M. M.; Amine, K. $Li_4Ti_5O_{12}$ Spinel Anodes. *Nat. Energy* **2021**, *6* (6), 683–683. https://doi.org/10.1038/s41560-021-00829-2.

(24) Gerber, L. C. H.; Frischmann, P. D.; Fan, F. Y.; Doris, S. E.; Qu, X.; Scheuermann, A. M.; Persson, K.; Chiang, Y.-M.; Helms, B. A. Three-Dimensional Growth of Li_2S in Lithium–Sulfur Batteries Promoted by a Redox Mediator. *Nano Lett.* **2016**, *16* (1), 549–554. https://doi.org/10.1021/acs.nanolett.5b04189.

(25) Fantin, R.; Trevisanello, E.; Ruess, R.; Pokle, A.; Conforto, G.; Richter, F. H.; Volz, K.; Janek, J. Synthesis and Postprocessing of Single-Crystalline $LiNi_{0.8}Co_{0.15}Al_{0.05}O_2$ for Solid-State Lithium-Ion Batteries with High Capacity and Long Cycling Stability. *Chem. Mater.* **2021**, *33* (7), 2624–2634. https://doi.org/10.1021/acs.chemmater.1c00471.

(26) Zha, G.; Hu, N.; Luo, Y.; Wang, F.; Wu, R.; Li, Y.; Fu, H.; Fu, X. Reducing Ni/Li Disorder and Boosting Electrochemical Performance of $LiNi_{0.8}Co_{0.06}7Fe_{0.033}Mn_{0.1}O_2$ Cathode Material. *J.*

Taiwan Inst. Chem. Eng. **2023**, *144*, 104730. https://doi.org/10.1016/j.jtice.2023.104730.

(27) Castel, E.; Berg, E. J.; El Kazzi, M.; Novák, P.; Villevieille, C. Differential Electrochemical Mass Spectrometry Study of the Interface of $xLi_2MnO_3 \cdot (1–x)LiMO_2$ (M = Ni, Co, and Mn) Material as a Positive Electrode in Li-Ion Batteries. *Chem. Mater.* **2014**, *26* (17), 5051–5057. https://doi.org/10.1021/cm502201z.

(28) Reeves-McLaren, N. *Inside Energy Storage Materials: Diffraction and Spectroscopic Methods for Battery Research*; AIP Publishing: 2022. https://doi.org/10.1063/9780735424197.

(29) Ramasubramanian, B.; Reddy, M.V.; Zaghib, K.; Armand, M.; Ramakrishna, S. Growth Mechanism of Micro/Nano Metal Dendrites and Cumulative Strategies for Countering Its Impacts in Metal Ion Batteries: A Review. Nanomaterials 2021, 11, 2476. https://doi.org/10.3390/nano11102476

(30) Goodenough, J. B.; Kim, Y. Challenges for Rechargeable Li Batteries. *Chem. Mater.* **2010**, *22* (3), 587–603. https://doi.org/10.1021/cm901452z.

(31) Whittingham, M. S. Lithium Batteries and Cathode Materials. *ChemInform* **2004**, *35* (50). https://doi.org/10.1002/chin.200450266.

(32) Burns, J.; Krause, L.; Le, D.-B.; Jensen, L.; Smith, A.; Xiong, D.; Dahn, J. Introducing Symmetric Li-Ion Cells as a Tool to Study Cell Degradation Mechanisms. *J. Electrochem. Soc.* **2011**, *158*, A1417. https://doi.org/10.1149/2.084112jes.

(33) Sinha, N.; Smith, A.; Burns, C.; Jain, G.; Eberman, K.; Scott, E.; Gardner, J.; Dahn, J. The Use of Elevated Temperature Storage Experiments to Learn about Parasitic Reactions in Wound $LiCoO_2$/Graphite Cells. *J. Electrochem. Soc.* **2011**, *158*, A1194–A1201. https://doi.org/10.1149/2.007111jes.

(34) Smith, A.; Burns, J.; Xiong, D.; Dahn, J. Interpreting High Precision Coulometry Results on Li-Ion Cells. *J. Electrochem. Soc.* **2011**, *158*, A1136–A1142. https://doi.org/10.1149/1.3625232.

(35) Hayner, C. M.; Zhao, X.; Kung, H. H. Materials for Rechargeable Lithium-Ion Batteries. *Annu. Rev. Chem. Biomol. Eng.* **2012**, *3* (1), 445–471. https://doi.org/10.1146/annurev-chembioeng

062011-081024.

(36) Blomgren, G. E. The Development and Future of Lithium Ion Batteries. *J. Electrochem. Soc.* **2017**, *164* (1), A5019–A5025. https://doi.org/10.1149/2.0251701jes.

(37) Mekonnen, Y.; Sundararajan, A.; Sarwat, A. I. A Review of Cathode and Anode Materials for Lithium-Ion Batteries. In *SoutheastCon 2016*; IEEE: Norfolk, VA, USA, 2016; pp 1–6. https://doi.org/10.1109/SECON.2016.7506639.

(38) Andersson, A.; Kalska, B.; Häggström, L.; Thomas, J. Lithium Extraction/Insertion in $LiFePO_4$: An X-Ray Diffraction and Moessbauer Spectroscopy Study. *Solid State Ion.* **2000**, *130*, 41–52. https://doi.org/10.1016/S0167-2738(00)00311-8.

(39) Wang, H.-E.; Qian, D.; Lu, Z.; Li, Y. Synthesis and Electrochemical Properties of LiMn2O4 and $LiCoO_2$-Coated $LiMn_2O_4$ Cathode Materials. *J. Alloys Compd.* **2012**, *517*, 186–191. https://doi.org/10.1016/j.jallcom.2011.12.079.

(40) Kim, T.-H.; Park, J.-S.; Chang, S. K.; Choi, S.; Ryu, J. H.; Song, H.-K. The Current Move of Lithium Ion Batteries Towards the Next Phase. *Adv. Energy Mater.* **2012**, *2* (7), 860–872. https://doi.org/10.1002/aenm.201200028.

(41) Padhi, A. K.; Nanjundaswamy, K. S.; Goodenough, J. B. Phospho-olivines as Positive Electrode Materials for Rechargeable Lithium Batteries. *J. Electrochem. Soc.* **1997**, *144* (4), 1188 1194. https://doi.org/10.1149/1.1837571.

(42) Koltypin, M.; Aurbach, D.; Nazar, L.; Ellis, B. On the Stability of $LiFePO_4$ Olivine Cathodes under Various Conditions (Electrolyte Solutions, Temperatures). *Electrochem. Solid-State Lett.* **2007**, *10*. https://doi.org/10.1149/1.2403974.

(43) Ping, P.; Wang, Q.; Sun, J.; Xiang, H. F.; Chen, C. Thermal Stabilities of Some Lithium Salts and Their Electrolyte Solutions With and Without Contact to a LiFePO4 Electrode. *J. Electrochem. Soc.* **2010**, *157*, A1170–A1176. https://doi.org/10.1149/1.3473789.

(44) Suo, L.; Han, W.; Lu, X.; Gu, L.; Hu, Y.-S.; Li, H.; Chen, D.; Chen, L.; Tsukimoto, S.; Ikuhara, Y. Highly Ordered Staging Structural Interface between $LiFePO_4$ and $FePO_4$. *Phys. Chem.*

Chem. Phys. **2012**, *14*, 5363–5367. https://doi.org/10.1039/c2cp40610a.

(45) Gu, L.; Zhu, C.; Li, H.; Yu, Y.; Li, C.; Tsukimoto, S.; Maier, J.; Ikuhara, Y. Direct Observation of Lithium Staging in Partially Delithiated $LiFePO_4$ at Atomic Resolution. *J. Am. Chem. Soc.* **2011**, *133*, 4661–4663. https://doi.org/10.1021/ja109412x.

(46) Andersson, A. S.; Thomas, J. O. The Source of First-Cycle Capacity Loss in $LiFePO_4$. J. Power Sources 2001, 97-98, 498–502. https://doi.org/10.1016/S0378-7753(01)00633-4.

(47) Srinivasan, V.; Newman, J. Discharge Model for the Lithium Iron-Phosphate Electrode. *J. Electrochem. Soc.* **2004**, *151* (10), A1517. https://doi.org/10.1149/1.1785012.

(48) Chen, G.; Richardson, T. Improving the Performance of Lithium Manganese Phosphate Through Divalent Cation Substitution. *Electrochem. Solid-State Lett.* 2008, *11* (10), A190–A194. https://doi.org/10.1149/1.2971169.

(49) Stanishev, V.; Aebi, P.; Passerini, S.; Novák, P.; Battaglia**, C.** Study of the $LiFePO_4/FePO_4$. Two-Phase System by High-Resolution Electron Energy Loss Spectroscopy. *Chem. Mater.* **2012,** *24* (4), 622–626. https://doi.org/10.1021/cm203245j.

(50) Sun, Y.; Lu, X.; Xiao, R.; Li, H.; Huang, X. Kinetically Controlled Lithium-Staging in Delithiated $LiFePO_4$ Driven by the Fe Center Mediated Interlayer Li–Li Interactions. *Chem. Mater.* **2012**, *24* (24), 4693–4703. https://doi.org/10.1021/cm3028324.

(51) Chung, S.-Y.; Bloking, J.; Chiang, Y.-M. Electronically Conductive Phospho-Olivines as Lithium Storage Electrodes. *Nat. Mater.* **2002**, *1*, 123–128. https://doi.org/10.1038/nmat732.

(52) Cheng, H.; Shapter, J. G.; Li, Y.; Gao, G. Recent Progress of Advanced Anode Materials of Lithium-Ion Batteries. *J. Energy Chem.* **2021**, *57*, 451–468. https://doi.org/10.1016/j.jechem.2020.08.056.

(53) Choi, N.-S.; Chen, Z.; Freunberger, S. A.; Ji, X.; Sun, Y.-K.; Amine, K.; Yushin, G.; Nazar, L. F.; Cho, J.; Bruce, P. G. Challenges Facing Lithium Batteries and Electrical Double-Layer Capacitors. *Angew. Chem. Int. Ed.* **2012**, *51* (40), 9994–10024. https://doi.org/10.1002/anie.201201429.

(54) Wang, J.; Sun, X. Understanding and Recent Development of Carbon Coating on $LiFePO_4$ Cathode Materials for Lithium-Ion Batteries. *Energy Env. Sci* **2012**, *5* (1), 5163–5185. https://doi.org/10.1039/C1EE01263K.

(55) Wang, G. X.; Needham, S.; Yao, J.; Wang, J. Z.; Liu, R. S.; Liu, H. K. A Study on $LiFePO_4$ and Its Doped Derivatives as Cathode Materials for Lithium-Ion Batteries. *J. Power Sources* **2006**, *159* (1), 282–286. https://doi.org/10.1016/j.jpowsour.2006.04.046.

(56) Park, Y.-S.; Bang, H. J.; Oh, S.-M.; Sun, Y.-K.; Lee, S.-M. Effect of Carbon Coating on Thermal Stability of Natural Graphite Spheres Used as Anode Materials in Lithium-Ion Batteries. *J. Power Sources* **2009**, *190* (2), 553–557. https://doi.org/10.1016/j.jpowsour.2009.01.067.

(57) Yamada, A.; Chung, S. C.; Hinokuma, K. Optimized $LiFePO_4$ for Lithium Battery Cathodes. *J. Electrochem. Soc.* **2001**, *148* (3), A224. https://doi.org/10.1149/1.1348257.

(58) Martha, S. K.; Markovsky, B.; Grinblat, J.; Gofer, Y.; Haik, O.; Zinigrad, E.; Aurbach, D.; Drezen, T.; Wang, D.; Deghenghi, G.; Exnar, I. $LiMnPO_4$ as an Advanced Cathode Material for Rechargeable Lithium Batteries. *J. Electrochem. Soc.* 2009, *156* (7), A541–A552. https://doi.org/10.1149/1.3125765

(59) Nasir, M. H.; Janjua, N. K.; Santoki, J. Electrochemical Performance of Carbon Modified $LiNiPO_4$ as Li-Ion Battery Cathode: A Combined Experimental and Theoretical Study. *J. Electrochem. Soc.* **2020**, *167* (13), 130526. https://doi.org/10.1149/1945-7111/abb83d.

(60) Wang, D.; Buqa, H.; Crouzet, M.; Deghenghi, G.; Drezen, T.; Exnar, I.; Kwon, N.-H.; Miners, J. H.; Poletto, L.; Grätzel, M. High-Performance, Nano-Structured LiMnPO4 Synthesized via a Polyol Method. *J. Power Sources* **2009**, *189* (1), 624–628. https://doi.org/10.1016/j.jpowsour.2008.09.077.

(61) Delacourt, C.; Poizot, P.; Morcrette, M.; Tarascon, J.-M.; Masquelier, C. One-Step Low Temperature Route for the Preparation of Electrochemically Active $LiMnPO_4$ Powders. *Chem. Mater.* **2004**, *16* (1), 93–99. https://doi.org/10.1021/cm030347b.

(62) Yang, J.; Xu, J. J. Synthesis and Characterization of Carbon-Coated Lithium Transition

Metal Phosphates $LiMPO_4$ (M = Fe , Mn, Co, Ni) Prepared via a Nonaqueous Sol-Gel Route. *J. Electrochem. Soc.* **2006**, *153* (4), A716. https://doi.org/10.1149/1.2168410.

(63) Chen, G.; Richardson, T. Improving the Performance of Lithium Manganese Phosphate Through Divalent Cation Substitution. *Electrochem. Solid-State Lett.* **2008**, *11* (10), A190–A194. https://doi.org/10.1149/1.2971169.

(64) Martha, S. K.; Grinblat, J.; Haik, O.; Zinigrad, E.; Drezen, T.; Miners, J. H.; Exnar, I.; Kay, A.; Markovsky, B.; Aurbach, D. $LiMn_{0.8}Fe_{0.2}PO_4$: An Advanced Cathode Material for Rechargeable Lithium Batteries. *Angew. Chem. Int. Ed.* **2009**, *48* (45), 8559–8563. https://doi.org/10.1002/anie.200903587.

(65) Thackeray, M. M.; David, W. I. F.; Bruce, P. G.; Goodenough, J. B. Lithium Insertion into Manganese Spinels. *Mater. Res. Bull.* **1983**, *18* (4), 461–472. https://doi.org/10.1016/0025 5408(83)90138-1.

(66) Liu, J.; Zhang, J.-G.; Yang, Z.; Lemmon, J. P.; Imhoff, C.; Graff, G. L.; Li, L.; Hu, J.; Wang, C.; Xiao, J.; Xia, G.; Viswanathan, V. V.; Baskaran, S.; Sprenkle, V.; Li, X.; Shao, Y.; Schwenzer, B. Materials Science and Materials Chemistry for Large Scale Electrochemical Energy Storage: From Transportation to Electrical Grid. *Adv. Funct. Mater.* **2013**, *23* (8), 929–946. https://doi.org/10.1002/adfm.201200690.

(67) Ellis, B. L.; Lee, K. T.; Nazar, L. F. Positive Electrode Materials for Li-Ion and Li-Batteries. *Chem. Mater.* **2010**, *22* (3), 691–714. https://doi.org/10.1021/cm902696j.

(68) **Dou, S.** Review and Prospects of Mn-Based Spinel Compounds as Cathode Materials for Lithium-Ion Batteries. *Ionics* **2015**, *21*, 3001–3030. https://doi.org/10.1007/s11581-015-1545-5

(69) Tarascon, J. M.; Guyomard, D.; Baker, G. L. An Update of the Li Metal-Free Rechargeable Battery Based on $Li_{1+x}Mn_2O_4$ Cathodes and Carbon Anodes. *J. Power Sources* **1993, *44* (1-3), 689 700.** https://doi.org/10.1016/0378-7753(93)80220-J

(70) Amatucci, G.; Tarascon, J.-M. Optimization of Insertion Compounds Such as $LiMn_2O_4$ for Li-Ion Batteries. *J. Electrochem. Soc.* **2002**, *149* (12), K31. https://doi.org/10.1149/1.1516778.

(71) Hosono, E.; Kudo, T.; Honma, I.; Matsuda, H.; Zhou, H. Synthesis of Single Crystalline Spinel $LiMn_2O_4$ Nanowires for a Lithium Ion Battery with High Power Density. *Nano Lett.* **2009**, *9*, 1045–1051. https://doi.org/10.1021/nl803394v.

(72) Arora, P.; Popov, B.; White, R. Electrochemical Investigations of Cobalt-Doped $LiMn_2O_4$ as Cathode Material for Lithium-Ion Batteries. *ChemInform* **2010**, *29* (21). https://doi.org/10.1002/chin.199821016.

(73) Aurbach, D.; Markovsky, B.; Salitra, G.; Markevich, E.; Talyossef, Y.; Koltypin, M.; Nazar, L.; Ellis, B.; Kovacheva, D. Review on Electrode–Electrolyte Solution Interactions, Related to Cathode Materials for Li-Ion Batteries. *J. Power Sources* **2007**, *165* (2), 491–499. https://doi.org/10.1016/j.jpowsour.2006.10.025.

(74) Delmas, C.; Fouassier, C.; Hagenmuller, P. Structural Classification and Properties of the Layered Oxides. *Phys. BC* **1980**, *99* (1), 81–85. https://doi.org/10.1016/0378-4363(80)90214-4.

(75) Chang, K.; Hallstedt, B.; Music, D.; Fischer, J.; Ziebert, C.; Ulrich, S.; Seifert, H. J. Thermodynamic Description of the Layered O_3 and O_2 Structural $LiCoO_2$–CoO_2 Pseudo-Binary Systems. *Calphad* **2013**, *41*, 6–15. https://doi.org/10.1016/j.calphad.2013.01.001.

(76) Delmas, C.; Braconnier, J.-J.; Hagenmuller, P. A New Variety of $LiCoO_2$ with an Unusual Oxygen Packing Obtained by Exchange Reaction. *Mater. Res. Bull.* **1982**, *17* (1), 117–123. https://doi.org/10.1016/0025-5408(82)90192-1.

(77) Mendiboure, A.; Delmas, C.; Hagenmuller, P. New Layered Structure Obtained by Electrochemical Deintercalation of the Metastable LiCoO2_22 (O2) Variety. *J. Solid State Chem.* **1985,** *57* (3), 323–331. https://doi.org/10.1016/0022-4596(85)90189-2.

(78) Chung, K. Y.; Yoon, W.-S.; McBreen, J.; Yang, X.-Q.; Oh, S. H.; Shin, H. C.; Cho, W. I.; Cho, B. W. Structural Studies on the Effects of ZrO_2 Coating on $LiCoO_2$ during Cycling Using In Situ X-Ray Diffraction Technique. *J. Electrochem. Soc.* **2006**, *153* (11), A2152. https://doi.org/10.1149/1.2338661.

(79) Endo, E.; Yasuda, T.; Kita, A.; Yamaura, K.; Sekai, K. A $LiCoO_2$ Cathode Modified by

Plasma Chemical Vapor Deposition for Higher Voltage Performance. *J. Electrochem. Soc.* **2000**, *147* (4), 1291. https://doi.org/10.1149/1.1393352.

(80) Amatucci, G. G.; Tarascon, J. M.; Klein, L. C. Cobalt Dissolution in $LiCoO_2$-Based Non Aqueous Rechargeable Batteries. *Solid State Ion.* **1996**, *83* (1), 167–173. https://doi.org/10.1016/0167-2738(95)00231-6.

(81) Cho, J.; Kim, Y. J.; Kim, T.-J.; Park, B. Zero-Strain Intercalation Cathode for Rechargeable Li-Ion Cell. *Angew. Chem. Int. Ed.* **2001**, *40* (18), 3367–3369. https://doi.org/10.1002/1521 3773(20010917)40:18<3367::AID-ANIE3367>3.0.CO;2-A.

(82) Chen, Z.; Dahn, J. R. Methods to Obtain Excellent Capacity Retention in $LiCoO_2$ Cycled to 4.5 V. *Electrochimica Acta* **2004**, *49* (7), 1079–1090. https://doi.org/10.1016/j.electacta.2003.10.019.

(83) Dahn, J. R.; von Sacken, U.; Michal, C. A. Structure and Electrochemistry of $Li_{1\pm\gamma}NiO_2$ and a New Li_2NiO_2 Phase with the $Ni(OH)_2$ Structure. Solid State Ionics 1990, 44 (1–2), 87–97. https://doi.org/10.1016/0167-2738(90)90071-6

(84) Ohzuku, T.; Ueda, A.; Nagayama, M. Electrochemistry and Structural Chemistry of $LiNiO_2$ ($R\bar{3}m$) for 4 Volt Secondary Lithium Cells. *J. Electrochem. Soc.* **1993**, *140* (7), 1862–1870. https://doi.org/10.1149/1.2220730.

(85) Li, J.; Shunmugasundaram, R.; Doig, R.; Dahn, J. R. In Situ X-Ray Diffraction Study of Layered Li–Ni–Mn–Co Oxides: Effect of Particle Size and Structural Stability of Core–Shell Materials. *Chem. Mater.* **2016**, *28* (1), 162–171. https://doi.org/10.1021/acs.chemmater.5b03500.

(86) Rougier, A.; Gravereau, P.; Delmas, C. Optimization of the Composition of the $Li_{1-z}Ni_{1+z}O_2$ Electrode Materials: Structural, Magnetic, and Electrochemical Studies. *J. Electrochem. Soc.* **1996**,*143* (4), 1168–1175. https://doi.org/10.1149/1.1836614.

(87) Lee, Y. S.; Yoon, C. S.; Sun, Y. K.; Yoshio, M. Structural Characterization of Mn-Based Materials Using γ-MnOOH Source. *Electrochem. Solid-State Lett.* **2001**, *5* (1), A1. https://doi.org/10.1149/1.1419702.

(88) Geldasa, F. T.; Kebede, M. A.; Shura, M. W.; Hone, F. G. Identifying Surface Degradation, Mechanical Failure, and Thermal Instability Phenomena of High Energy Density Ni-Rich NCM Cathode Materials for Lithium-Ion Batteries: A Review. ACS Appl. Energy Mater. 2022, 5 (10), 5891–5909. https://doi.org/10.1021/acsaem.2c00513

(89) Zhao, H.; Law, H.; Liao, S.; Chen, D.; Lin, P. Novel Graphitic Sheets with Ripple-like Folds as an NCA Cathode Coating Layer for High-Energy-Density Lithium-Ion Batteries. *Nanotechnology* **2020**, *32* (8), 08LT01. https://doi.org/10.1088/1361-6528/abc4a1.

(90) Oh, P.; Ko, M.; Myeong, S.; Kim, Y.; Cho, J. A Novel Surface Treatment Method and New Insight into Discharge Voltage Deterioration for High-Performance $0.4Li_2MnO_3$ $0.6LiNi_{1/3}Co_{1/3}Mn_{1/3}O_2$ Cathode Materials. *Adv. Energy Mater.* **2014**, *4* (16), 1400631. https://doi.org/10.1002/aenm.201400631.

(91) Manthiram, A.; Murugan, A. V.; Sarkar, A.; Muraliganth, T. Nanostructured Electrode Materials for Electrochemical Energy Storage and Conversion. *Energy Environ. Sci.* **2008**, *1* (6), 621–638. https://doi.org/10.1039/B811802G.

(92) Cai, L.; Liu, Z.; An, K.; Liang, C. Probing Li-Ni Cation Disorder in $Li_{1-x}Ni_{1+x-y}Al_yO_2$ Cathode Materials by Neutron Diffraction. *J. Electrochem. Soc.* **2012**, *159* (7), A924. https://doi.org/10.1149/2.005207jes.

(93) Zhang, X.; Jiang, W.; Mauger, A.; Qilu; Gendron, F.; Julien, C. Minimization of the Cation Mixing in $Li_{1+x}(NMC)_{1-x}O_2$ as Cathode Material. *J. Power Sources* **2010**, *195*, 1292–1301. https://doi.org/10.1016/j.jpowsour.2009.09.029.

(94) Tabuchi, M.; Kuriyama, N.; Takamori, K.; Imanari, Y.; Nakane, K. Appearance of Lithium Excess $LiNiO_2$ with High Cyclability Synthesized by Thermal Decomposition Route from $LiNiO_2$ Li_2NiO_3 Solid Solution. *J. Electrochem. Soc.* **2016**, *163* (10), A2312–A2317. https://doi.org/10.1149/2.0861610jes.

(95) Antolini, E. $Li_xNi_{1-x}O$ ($0 < x \leq 0.3$) Solid Solutions: Formation, Structure, and Transport Properties. *ChemInform* **2004**, *35* (24). https://doi.org/10.1002/chin.200424209. (96

Boulineau, A.; Croguennec, L.; Delmas, C.; Weill, F. Structure of Li_2MnO_3 with Different Degrees of Defects. *Solid State Ion.* **2010**, *180* (40), 1652–1659. https://doi.org/10.1016/j.ssi.2009.10.020.

(97) Thackeray, M. M.; Kang, S.-H.; Johnson, C. S.; Vaughey, J. T.; Hackney, S. A. Comments on the Structural Complexity of Lithium-Rich $Li_{1+x}M_{1-x}O_2$ Electrodes (M=Mn, Ni, Co) for Lithium Batteries. *Electrochem. Commun.* **2006**, *8* (9), 1531–1538. https://doi.org/10.1016/j.elecom.2006.06.030.

(98) Huang, Y.; Dong, Y.; Li, S.; Lee, J.; Wang, C.; Zhu, Z.; Xue, W.; Li, Y.; Li, J. Lithium Manganese Spinel Cathodes for Lithium-Ion Batteries. *Adv. Energy Mater.* **2021**, *11* (2), 2000997. https://doi.org/10.1002/aenm.202000997.

(99) Rossouw, M. H.; Thackeray, M. M. Lithium Manganese Oxides from Li_2MnO_3 for Rechargeable Lithium Battery Applications. *Mater. Res. Bull.* **1991**, *26* (6), 463–473. https://doi.org/10.1016/0025-5408(91)90186-P. (100) Jarvis, K. A.; Deng, Z.; Allard, L. F.; Manthiram, A.; Ferreira, P. J. Atomic Structure of a Lithium-Rich Layered Oxide Material for Lithium-Ion Batteries: Evidence of a Solid Solution. *Chem. Mater.* **2011**, *23* (16), 3614–3621. https://doi.org/10.1021/cm200831c.

(101) Croy, J. R.; Kim, D.; Balasubramanian, M.; Gallagher, K.; Kang, S.-H.; Thackeray, M. M. Countering the Voltage Decay in High Capacity $xLi_2MnO_3 \bullet (1-x)LiMO_2$ Electrodes (M=Mn, Ni, Co) for Li^+ -Ion Batteries. *J. Electrochem. Soc.* **2012**, *159* (6), A781–A790. https://doi.org/10.1149/2.080206jes.

(102) Rossouw, M. H.; Liles, D. C.; Thackeray, M. M. Synthesis and Structural Characterization of a Novel Layered Lithium Manganese Oxide, Li0.36Mn0.91O2, and Its Lithiated Derivative, $Li_{1.09}Mn_{0.91}O_2$. *J. Solid State Chem.* **1993**, *104* (2), 464–466. https://doi.org/10.1006/jssc.1993.1182.

(103) Bianchini, M.; Schiele, A.; Schweidler, S.; Sicolo, S.; Fauth, F.; Suard, E.; Indris, S.; Mazilkin, A.; Nagel, P.; Schuppler, S.; Merz, M.; Hartmann, P.; Brezesinski, T.; Janek, J. From $LiNiO_2$ to Li_2NiO_3: Synthesis, Structures and Electrochemical Mechanisms in Li-Rich Nickel

Oxides. *Chem. Mater.* **2020**, *32* (21), 9211–9227. https://doi.org/10.1021/acs.chemmater.0c02880.

(104) Lee, J. G.; Hwang, H. J.; Kwon, O.; Jeon, O. S.; Jang, J.; Shul, Y.-G. Synthesis and Application of Hexagonal Perovskite $BaNiO_3$ with Quadrivalent Nickel under Atmospheric and Low-Temperature Conditions. *Chem. Commun.* **2016**, *52* (71), 10731–10734. https://doi.org/10.1039/C6CC05704G.

(105) Chen, Z.; Dahn, J. Improving the Capacity Retention of $LiCoO_2$ Cycled to 4.5 V by Heat Treatment. *Electrochem. Solid State Lett.* **2004**, *7*, A11–A14. https://doi.org/10.1149/1.1628871.

(106) Thiele, G.; Stracke, W**.** Über Die Darstellung von Lithium-Nickel-Oxyd. *Z. Anorg. Allg. Chem.* **1964,** *333* (4–5), 281–286. https://doi.org/10.1002/zaac.19643330405.

(107) Migeon, H.-N.; Zanne, M.; Gleitzer, C.; Aubry, J. The Li_2O–NiO–O_2 System at 670 °C and the Consequences of Non-Stoichiometry on the Magnetic Properties of the $Li_xNi_{1-x}O_{1\pm y}$ Phases. *J. Mater. Sci.* **1978**, *13* (3), 461–470. https://doi.org/10.1007/BF00541793. (108) Sathiya, M.; Rousse, G.; Ramesha, K.; Laisa, C. P.; Vezin, H.; Sougrati, M. T.; Doublet, M.-L.; Foix, D.; Gonbeau, D.; Walker, W.; Prakash, A. S.; Ben Hassine, M.; Dupont, L.; Tarascon, J.-M. Reversible Anionic Redox Chemistry in High-Capacity Layered-Oxide Electrodes. *Nat. Mater.* **2013**, *12* (9), 827–835. https://doi.org/10.1038/nmat3699.

(109) Sathiya, M.; Ramesha, K.; Rousse, G.; Foix, D.; Gonbeau, D.; Prakash, A. S.; Doublet, M. L.; Hemalatha, K.; Tarascon, J.-M. High Performance $Li_2Ru_{1-y}Mn_yO_3$ ($0.2 \leq y \leq 0.8$) Cathode Materials for Rechargeable Lithium-Ion Batteries: Their Understanding. *Chem. Mater.* **2013**, *25* (7), 1121–1131. https://doi.org/10.1021/cm400193m.

(110) Sathiya, M.; Ramesha, K.; Rousse, G.; Foix, D.; Gonbeau, D.; Guruprakash, K.; Prakash, A. S.; Doublet, M. L.; Tarascon, J.-M. Li_4NiTeO_6 as a Positive Electrode for Li-Ion Batteries. *Chem. Commun.* **2013**, *49* (97), 11376–11378. https://doi.org/10.1039/C3CC46842A.

(111) Mccalla, E.; Annigere, P.; J. Berg, E.; Saubanere, M.; Abakumov, A.; Foix, D.; Klobes, B.; Sougrati, M. T.; Rousse, G.; Lepoivre, F.; Mariyappan, S.; Doublet, M.-L.; Gonbeau, D.; Novak, P.; van Tendeloo, G.; Hermann, R.; Tarascon, J.-M. Reversible Li-Intercalation through Oxygen

Reactivity in Li-Rich Li-Fe-Te Oxide Materials. *J. Electrochem. Soc.* **2015**, *162*, A1341. https://doi.org/10.1149/2.0991507jes.

(112) McCalla, E.; Abakumov, A. M.; Saubanère, M.; Foix, D.; Berg, E. J.; Rousse, G.; Doublet, M.-L.; Gonbeau, D.; Novák, P.; Van Tendeloo, G.; Dominko, R.; Tarascon, J.-M. Visualization of O-O Peroxo-like Dimers in High-Capacity Layered Oxides for Li-Ion Batteries. *Science* **2015**, *350* (6267), 1516–1521. https://doi.org/10.1126/science.aac8260.

(113) McCalla, E.; Sougrati, M. T.; Rousse, G.; Berg, E. J.; Abakumov, A.; Recham, N.; Ramesha, K.; Sathiya, M.; Dominko, R.; Van Tendeloo, G.; Novák, P.; Tarascon, J.-M. Understanding the Roles of Anionic Redox and Oxygen Release during Electrochemical Cycling of Lithium-Rich Layered Li_4FeSbO_6. *J. Am. Chem. Soc.* **2015**, *137* (14), 4804–4814. https://doi.org/10.1021/jacs.5b01424.

(114) Chen, C.-J.; Pang, W. K.; Mori, T.; Peterson, V. K.; Sharma, N.; Lee, P.-H.; Wu, S.; Wang, C.-C.; Song, Y.-F.; Liu, R.-S. The Origin of Capacity Fade in the $Li_2MnO_3 \cdot LiMO_2$ (*M* = Li, Ni, Co, Mn) Microsphere Positive Electrode: An *Operando* Neutron Diffraction and Transmission X Ray Microscopy Study. *J. Am. Chem. Soc.* **2016**, *138* (28), 8824–8833. https://doi.org/10.1021/jacs.6b03932.

(115) Zheng, J.; Gu, M.; Xiao, J.; Zuo, P.; Wang, C.; Zhang, J.-G. Corrosion/Fragmentation of Layered Composite Cathode and Related Capacity/Voltage Fading during Cycling Process. *Nano Lett.* **2013**, *13* (8), 3824–3830. https://doi.org/10.1021/nl401849t.

(116) Bettge, M.; Li, Y.; Gallagher, K.; Zhu, Y.; Wu, Q.; Lu, W.; Bloom, I.; Abraham, D. P. Voltage Fade of Layered Oxides: Its Measurement and Impact on Energy Density. *J. Electrochem. Soc.* **2013**, *160* (11), A2046–A2055. https://doi.org/10.1149/2.034311jes.

(117) Li, Y.; Bareño, J.; Bettge, M.; Abraham, D. P. Unexpected Voltage Fade in LMR-NMC Oxides Cycled below the “Activation” Plateau. *J. Electrochem. Soc.* **2015**, *162* (1), A155–A161. https://doi.org/10.1149/2.0741501jes.

(118) Berg, H.; Zackrisson, M. Perspectives on Environmental and Cost Assessment of Lithium

Metal Negative Electrodes in Electric Vehicle Traction Batteries. *J. Power Sources* **2019**, *415*, 83 90. https://doi.org/10.1016/j.jpowsour.2019.01.047.

(119) Ohzuku, T.; Makimura, Y. Layered Lithium Insertion Material of $LiNi_{1/2}Mn_{1/2}O_2$: A Possible Alternative to $LiCoO_2$ for Advanced Lithium-Ion Batteries. *Chem. Lett.* **2001**, *30* (8), 744–745. https://doi.org/10.1246/cl.2001.744.

(120) Thackeray, M. M. Manganese Oxides for Lithium Batteries. *Prog. Solid State Chem.* **1997**, *25* (1–2), 1–71. https://doi.org/10.1016/S0079-6786(97)81003-5.

(121) Feng, Z.; Rajagopalan, R.; Zhang, S.; Sun, D.; Tang, Y.; Ren, Y.; Wang, H. A Three in One Strategy to Achieve Zirconium Doping, Boron Doping, and Interfacial Coating for Stable $LiNi_{0.8}Co_{0.1}Mn_{0.1}O_2$ Cathode. *Adv. Sci.* **2021**, *8* (2), 2001809. https://doi.org/10.1002/advs.202001809.

(122) Masquelier, C.; Croguennec, L. Polyanionic (Phosphates, Silicates, Sulfates) Frameworks as Electrode Materials for Rechargeable Li (or Na) Batteries. *Chem. Rev.* **2013**, *113* (8), 6552–6591. https://doi.org/10.1021/cr3001862.

(123) Huang, H.; Yin, S.-C.; Kerr, T.; Taylor, N.; Nazar, L. F. Nanostructured Composites: A High Capacity, Fast Rate $Li_3V_2(PO_4)_3$/Carbon Cathode for Rechargeable Lithium Batteries. *Adv. Mater.* **2002**, *14* (21), 1525–1528. https://doi.org/10.1002/adma.200290005.

(124) Mingos, D. M. P.; Baghurst, D. R. Tilden Lecture. Applications of Microwave Dielectric Heating Effects to Synthetic Problems in Chemistry. *Chem. Soc. Rev.* **1991,** *20* (1), 1. https://doi.org/10.1039/cs9912000001.

(125) Singh, S.; Gupta, D.; Jain, V.; Sharma, A. Microwave Processing of Materials and Applications in Manufacturing Industries: A Review. *Mater. Manuf. Process.* **2014,** *29* (8), 795–820. https://doi.org/10.1080/10426914.2014.952028.

(126) Clark, D. E.; Sutton, W. H. Microwave Processing of Materials. *Acta Mater.* **1996,** *46* (3), 921 932. https://doi.org/10.1016/S1359-835X(99)00002-02.

(127) Yang, J.; Tang, K.; He, G.; Wang, Z.; Mu, Y.; Du, G.; Chen, G. Optimal Microwave-Assisted Hydrothermal Synthesis of Nanosized $xLi_2MnO_3 \cdot (1 - x)LiNi_{1/3}Co_{1/3}Mn_{1/3}O_2$ Cathode Materials for Lithium-Ion Battery. *J. Power Sources* **2014,** *247*, 844–851. https://doi.org/10.1016/j.jpowsour.2013.09.015.

(128) Fei, J.; Guo, Z.; Liu, H. K. Microwave Synthesis of Electrode Materials for Lithium Batteries. *J. Mater. Sci.* **2005,** *40* (1), 139–144. https://doi.org/10.1007/s10853-005-5692-9.

Chapter2

Materials and experimental methods

2.1PXRD

In 1912, Laue and colleagues theoretically predicted and experimentally demonstrated that X-rays can undergo diffraction upon interaction with crystals, thereby confirming their electromagnetic wave nature.[1] This discovery marked the first major milestone in the field of X-ray crystallography. When a beam of monochromatic X-rays strikes a crystal, the regularly arranged atomic unit cells within the crystal cause the X-rays scattered by different atoms to interfere with one another. This interference occurs because the spacing between the atoms in the crystal lattice is on the same order of magnitude as the wavelength of the incident X-rays.[2]

Interference produces strong X-ray diffraction in certain special directions. The orientation and intensity of the spatial distribution of diffraction lines are closely related to the crystal structure. This is the basic principle of X-ray diffraction.[3]

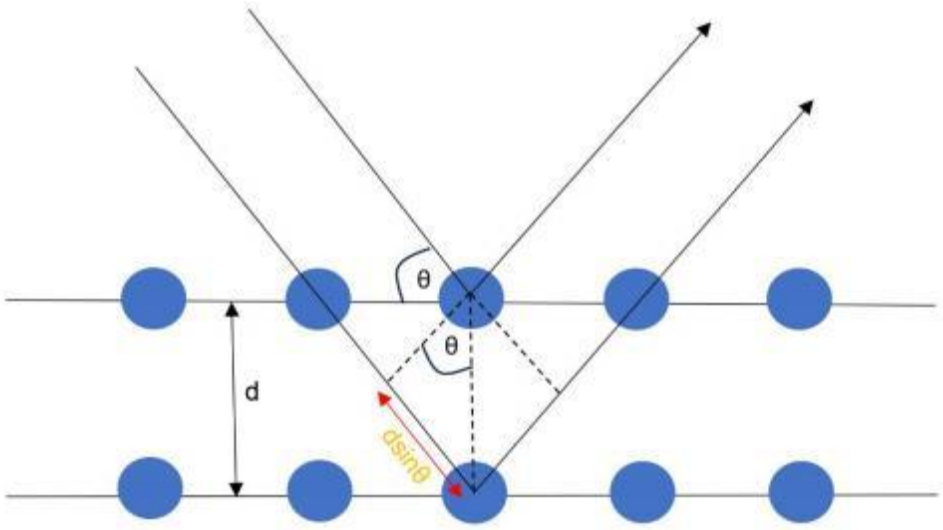

Fig2.1 Geometric schematic of the nλ = 2dsinθ form used to derive Bragg's law.

The relationship between the spatial orientation of the diffraction line and the crystal structure can be expressed by the Bragg equation:

$$n\lambda = 2d \sin(\theta) \quad (2.1)$$

where n signifies the diffracted beam order, λ denotes the incident beam wavelength, d represents lattice spacing, and θ symbolizes the angle of incidence.[4]

X-ray diffraction (XRD) analysis is a method of structural analysis of the spatial distribution of atoms or molecules within a substance using the XRD diffractogram formed by crystals.[2] Every crystalline material exhibits a unique X-ray diffraction pattern, similar to how fingerprints are unique to individuals. This characteristic diffraction pattern serves as a crucial tool for identifying the structure and type of a substance. Through phase analysis using XRD, the crystal phases present can be identified, and their relative quantities can be quantified. As a result, XRD is a fundamental technique for testing if crystalline samples are single- or multi-phase and for resolving new crystal structures. XRD data of different crystals exhibit diffraction peaks with varying intensities at distinct angles (θ). The precise analysis of these diffraction peaks is fundamental for phase identification. When comparing XRD data, key characteristics include the number, position, intensity, and shape of the primary diffraction.

X-ray diffraction follows Bragg's law and is classified into angular dispersion and energy dispersion types. The most commonly used X-ray diffractometer operates on the angular dispersion principle, utilizing quasi-monochromatic incident X-rays. The diffraction pattern, represented as a d-θ curve, is obtained through scanning. In contrast, energy-dispersive X-ray diffraction maintains a fixed diffraction angle (θ) and employs a broad-spectrum of X-rays of varying energy instead of monochromatic X-rays. Additionally, energy-resolved semiconductor detectors replace conventional photon-counting detectors, enabling a one-to-one correlation between the lattice spacing (d) of the material and the corresponding energy (E).

XRD phase analysis includes both qualitative and quantitative analysis.[3] Qualitative analysis is to determine the phase type of the unknown crystal by comparing the measured diffraction data with the standard card data. Quantitative analysis is to calculate the respective content by measuring the integrated diffraction intensity from the crystal when the phase category is known.[3]

After synthesis, the calcined powder was finely ground using an agate mortar and pestle to achieve a uniform particle size. The powder was then carefully packed into a flat sample holder made of low-background silicon to minimize interference during XRD measurements. The surface of the sample was smoothed using a glass slide to ensure a flat and even surface, which is critical for obtaining high-quality XRD patterns.

In this study, X-ray diffraction (XRD) patterns were acquired using a Rigaku Miniflex diffractometer equipped with a Cu Kα radiation source ($\lambda = 1.541$ Å). The instrument was operated at a voltage of 40 kV and a current of 15 mA, with a step size of 0.02° (2θ) over an angular range of 10° to 80° peaks.

2.2 Rietveld refinement

In the field of Powder X-ray Diffraction (PXRD), the identification of key structural parameters, including unit cell dimensions, atomic coordinates and site occupancy, is achieved through a technique called Rietveld refinement. This approach involves a detailed comparison between experimentally obtained diffraction patterns and those generated from a theoretical structural model. The Rietveld refinement process systematically adjusts the theoretical model using least squares optimization to iteratively improve its accuracy. The goal is to reduce the discrepancies between the simulated diffraction profile and the experimental data by refining parameters such as peak width, intensity, profile shape, and position. By minimizing the residual difference between the calculated and observed patterns, the method progressively enhances the agreement between the two. This iterative optimization continues until the simulated pattern closely matches the experimental data, allowing for the extraction of detailed structural information from previously uncharacterized samples.

The optimization process involves iterative adjustments to various structural and instrumental variables, continuing until a minimum value is achieved. Upon completion of this refinement, the resulting structural model can be regarded as an accurate depiction of the actual structure, providing valuable data including unit cell dimensions, volume, atomic coordinates, and site occupancy factors. To evaluate the quality of the refinement and the degree of correspondence between experimental and calculated patterns, specific statistical indicators are utilized. Three key statistical parameters are typically computed: the weighted profile R-factor (R_{wp}), the anticipated R-factor (R_{exp}), and the goodness-of-fit index (χ^2). [6,13] The weighted R-factor is determined through the following calculation:

$$R_{wp} = \sqrt{\frac{\sum w_i(y_{obs,i} - y_{calc,i})^2}{\sum w_i y_{obs,i}^2}} \tag{2.2}$$

In this context, the subscript i denotes the i-th atomic position, where W_i represents a statistical weighting factor derived from the estimated uncertainty of the experimental measurements. The terms

y(obs) and y(calc) correspond to the experimentally obtained and computationally predicted profiles, respectively.

The R_{exp} factor is calculated as:

$$R_{exp} = \sqrt{\frac{N-P}{\sum \bar{w}_i y_{obs,i}^2}} \quad (2.3)$$

In the given equation, N represents the total count of data points while P denotes the number of adjustable parameters. Under typical experimental conditions, the magnitude of N significantly exceeds that of P, thereby predominantly influencing the numerator's value. This mathematical relationship reflects the theoretical lower limit of the R-factor, considering the influence of the dataset's size. Consequently, in cases of accurate profile refinement, the weighted profile R-factor (R_{wp}) is expected to approach the value of the expected R-factor (R_{exp}). [6,13] The quantitative assessment of this agreement can be evaluated through the ratio between these two parameters, yielding the statistical measure of fit quality, expressed as the chi-squared (χ^2) value, which is mathematically defined as:

$$\chi^2 = \frac{R_{wp}}{Rexp} \quad (2.4)$$

To achieve optimal profile refinement results, the refinement quality can be quantitatively assessed through two key indicators: the R-factors should demonstrate minimal values, while the chi-squared (χ^2) statistic should approach unity (1.0) as closely as possible. These criteria collectively serve as essential metrics for evaluating the reliability and precision of the structural refinement process.

In this study, the Rietveld refinement procedure was executed using the least squares method through the GSAS II program (General Structural Analysis System).[6] For PXRD refinement, a general sequence is typically followed: (i) background polynomials, (ii) scale factors, (iii) grain cell parameters, (iv) zeros and sample displacements, (v) profile parameters, (vi) atomic positions, (vii) site occupancies, and (viii) anisotropic displacement parameters. Rietveld refinement of PXRD data

for each sample was undertaken using the GSAS-II program for comprehensive structural analysis and comparison.

2.3 SEM

Scanning electron microscopy (SEM) represents a highly adaptable imaging methodology widely applied for the examination of surface topography, morphological features, and compositional characteristics of various samples. This analytical tool finds extensive application in the evaluation of critical parameters including particulate dimensions, dispersion patterns, porosity attributes, and surface properties. While traditional optical microscopy, with its origins tracing back to the 18th century, has been instrumental in scientific observation, its inherent limitations in achieving the necessary spatial resolution for comprehensive material characterization – primarily due to the restrictions imposed by the visible light spectrum (approximately 400-700 nm) – have driven the evolution of advanced electron microscopy techniques. These sophisticated methods enable surface visualization and analysis at the nanometer scale, significantly enhancing our capacity for material characterization.[7]

Within a scanning electron microscope, an electron gun generates an electron beam by heating a tungsten filament. Subsequently, the accelerated electron beam is directed through a vacuum by means of a potential and directed toward the sample. The potential can be finely tuned in alignment with the experimental requisites, typically encompassing the interval of 0.2 to 30 kV. The wavelength of the electron beam adheres to the de Broglie equation:[8]

$$\lambda = \frac{h}{p} = \frac{h}{\sqrt{2mE}} \tag{2.5}$$

where h denotes Planck's fundamental constant, whereas the variables λ, p, m and E correspond to the electron's wavelength, momentum, electron’s mass and energy, respectively. The selection of electron energy, which directly determines the associated wavelength, is critically dependent on the sample's properties. Specifically, the utilization of reduced energy electrons (characterized by longer wavelengths) proves particularly beneficial when examining radiation-

sensitive or electrically insulating materials. Although the implementation of lower energy beams minimizes potential specimen degradation caused by electron irradiation, this approach concurrently results in diminished spatial resolution owing to the increased wavelength of the probing radiation. Consequently, the optimization of acceleration voltage requires careful consideration of the sample's specific attributes to achieve an optimal compromise between resolution and sample integrity.[8]

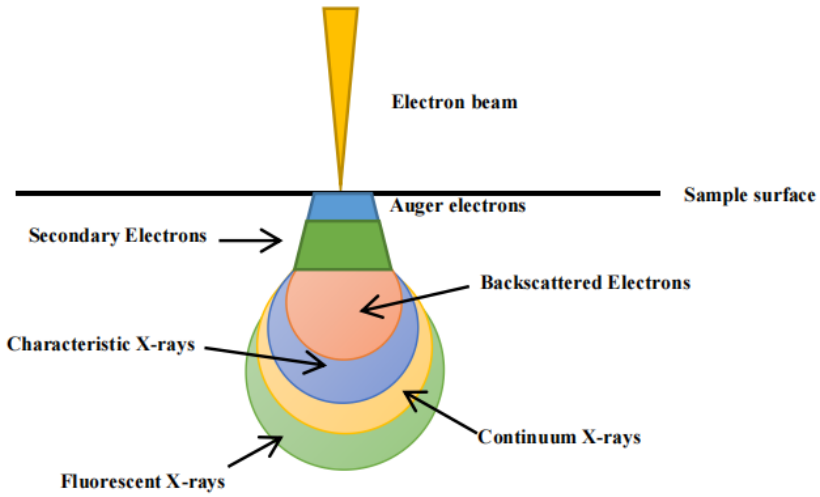

Fig2.2 Electron penetration through the sample surface in SEM.

The electron beam undergoes demagnification through a series of two or three electromagnetic condenser lenses, forming a highly focused probe. This probe is then systematically rastered across the specimen's surface area using precisely controlled scan coils. Upon interaction with the sample, the incident electrons penetrate the material, creating a teardrop-shaped interaction zone (as illustrated in Figure 2.2). The spatial extent of this interaction volume is influenced by several parameters, including the accelerating voltage of the electron beam and the atomic composition of the specimen. Specifically, higher beam energies and lower atomic number elements typically yield greater penetration depths. While the angle of beam incidence has minimal effect on penetration depth, it significantly influences the trajectories of electron scattering and deflection within the sample.[8]

The interaction of the primary electron beam with the specimen generates multiple signal types, each providing distinct analytical information. These include secondary electrons (SE), backscattered electrons (BSE), and Auger electrons, along with characteristic X-rays, continuum X-rays (Bremsstrahlung radiation), and fluorescent X-rays. Backscattered electrons, resulting from elastic scattering events, are particularly valuable for compositional mapping due to their strong dependence on atomic number contrast. Secondary electrons, produced through inelastic scattering processes, are predominantly utilized for surface topography characterization owing to their high surface sensitivity. [9]

Auger electron emission occurs when excited atoms undergo non-radiative relaxation, providing elemental-specific information through their characteristic energy spectra. The generation of characteristic X-rays follows the ionization of inner-shell electrons and subsequent electron transitions from higher energy levels, with the emitted photon energy being unique to each element. Continuum X-rays, produced through the deceleration of electrons in the Coulomb field of atomic nuclei, exhibit a broad energy spectrum and are primarily used for studying beam-sample interactions rather than direct elemental analysis.[9]

Fluorescent X-rays represent a specific category of characteristic X-rays, generated through secondary excitation processes where X-ray photons induce electron transitions. These signals complement the information obtained from primary characteristic X-rays and contribute to the analysis of background radiation in X-ray spectra. The combined detection and analysis of these various signals enable comprehensive characterization of the specimen's composition, structure, and surface properties.[9]

Scanning electron microscope images were obtained utilizing an FEI Inspect F50 scanning electron microscope, with voltage settings ranging from 5 to 20 kV. Sample preparation involved affixing powdered samples onto conductive carbon substrates, subsequently mounted onto aluminium pillars, and coated with a layer of sputtered gold to enhance conductivity to avoid surface charging under the electron beam.

2.4 Galvanostatic Cycling

In assessing materials for use in lithium-ion batteries, such as electrodes and electrolytes, the evaluation of their practical performance is of paramount importance. A widely employed electrochemical testing method is constant current cycling with potential limitation (GCPL). This technique mirrors the operational conditions of commercial batteries, offering comprehensive characterization under diverse current rates and potential limitations, thus mimicking real-world battery usage.[10]

Galvanostatic cycling involves maintaining a fixed current throughout the process, whereas potentiostatic operation is confined within specified voltage boundaries. The cathode undergoes electrochemical cycling by applying an anodic current, which systematically increases the cell potential to its maximum value at a rate governed by the applied current density. When the upper voltage boundary is attained, the current direction is inverted, facilitating electron removal from the anode material. During this process, as electrons migrate through the external circuit, the cell potential gradually decreases until it reaches the minimum threshold, thereby completing a single charge-discharge cycle of the electrochemical cell.

For the anode material, charging results in delithiation, whereas discharging leads to reversible lithiation. Battery capacity, signifying the stored charge (energy), is measured in C kg^{-1} or $mAhg^{-1}$. This specific capacity metric facilitates facile material comparison. A material's theoretical capacity hinges upon the number of mobile ions it accommodates, which is related to its lithium extraction/insertion capability and molecular mass.

The theoretical capacity (Q) can be calculated using the form:

$$Q = \frac{nF}{M_W} \tag{2.6}$$

where n signifies the amount of Li^+ stored within the active material, F is Faraday's constant, and Mw denotes the mass of the active material in C kg^{-1}. Actual capacity is determined from the

current overtime and the active material's mass. A close correlation between specific capacity during cycling and theoretical capacity is desirable; deviations may indicate sample issues.[8]

The term "C-rate" defines cycling rates, with 1C denoting a complete cell capacity addition/removal within an hour. GCPL assesses battery performance under elevated currents, expressed as Ch^{-1},where C signifies the cell charge for full electrode reduction/oxidation, and h represents the time in hours.

The constant current cycling experiments in this study employed 2032 coin cell（A 2032 coin cell is a small, round, flat battery that looks like a tiny coin (hence the name "coin cell"). The cells were assembled with specific materials, including electrode pellets (active material: carbon black: PVDF in a 80:10:10 weight ratio), Whatman glass microfibre septums, and 1 M $LiPF_6$ ethylene carbonate (EC) and dimethyl carbonate (DMC)(3:7) solution as electrolyte.

2.5 Inductively Coupled Plasma Atomic Emission Spectroscopy

Atomic spectroscopic techniques, such as optical spectroscopy, X-ray spectroscopy, and mass spectrometry, are among the most effective methods for detecting inorganic elements. Inductively Coupled Plasma Atomic Emission Spectroscopy (ICP-OES) combines the strengths of atomic emission spectroscopy (AES) with the capability for simultaneous multi-element analysis, offering high sensitivity and accuracy in elemental detection.[11]

ICP-OES offers several advantages, including a broad linear dynamic range and the ability to simultaneously detect primary, secondary, and trace elements. It is well-suited for the direct analysis of solid, liquid, and gaseous samples, enabling multi-element detection across multiple spectral lines.

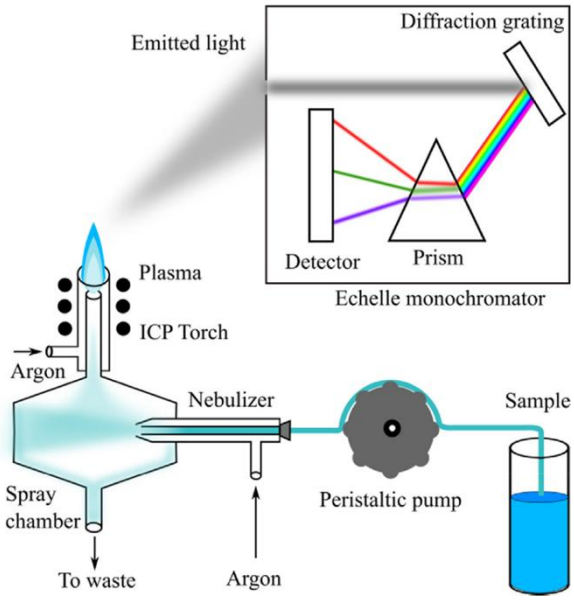

Fig2.3 Simplified scheme demonstrating the basic operating principles of ICP-OES. Reprinted with the permission from ref 14. Copyright 2018, Elsevier Inc.

The operational principle of ICP-OES involves first converting the sample into a liquid state, which is then delivered to the plasma generator via a pumping system. Within the plasma generator, an electric discharge excites argon or nitrogen gas, producing a high-temperature plasma composed of energetically excited gas atoms and ions.[11,12]

When the sample is introduced into the plasma, its constituent elements are energized by collisions with high-energy electrons, transitioning to excited states. Upon returning to their ground

states, these excited elements emit light at characteristic wavelengths, known as emission spectral lines. Each element possesses a unique set of emission lines. Spectroscopic instruments detect and analyze these spectral lines to determine elemental composition. By measuring the intensity and wavelength of the emitted light, the concentration of each element can be accurately quantified.[14] ICP-OES is a very precise and sensitive analytical technology widely used in metal analysis. By measuring the spectral lines of elements, ICP-OES can analyze multiple elements simultaneously and provide accurate chemical composition information. In this research, the ICP-OES experiments were completed by Dr.Innes McClelland on my behalf in Material Science and Engineering Department.

References

(1) Authier, A. Disputed Discovery: The Beginnings of X-ray Diffraction in Crystals in 1912 and Its Repercussions. Acta Crystallogr. A **2012**, 68 (1), 1–9. https://doi.org/10.1107/S0108767311043953.

(2) Lu, C.; Huang, J.; Wang, S.; Yang, J.; He, S. Ultrathin and Broadband Graphene Metamaterial Absorber. *Opt. Express* **2014,** *22* (10), 11930–11939. https://doi.org/10.1364/OE.22.011930.

(3) Bréger, J.; Jiang, M.; Dupré, N.; Meng,Y. S.; Shao-Horn,Y.; Ceder, G.; Grey, C. P. High-Resolution X- Ray Diffraction, DIFFaX, NMR and First Principles Study of Disorder in the Li_2MnO_3– $Li[Ni_{1/2}Mn_{1/2}]O_2$ Solid Solution. *J. Solid State Chem.* **2005**, *178* (9), 2575–2585. https://doi.org/10.1016/j.jssc.2005.05.027.

(4) Kaduk, J. A.; Billinge, S. J. L.; Dinnebier, R. E.; Henderson,N.; Madsen,I.; Černý, R.; Leoni, M.;Lutterotti, L.; Thakral, S.; Chateigner, D. Powder Diffraction. Nat. Rev. Methods Primer 2021, 1 (1), 1–22. https://doi.org/10.1038/s43586-021-00074-7.

(5) Toby, B. H.; Von Dreele, R. B. GSAS-II: The Genesis of a Modern Open-Source All Purpose Crystallography Software Package. J. Appl. Crystallogr. 2013, 46 (2), 544–549. https://doi.org/10.1107/S0021889813003531.

(6) Toby, B. H. R Factors in Rietveld Analysis: How Good Is Good Enough? Powder Diffr. 2006, 21 (1), 67–70. https://doi.org/10.1154/1.2179804.

(7) Goldstein, J.; Newbury, D.; Joy, D.; Lyman, C.; Echlin, P.; Lifshin, E.; Sawyer, L.; Michael, J. *Scanning Electron Microscopy and X-Ray Microanalysis ISBN: 0306472929*; **2003**; Vol. XIX. https://doi.org/10.1007/978-1-4615-0215-9.

(8) Egerton, R. F. Scanning Electron Microscopy (SEM) and Transmission Electron Microscopy (TEM) for Materials Characterization. *Nanostructure Science and Technology* **2016**, 3–37. https://doi.org/10.1007/978-3-319-26651-0_1.

(9) Inkson, B. J. Scanning Electron Microscopy (SEM) and Transmission Electron Microscopy (TEM) for Materials Characterization. In *Materials Characterization Using Nondestructive*

Evaluation (NDE) Methods; Hubschen, G., Altpeter, I., Tschuncky, R., Herrmann, H.-G., Eds.; Woodhead Publishing, **2016**; pp 17-43. https://doi.org/10.1016/B978-0-08-100040-3.00002-X.

(10) Borkiewicz, O. J.; Shyam, B.; Wiaderek, K. M.; Kurtz, C.; Chupas, P. J.; Chapman, K. W. The AMPIX Electrochemical Cell: A Versatile Apparatus for in Situ X-Ray Scattering and Spectroscopic Measurements. *J. Appl. Crystallogr.* **2012**, *45* (6), 1261–1269. https://doi.org/10.1107/S0021889812042720.

(11) Nishiguchi, K.; Utani, K.; Fujimori, E. Real-Time Multielement Monitoring of Airborne Particulate Matter Using ICP-MS Instrument Equipped with Gas Converter Apparatus. *J. Anal. At. Spectrom.* **2008**, *23* (8), 1125. https://doi.org/10.1039/b802302f.

(12) Kröger, T.-N.; Wiemers-Meyer, S.; Harte, P.; Winter, M.; Nowak, S. Direct Multielement Analysis of Polydisperse Microparticles by Classification-Single-Particle ICP-OES in the Field of Lithium-Ion Battery Electrode Materials. *Anal. Chem.* **2021**, *93* (20), 7532–7539. https://doi.org/10.1021/acs.analchem.1c01283.

(13) Rietveld, H. M. A Profile Refinement Method for Nuclear and Magnetic Structures. J. Appl. Crystallogr. **1969**, 2 (2), 65–71.https://doi.org/10.1107/S0021889869006558.

(14) Cherevko, S.; Mayrhofer, K. J. J. On-Line Inductively Coupled Plasma Spectrometry in Electrochemistry: Basic Principles and Applications. Encyclopedia of Interfacial Chemistry **2018**, 326–335. https://doi.org/10.1016/B978-0-12-409547-2.13312.

Chapter 3

Solid state synthesis exploration of layered Li_2NiO_3- $LiNiO_2$ cathodes for LIBs

3.1 Introduction

With the increasing energy demand, the layered lithium-rich and ultrahigh nickel-content (Li-rich high-Ni) cathode materials have attracted considerable attention because of their high capacity and high working voltage. To overcome the limitations of $LiCoO_2$ cathodes, alternative transition metals (e.g., Ni, Mn) are being investigated as substitutes for Co. These substitutions aim to enhance Li^+ diffusivity, increase specific capacity through oxygen redox activity and phase evolution, and address the economic, environmental, and ethical challenges posed by cobalt reliance.[1] In addition to lowering costs and increasing capacity, partial substitution of Ni for Co in the cathode material can also improve electrochemical performance and energy density. For instance, NMC811 has 217 $mAhg^{-1}$ at a current density of 10 mAg^{-2}.[2] To tackle the higher demand for volume-constrained applications[3], volumetric energy density is taken into to consideration. This concept is closely linked to the structure of the materials, including their particle size and distribution.[4]

However, the Li-rich high-Ni materials confront a series of degradation processes, including the release of oxygen (especially for the initial charge/discharge cycle), migration of the transition metals (causing Li/Ni mixing), surface layer deconstruction[5], structural transformation, decomposition reactions with the electrolyte[6] and particle cracking.[7] These processes ultimately lead to significant decay in capacity and voltage, as well as inadequate cycling stability. Due to the inability to fully remove lithium, the presence of oxygen loss, the significant irreversible capacity of materials, and phase change all contribute to the inferior cycling performance.[8]

Solid-state synthesis is a cost-effective and environmentally benign alternative to sol-gel or hydrothermal/solvothermal routes for cathode material fabrication, offering advantages in process simplicity and scalability.[9,10]

Solid-state synthesis has become a widely adopted technique for fabricating lithium-rich and Mn/Ni-based cathode materials, such as $LiNiO_2$ and Li_2MnO_3. However, precise control of synthesis parameters, particularly stoichiometric ratios, remains challenging. Critical material characteristics including morphology, particle size distribution, and cation ordering - all of which significantly affect electrochemical performance - are strongly dependent on processing conditions such as thermal treatment profiles, lithium excess amounts, and final calcination temperatures.[11]

The optimization of solid-state synthesis conditions for Li_2NiO_3 cathodes was comprehensively addressed in Bianchini's work[12], with particular emphasis on electrochemical performance enhancement. After establishing the fundamental importance of pre-treatment steps, the research delineates four key optimization parameters: precursor materials, lithium excess ratio, temperature ramp rates, and optimal calcination parameters.

3.2 Synthesis of Li_2NiO_3

For the preparation of Li_2NiO_3, stoichiometric amounts of nickel hydroxide and lithium hydroxide (2:1 molar ratio) were thoroughly mixed via manual grinding using quartz tools for 30 minutes. Following homogenization, the precursor mixture was transferred to an alumina crucible (20 mL capacity) and processed in an oxygen furnace under the following thermal regime: initial dehydration at 300°C (12 h), followed by high-temperature calcination at 550°C (24 h), and finally gradual cooling to 200°C(as shown in Fig3.1).[12] The calcined samples were placed inside an Ar-filled glovebox with a low concentration of H_2O (<0.1ppm) and O_2 (<0.1ppm) to prevent any potential interaction with carbon dioxide and moisture during storage.

Multiple interdependent factors govern the material's phase formation and morphological evolution during calcination. Systematic optimization requires careful control of: (1) preheating protocol, (2) dwell time, (3) $Ni(OH)_2$ precursor characteristics, (4) lithium excess ratio, (5) heating/cooling gradients, and (6) target temperature set points.

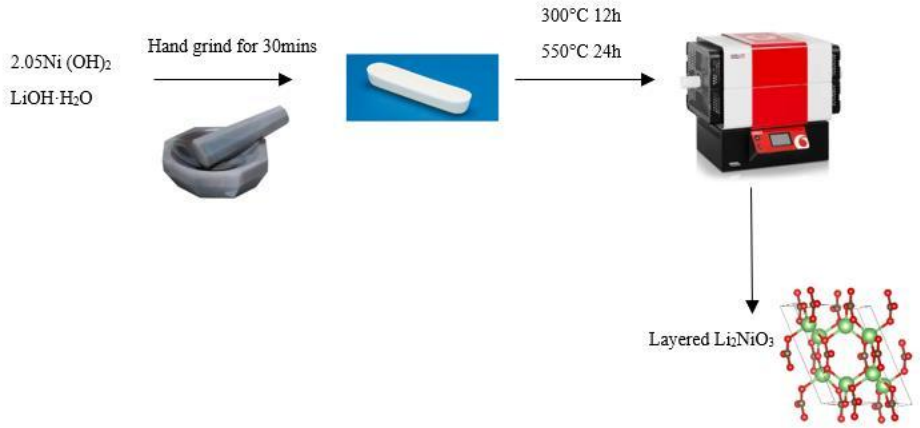

Fig 3.1 Reaction scheme used for the solid-state synthesis of Li_2NiO_3.

3.3 Calcination optimization with/without preheat treatment, and short/long time procedure.

3.3.1 Introduction and experimental design

The length of the calcination process affects the lattice parameters in the structure as well as the crystallinity of high nickel content cathode materials.[13] In addition, a brief calcination period might occasionally lead to incomplete reactions and the development of impurity phases.[14]

Three distinct thermal processing routes were investigated to optimize Li_2NiO_3 synthesis: (i) no preheating step, (ii) abbreviated calcination, and (iii) standard protocol. Material characterization focused on phase purity, particulate properties, and crystallographic features. The conventional thermal treatment replicated Bianchini's methodology, employing a 300°C/12 h preheating stage preceding 550°C/24 h calcination.[12] The abbreviated calcination procedure involves preheating at a temperature of 300°C for a duration of 12 hours, followed by calcination at a temperature of 550°C for 12 hours. In contrast, the non-preheated condition is subjected to calcination at a

temperature of 550°C for 24 hours. All of the samples have a 5% surplus of lithium derived from LiOH sources.[15]

3.3.2 SEM

Upon comparison of the SEM images of the three samples, irregular geometric particle shapes are evident in Figure 3.2a and 3.2b. These samples, which underwent short calcination without preheating, were subjected to brief low-temperature calcination, resulting in impurity formation and poor crystallization.[12]

Samples (a) and (b) consist of relatively large secondary particles (5–10μm). Under standard preheating and calcination conditions, the secondary particles become slightly larger and exhibit agglomeration, a trend that contrasts with the findings of Bianchini et al. (see Figure 3.1).[12] In contrast to Bianchini's findings[12], the secondary particles are smaller—that is, 5–10μm as opposed to 5–20 μm.

Smaller particles reduce the Li^+ diffusion path length, improving ion conduction—particularly for the poorly conductive Li_2NiO_3 phase—and enhancing the material's electrochemical performance, especially its rate capability. Additionally, the increased specific surface area and higher density of active sites in smaller particles further promote electrochemical activity. The material also demonstrates superior cycling stability due to better accommodation of volume changes during Li^+ deintercalation.[15-19]

On the other hand, a low volume specific capacity is detrimental to electrochemical processes, while high specific surface areas might offer additional chances for side reactions with the electrolyte.[20,21]

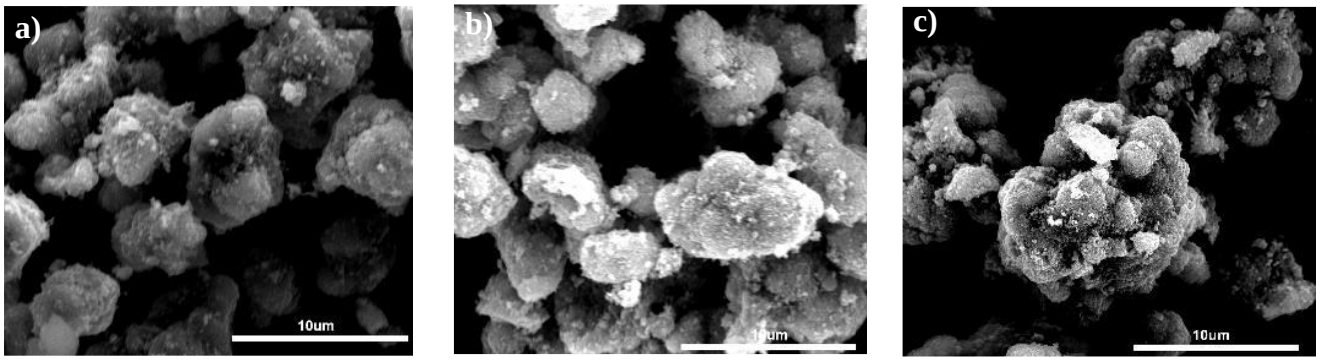

Fig3.2 SEM images for Li_2NiO_3 samples with; (a) short calcination (300°C 12h, and 550°C 12h); (b) no preheat treatment (550°C, 24h) compared with; (c) preheat and calcination condition (300°C 12h, and 550°C 24h).

3.3.3 ICP-OES

Table3.1 Chemical content for the Li_2NiO_3 sample (Data from Dr.Innes McClelland, University of Sheffield). Note: data supplied without errors on the values.

Sample	Li	Ni	Li/Ni	Result
Li_2NiO_3(5% Li excess)	1.97	1.03	1.91	$Li_{1.97}Ni_{1.03}O_3$

The stoichiometric ratios of the synthesized powder samples were determined using a 5% Li excess to compensate for potential volatilization losses. The thermal treatment protocol consisted of heating and cooling cycles at a controlled rate of $3°Cmin^{-1}$. Prior to calcination, the samples were preheated at 300°C for 12 h to remove volatile impurities, followed by calcination at 550°C for 24 h under static air. ICP-OES analysis confirmed the final stoichiometry as $Li_{1.97}Ni_{1.03}O_3$, indicating a lithium deficiency (Li < 2.00). This deviation from the ideal stoichiometry may arise from incomplete reaction kinetics due to insufficient Li precursor availability or suboptimal calcination temperature, leading to partial incorporation of Li into the lattice. In addition, cathode materials containing a significant amount of nickel have a modest difference in ionic radius between Li^+ (0.76 Å) and Ni^{2+} (0.69 Å), which leads to the unpredictability of Ni^{3+} and Ni^{4+} at elevated temperatures during the

synthesis process.[23,24] The presence of Ni^{2+} ions in the lithium layer is expected to hinder Li^{+} diffusion due to the shorter Ni–O bond length compared to Li–O. This structural distortion reduces the interlayer spacing, negatively affecting rate capability. Furthermore, Ni^{2+} occupation of Li sites decreases the reversible specific capacity by blocking Li^{+} migration pathways. Additionally, prolonged cycling may aggravate cation mixing, promoting surface reconstruction into a rock-salt-like phase. This disordered phase further degrades Li^{+} diffusivity, exacerbating kinetic limitations.

3.3.4 X-ray diffraction and Rietveld analysis

As evidenced by the PXRD patterns in Figure 3.3, the diffraction peaks closely match the reference ICSD153094 standard, confirming the target phase formation. However, the sample subjected to shorter calcination displays additional reflections at 30–32° (marked by stars in Figure 3.3b), which were identified as residual Li_2CO_3 impurities. In contrast, prolonged calcination significantly reduces these secondary phases, yielding a purer Li_2NiO_3 product. This suggests that extended thermal treatment enhances phase homogeneity by promoting complete decomposition of lithium carbonate.

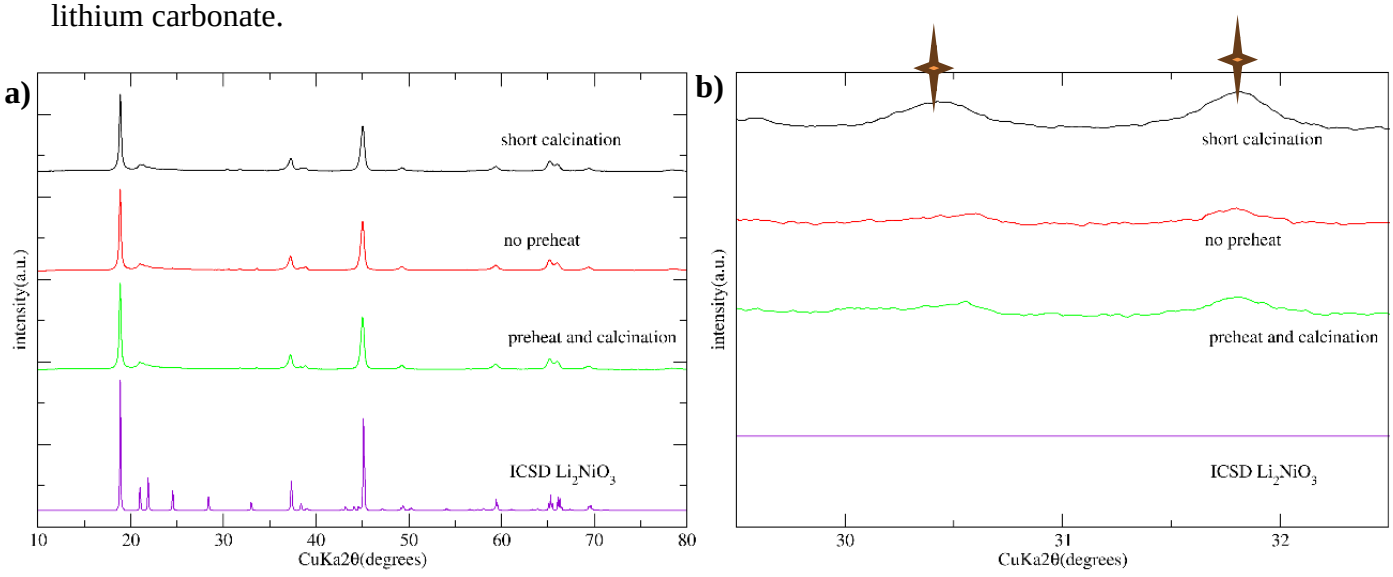

Fig3.3 (a) PXRD patterns of Li_2NiO_3 with short calcination set, no preheating set and normal heating and calcination; b) enhanced scale figure from 30-32° to highlight the Li_2CO_3 ICSD66941 with impurity shown in the image.[25]

The Rietveld refinement results (Fig. S3.1) confirm successful indexing to the monoclinic C2/m Li_2NiO_3 structure, demonstrating satisfactory cell parameters and structural integrity. Comparative analysis reveals that the sample prepared without preheating and with shortened calcination exhibits significantly reduced (110) peak intensity relative to conventionally processed specimens. This is further evidenced by the decreased I(110)/I(020) intensity ratio, which according to Boulineau et al.[27,28] serves as an indicator of cation disorder and stacking faults along the c-axis.

Notably, while the I(110)/I(020) ratios remain comparable between non-preheated and standard processed samples, suggesting similar degrees of Li/Ni ordering and stacking defects, distinct differences emerge in the 21.3-31.8° range. The non-preheated sample displays markedly stronger Li_2CO_3 impurity peaks, as clearly visible in Figure 3.3b. These observations demonstrate that residual lithium carbonate persists during early synthesis stages but gradually diminishes with prolonged calcination. The results underscore the critical importance of both preheating and extended high-temperature treatment under oxygen atmosphere for the formation of phase-pure Li_2NiO_3.

According to Table S3.1, the ratio of a to b falls when going from brief calcination to regular preheating and calcination. This strongly suggests that the crystal structure of the material changed from trigonal to monoclinic. The monoclinic Li_2NiO_3 crystal exhibits a 1:2 ratio of ordered Li and Ni on the ab plane, resulting in a deviation of the a/b value of Li_2NiO_3 from that of α-$NaFeO_2$.[27]

Based on the Scherrer equation, the three samples in the 20 nm range have similar sizes, as indicated in Table S3.1. However, there is an increasing trend in size from the short calcination to preheat and calcination, ranging from 18 to 21 nm. This suggests that longer calcination time leads to larger particle sizes and improved crystallinity.

The refined site occupancies presented in Table S3.2(b) reveal notable variations in Ni distribution among the 4g, 2b, and 2c crystallographic positions. Specifically, the 4g site exhibits sub-stoichiometric Ni occupancy that progressively increases with processing time, whereas the 2b site shows supra-stoichiometric occupation compared to the ideal Li_2NiO_3 structure. Notably, samples

subjected to conventional preheating and calcination protocols display a marked decrease in Ni occupancy at the 4h site, approaching the theoretical value. This behavior suggests that during high-temperature processing under oxygen-rich conditions, partial Li loss occurs, leading to the formation of oxygen vacancies. Concurrently, oxidation of Ni to higher valence states facilitates the incorporation of additional oxygen atoms, effectively compensating for some of the oxygen vacancies created.[12]

These structural refinements indicate that the standard preheating/calcination method yields a product more closely resembling the ideal Li_2NiO_3 phase. This conclusion is further supported by the superior agreement factor (g_{total}= Ni content values per chemical formula) obtained for preheated samples, which approaches the theoretical value. The collective evidence underscores the critical importance of both preheating and optimized calcination duration in oxygen atmosphere for obtaining phase-pure materials with desired structural characteristics.

3.3.5 Conclusion

The systematic investigation reveals two critical parameters for optimal Li_2NiO_3 synthesis: (1) implementation of a preheating stage and (2) extension of calcination duration. Prolonged thermal treatment at 550°C promotes three significant improvements: (i) substantial reduction of residual impurities (Li_2CO_3), (ii) enhancement of crystalline ordering, and (iii) progressive particle growth. Furthermore, extended calcination facilitates the oxidation of nickel from Ni^{2+} to Ni^{4+}, accompanied by a structural transition from trigonal to monoclinic symmetry.

Based on these findings, the optimal synthesis protocol comprises sequential thermal treatment at 300°C (12 h) followed by calcination at 550°C (24 h) under oxygen atmosphere. Future studies will focus on additional parameter optimization to further improve the phase purity and electrochemical properties of Li_2NiO_3.

3.4 Calcination optimization for precursor $Ni(OH)_2$: low, mid, and high ammonium hydroxide solution concentration

3.4.1 Introduction and experimental design

The ammonia concentration in the co-precipitation process is a critical parameter, known to influence the morphology, particle size distribution, and ultimately the electrochemical properties of transition metal oxides.[29,30]

To systematically study these effects, three $Ni(OH)_2$ precursors were synthesized using low (1:2), medium (1:2.4), and high (1:3.75) NH_4OH ratios in a continuous stirred-tank reactor (CSTR). These precursors were subsequently mixed with LiOH (5% excess Li) and calcined under controlled conditions:

- Preheating: 300°C for 12 h
- Calcination: 550°C for 24 h (heating/cooling rate of 3°C/min)

This approach was designed to evaluate the impact of the precursor composition on the final Li_2NiO_3 product and identify optimal synthesis conditions.

3.4.2 SEM

Comparative analysis of the morphological features in Fig. 3.3(a-c) reveals distinct particle aggregation behaviour among the synthesized samples. The particle size of secondary particles was evaluated using ImageJ software based on high-resolution scanning electron microscopy (SEM) images. The image, which included a scale bar of 5 μm, was first calibrated in ImageJ by drawing a reference line across the scale and assigning the corresponding real-world distance. Following calibration, the image was converted to 8-bit grayscale and the contrast was adjusted to enhance the visibility of particle edges. Noise reduction techniques such as smoothing and median filtering were applied to improve image clarity, and thresholding was used to binarize the image. To resolve

agglomerated structures, the watershed algorithm was employed, effectively separating overlapping particles.

Subsequently, the “Analyze Particles” function in ImageJ was used to extract quantitative information including the equivalent circular diameter (ECD) of each particle. Over 100 secondary particles were measured to ensure statistical reliability.

The extracted particle size data were further processed using OriginPro software to construct frequency distribution histograms. Initially, the raw data were grouped into bins based on primary particle diameter intervals, and the corresponding frequency percentages were calculated. To visualize the data, a column chart (histogram) was plotted, where the x-axis represented the primary particle diameter (nm) and the y-axis indicated the frequency percentage of the 100 measured particles. Error bars were incorporated into the histogram to reflect the statistical variability within each bin. The standard error for each group was calculated based on the standard deviation and the number of particles within the corresponding size range. These standard error values were then imported into Origin and assigned as y-axis error bars through the "Plot Details" dialog under the "Error Bars" section. To better illustrate the particle size distribution, a Gaussian fitting curve was superimposed onto the histogram using the "Fit Gaussian" function within Origin. This fitting provided a smooth profile highlighting the degree of uniformity in the synthesized nanoparticles. Overall, the resulting plot clearly demonstrated the narrow particle size distribution, consistent with the uniform morphology observed in the SEM images. Based on the statistical analysis, the average particle size was found to be approximately 17 nm, indicating the successful synthesis of nanoscale materials with uniform morphology.

The low- and mid-NH_3 concentration samples demonstrate pronounced particle reunion, whereas the high-NH_3 sample shows controlled agglomeration of crystallites with an average diameter of 17 nm - significantly smaller than the 100 nm crystallites reported by Bianchini et al.[12]

Scanning electron microscopy (SEM) characterization confirms this size-dependent morphological evolution across all samples.

Notably, all three samples exhibit hierarchical structures composed of: (i) primary particles (15-20 nm diameter) and (ii) secondary particles (5-10 μm aggregates).

The low- and mid-NH_3 derived materials possess quasi-spherical secondary particles with mean diameters of approximately 10 μm. In contrast, the high-NH_3 sample maintains uniform spherical morphology (Fig. 3.4a-c), consistent with previous reports on optimized synthesis conditions. [12]

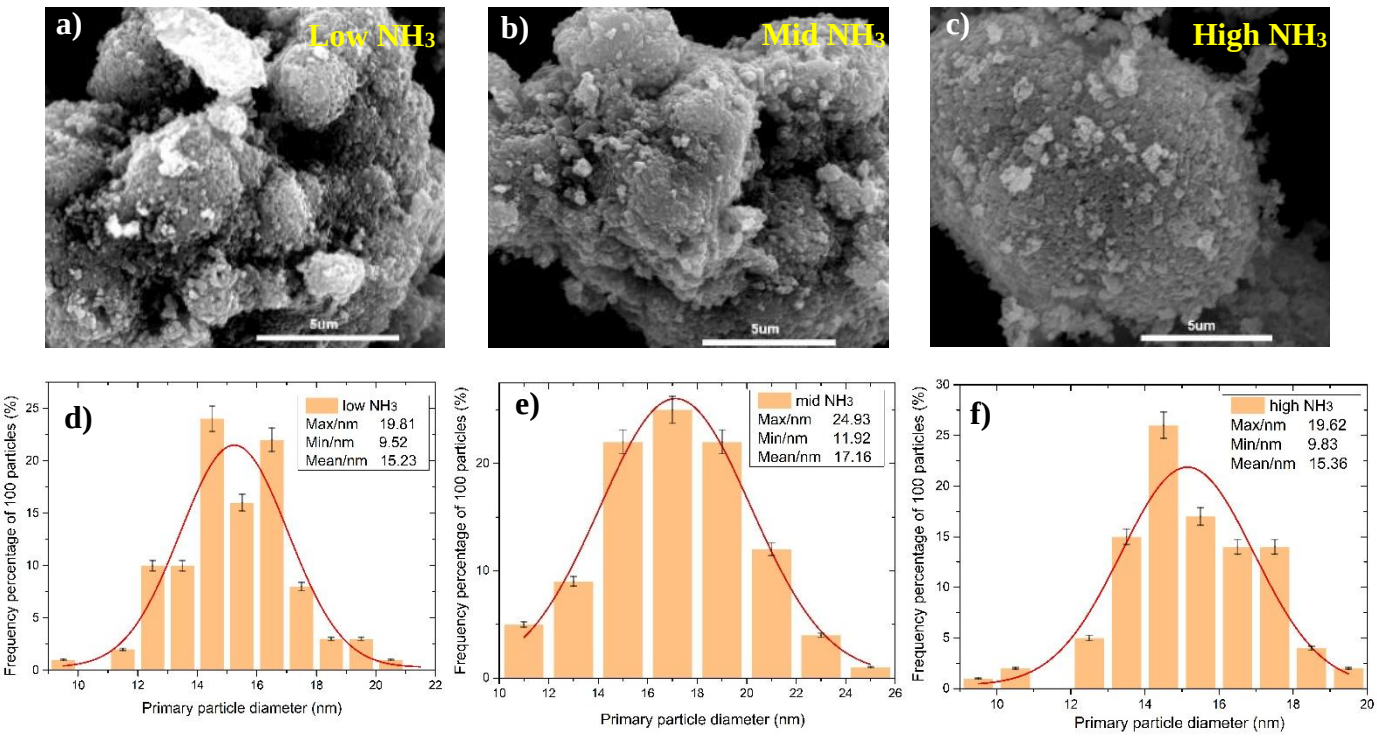

Fig3.4 SEM images (a,b, c) and particle size distribution (d, e, f) of all as-prepared samples.

3.4.3 X-ray diffraction and Rietveld analysis

Figure 3.5 (a) presents the PXRD patterns of Li_2NiO_3 synthesized from precursors prepared with the different NH_3 concentrations. All diffraction peaks can be indexed to the monoclinic phase (space group C2/m), confirming the successful formation of the target Li_2NiO_3 phase.

Close examination reveals that the sample prepared with lower NH_3 concentration shows minimal impurity phases, as evidenced by the absence of secondary peaks at 21.3°, 30.6°, and 31.8°. In contrast, the intermediate-NH_3 derived sample displays detectable impurity reflections at these angular positions, which may account for its compromised electrochemical performance (discussed in Section 3.4.4). The phase purity correlates directly with the NH_3 concentration employed during precursor synthesis.

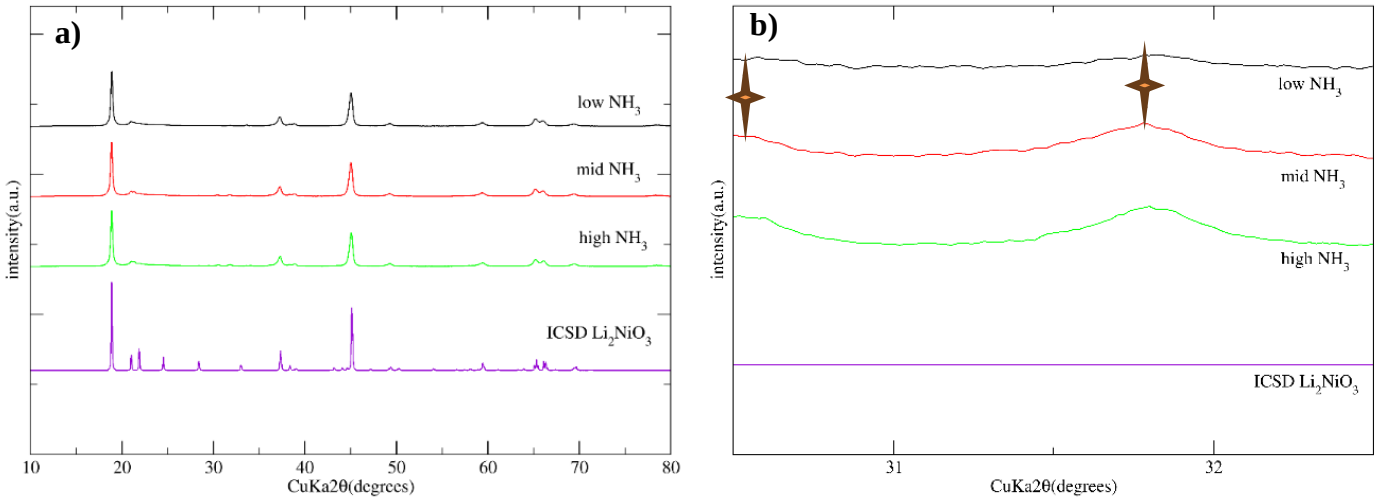

Fig3.5 (a)PXRD patterns of Li_2NiO_3 with low, mid, and high ammonia solution concentration; (b) enhanced scale figure from 30-32°to highlight the Li_2CO_3 ICSD66941 with impurity shown in the image.[25]

When comparing the ratio of I(110)/I(020), it is observed that the low NH_3 sample has the highest value, while the mid NH_3 sample has the lowest value. This difference in values can be attributed to the presence of impurities, since a higher impurity content leads to more Li/Ni mixing and more stacking defects.

The Scherrer equation was used to calculate the crystallite size of the three samples mentioned earlier.[31] The results are presented in Table S3.2, showing a minimal difference of only 1nm in size, which is considered to be very modest. The determined lattice parameters are presented in Table S3.2. The values of a, b, c and the volume exhibit minimal variation, indicating that the selection of the precursor has a negligible effect on the size and purity aspects.

According to Table S3.2, the Ni occupancy site 4g has a value that is similar for all three samples, and it is close to the standard value. The 2b value for low NH_3 has the highest value, which is different from the standard value. On the other hand, the 4h value has the smallest value, which is also close to the standard value. The g_{total} values exhibit a high degree of uniformity and closely align with the expected standard value.[12]

3.4.4 Electrochemical testing

All samples were subjected to identical thermal treatment protocols consisting of:

(i) 12 h preheating at 300°C,

(ii) subsequent calcination at 550°C for 24 h under oxygen atmosphere,

(iii) with 5% stoichiometric lithium excess to compensate for volatilization losses, and

(iv) controlled heating/cooling rates of 3°C/min.

The electrochemical properties were systematically evaluated for three distinct precursor-derived samples, designated as:

- Li_2NiO_3-L (low-NH_3 concentration precursor)
- Li_2NiO_3-M (intermediate-NH_3 concentration)

• Li_2NiO_3-H (high-NH_3 concentration)

The Li_2NiO_3-L, Li_2NiO_3-M and Li_2NiO_3-H are similar samples, which are part of $LiMO_2$–Li_2MnO_3 solid solution (M = $Ni_{1/2}Mn_{1/2}$, $Ni_{1/3}Mn_{1/3}Co_{1/3}$)[32-33], exhibit comparable starting charge and discharge curves. The voltage profile during the first cycle demonstrates a gradual slope with a brief plateau at 4.5 V for the extraction of Li_2O[9], which is comparable to the findings reported by Styanova for $LiNiO_2$–Li_2NiO_3.[34]

The electrochemical profile of the prepared sample exhibits a characteristic plateau at 4.75 V during the initial charging cycle (Fig. 3.6a), corresponding to oxygen evolution from the crystal lattice. This phenomenon, previously reported in similar layered oxide systems[12,35], originates from coupled lithium extraction and oxygen loss processes. As Li^+ ions are removed from the Li_2NiO_3 structure, charge compensation occurs through oxidation of nickel ions ($Ni^{3+} \rightarrow Ni^{4+}$), simultaneously triggering the decomposition of unstable LiO_2 intermediates. The resulting oxygen release leads to irreversible formation of Li_2O surface phases and bulk oxygen vacancies. During subsequent discharge, transition metal ions migrate into these vacancy sites, creating structural distortions that trap lithium ions in modified coordination environments[8]. This irreversible structural evolution accounts for the observed first-cycle capacity loss of 25-30%, manifested through the gradual disappearance of the 4.75 V plateau in subsequent cycles. The permanent capacity fade correlates with X-ray diffraction evidence of peak broadening and differential capacity analysis showing progressive redox peak shifts[12], collectively indicating an irreversible phase transformation upon initial lithium extraction.

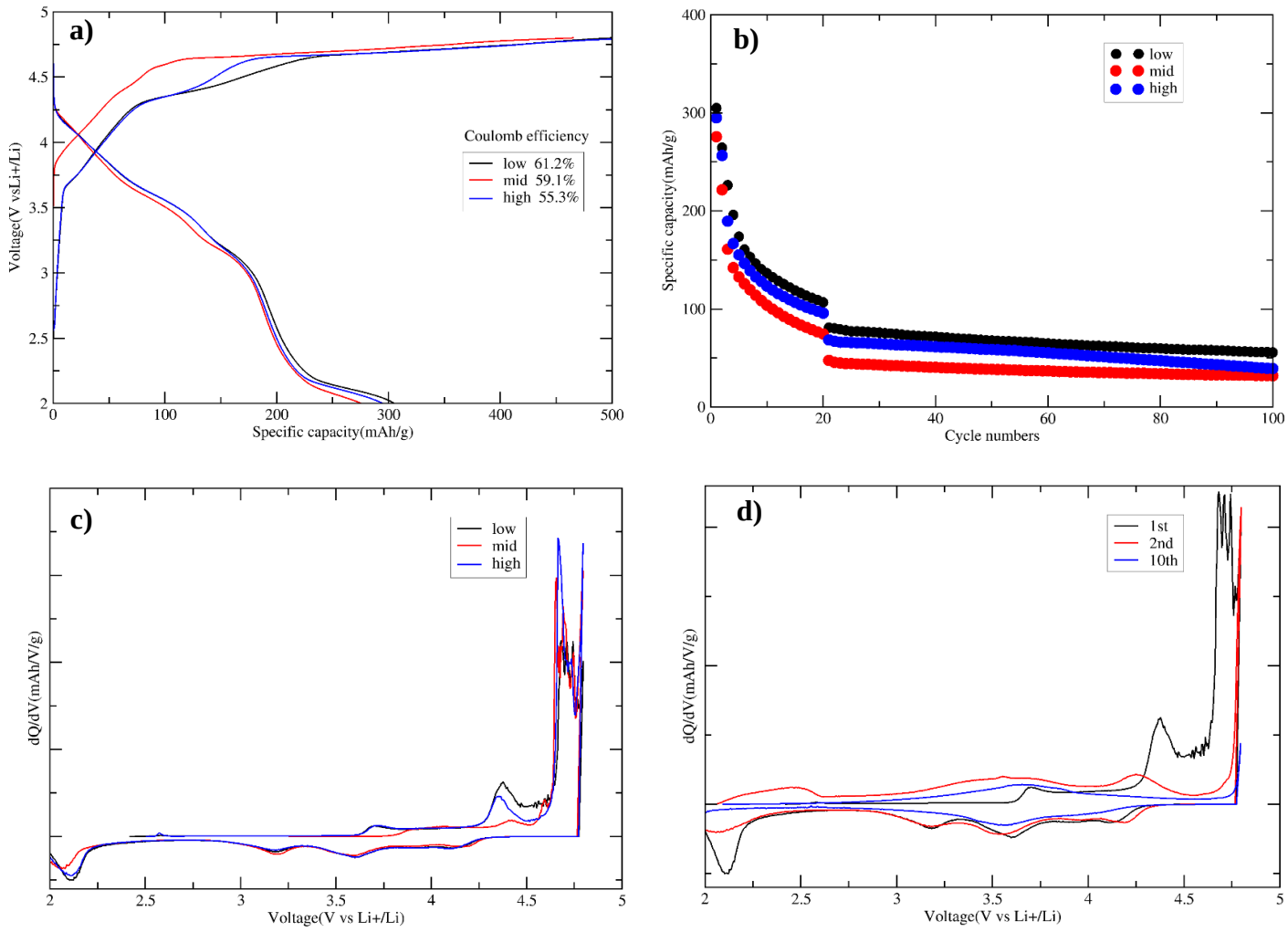

Fig3.6 The electrochemical performance of Li_2NiO_3, synthesis from three $Ni(OH)_2$ precursor made from three concentrations of NH_3; (a) Charge/discharge voltage profiles of Li_2NiO_3 electrodes; (b)cycling performance (first 20 cycles at the rate C/25 and then 20-100 cycles at C/5); (c) differential capacity versus (dQ/dV) for the Li_2NiO_3 electrodes; (d), 1, 2, 10 cycles of dQ/dV of low NH_3 Li_2NiO_3 -L electrodes.

The electrochemical behavior of Li_2NiO_3 cathodes is fundamentally governed by their crystal structure rather than transition metal chemistry, as demonstrated by Tabuchi et al.[35] These materials exhibit characteristic first-cycle capacities of ~500 mAh/g (charge) and ~300 mAh/g (discharge), yielding an initial efficiency of approximately 60%. This performance is notably inferior to Li_2MnO_3-

based solid solutions reported by Bianchini et al. [12], with the capacity difference attributed to irreversible structural changes during cycling. In situ characterization techniques including X-ray diffraction and electrochemical mass spectrometry reveal that oxygen loss during initial charging leads to reduction of transition metal oxidation states in subsequent cycles. [38] Armstrong's lattice dynamics model [37] explains this phenomenon through anion/cation rearrangement in the (1-x)MO_2 framework, where only partial lithium reinsertion (1-x) of the (1+x) extracted Li^+ occurs during discharge due to oxygen vacancy formation. The observed irreversible capacity loss (IRC) stems from the metastable phase transition between $R\bar{3}m$ and C2/m structures at relatively low calcination temperatures (550°C). All synthesized Li_2NiO_3 variants (derived from low, medium, and high-NH_3 precursors) consistently demonstrate this behavior, with approximately 50% of initially extracted lithium being reversibly reinserted. This limitation becomes particularly problematic for extended cycling or high-voltage operation, as Li^+ extraction from the $Ni_{2/3}Li_{1/3}$ layer proves increasingly difficult. [12]

Table3.2 Specific capacity data for the Li_2NiO_3 samples from commercial, low, mid, and high NH_3 $Ni(OH)_2$.

Sample	Q1c/(mAh/g)	Q1d/(mAh/g)	Q1d/Q1c	Q50c/(mAh/g)	Q50d/(mAh/g)	Q50d/Q50c	Q50d/Q1d
Li_2NiO_3-L	534	319	0.597	71	70	0.986	0.219
Li_2NiO_3-M	465	275	0.591	40	39	0.975	0.142
Li_2NiO_3-H	531	294	0.554	60	59	0.983	0.201

Based on the information provided in Figure 3.5 and Table 3.2, it can be observed that Li_2NiO_3-L exhibits the maximum specific capacity of around 60 mAh/g during the long cycle in the voltage window 2-4.8 V. This value is similar to the result obtained by Bianchini.[12] For the two inferior samples, Li_2NiO_3-H and Li_2NiO_3- M, the capacity decreases to just 35 mAh/g, which is nearly half that of Li_2NiO_3-L. Nevertheless, once the cycles exceed 30, the coulombic efficiency reaches a stable level of 98%. Compared to the isostructural phase, Li_2MnO_3, Park[22] shows the specific capacity is around 120 mAh/g for the Li_2MnO_3 synthesised at 600°C, higher than Li_2NiO_3 we obtained from 550°C. This indicates worse cycling performance for Li_2NiO_3 at low calcination temperature. Compared to the cathode $LiNiO_2$ with a high nickel concentration, Q50d/Q1d values of Li_2NiO_3 samples are only about 0.15–0.2, showing inadequate thermal stability and capacity retention.[39]

Electrochemical cycling performance within the 2.0-4.8 V voltage range (Fig. 3.5) reveals complete activation of all synthesized samples. Both low- and high-NH_3-derived materials demonstrate comparable capacity fading trends, with specific capacities declining to approximately 100 mAh/g by the 21st cycle following the rate change from C/25 to C/5. This degradation continues progressively, reaching ~60 mAh/g

at the 100th cycle - a value marginally lower than previously reported results for conventionally synthesized materials [12].

Notably, the solid-state synthesized reference material described by Bianchini et al. [12,36] exhibits distinct electrochemical behavior, characterized by an initial capacity increase during early cycles followed by gradual decay within the first 20 cycles. This anomalous activation process stems from two interrelated factors: (i) the inherent difficulty in oxidizing nickel ions during lithium extraction, and (ii) the requirement for elevated potentials to activate electrochemical reaction sites, a phenomenon analogous to that observed in Li_2MnO_3-based systems.[12,36] These combined effects result in the delayed electrochemical activation observed in conventional solid-state synthesized samples, contrasting with the immediate activation behavior of solution-processed materials described in this work.

Fig 3.7 shows the CV curves at 2-4.8 V for the Li_2NiO_3-L sample, the oxidation peak at 3.8 V corresponds to the oxidation reaction of Ni^{3+}/Ni^{4+}, the potential when lithium ions are extracted from the Li_2NiO_3 layer. The reduction reaction peak located around 3.6 V during discharge corresponds to the reaction of Li embedded in the layered NiO_2 component.[30,33] These phenomena indicate that the phase of Li_2NiO_3 samples transforms into a disordered phase during the initial charging process.[41] A major broad reduction peak at 3.4 V was observed during the initial discharge of the Li_2NiO_3 sample, which can be attributed to the lithiation of layered active NiO_2 into layered $LiNiO_2$.[42,43] It can be seen that the curve has no other peaks except near 2.0 and 4.8 V, indicating the electrochemical stability of the modified material in this voltage range.

Structural stability evaluation through cyclic voltammetry analysis reveals two key observations: first, the relative peak intensity attenuation between initial and subsequent cycles serves as a quantitative indicator of structural integrity. Diminished intensity reduction correlates with enhanced phase stability and suppressed oxygen evolution. Second, this oxygen retention mechanism significantly mitigates

irreversible side reactions, particularly during the critical first cycle where parasitic processes are most prevalent.

The observed voltage profile degradation originates from a crystallographic phase transformation from the initial layered configuration ($R\bar{3}m$ symmetry) to a defective spinel-type arrangement (Fd$\bar{3}$m symmetry). This structural evolution involves: cation migration into lithium layers, partial oxygen lattice collapse, and formation of tetrahedrally coordinated transition metal sites. These collective transformations account for both the voltage decay and capacity fade observed during extended cycling.

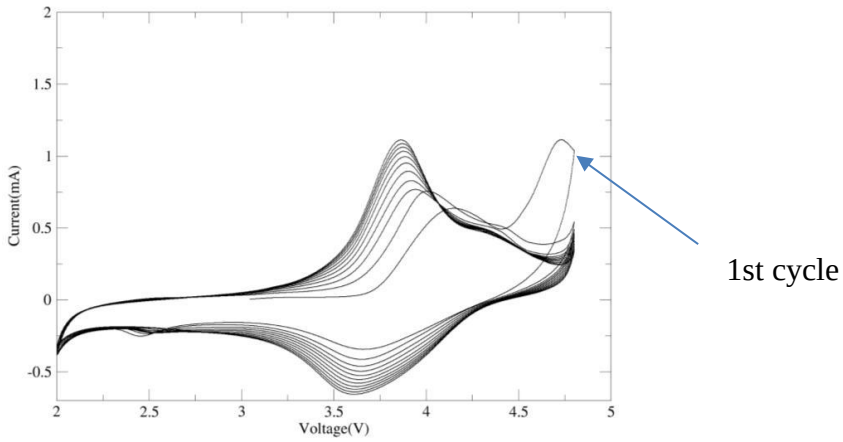

Fig3.7 CV curves of Li_2NiO_3-L sample.

3.4.5 Conclusion

Through systematic evaluation of the electrochemical behavior, crystallographic properties, and morphological characteristics, the Li_2NiO_3 material derived from low-NH_3 precursors emerges as the most promising candidate, demonstrating superior overall performance compared to its medium- and high-NH_3 counterparts. This superiority manifests in several critical aspects: enhanced cycling stability with improved capacity retention, better-defined crystalline structure evidenced by sharper diffraction peaks, and more homogeneous particle morphology with narrower size distribution. These comprehensive

findings establish the low-NH_3 synthesis route as the optimal approach, and consequently, all subsequent optimization efforts described in this study will employ $Ni(OH)_2$ precursors prepared under low-NH_3 conditions as the baseline material. This strategic selection not only ensures experimental consistency but also provides a reliable foundation for evaluating the effects of various modifications while maintaining direct comparability with the established performance benchmarks. The choice is further justified by the material's balanced electrochemical properties and structural integrity, which collectively address the key challenges in cathode material development for advanced battery applications.

3.5 Calcination optimization for Li excess (0, 3 and 5% LiOH excess)

3.5.1 Introduction and experiment design

The cation ordering in high-nickel cathode materials significantly influences their electrochemical behavior, with Ni/Li exchange playing a particularly crucial role. Previous studies have established that controlled lithium stoichiometry modulation can effectively regulate this cation mixing.[15] Building on this foundation, our investigation focuses on optimizing the anti-site defect chemistry in Li_2NiO_3 through systematic lithium excess variation during synthesis.

Experimental evidence suggests that moderate lithium excess induces several beneficial structural modifications: expansion of interlayer spacing facilitates lithium-ion diffusion, while simultaneously reducing Ni^{2+} incorporation in lithium layers. Furthermore, this approach promotes the development of a Ni^{3+} concentration gradient near particle surfaces, which enhances charge transfer kinetics. These coordinated effects collectively improve the Ni/Li exchange dynamics, as demonstrated by Guo et al.[15]

For this study, we employed a standardized synthesis protocol using low-NH_3 derived $Ni(OH)_2$ precursor with three lithium stoichiometries (0, 3 and 5% excess LiOH). All samples underwent identical thermal treatment:

- 12 h preheating at 300°C

- 24 h calcination at 550°C (3°C/min ramp rate)

This controlled approach enables precise evaluation of lithium stoichiometry effects while maintaining other synthesis variables constant, allowing for unambiguous interpretation of the lithium excess role in cation ordering optimization

3.5.2 SEM

According to Figure 3.8 (a), the secondary particle sizes of samples with 0 Li excess are approximately 5μm, which is smaller than the sizes of samples with 3% and 5% Li excess, which are around 10-20 μm. The primary particles have a dot-shaped morphology and have a similar size of 20 nm, which is consistent with the findings of Bianchini's work.[12]

The level of impurity present on the surfaces of the sample is observed to grow as the amount of excess Li increases, as shown in Figure 3.8. This observation is consistent with the XRD and Rietveld refinement results discussed in the following section.

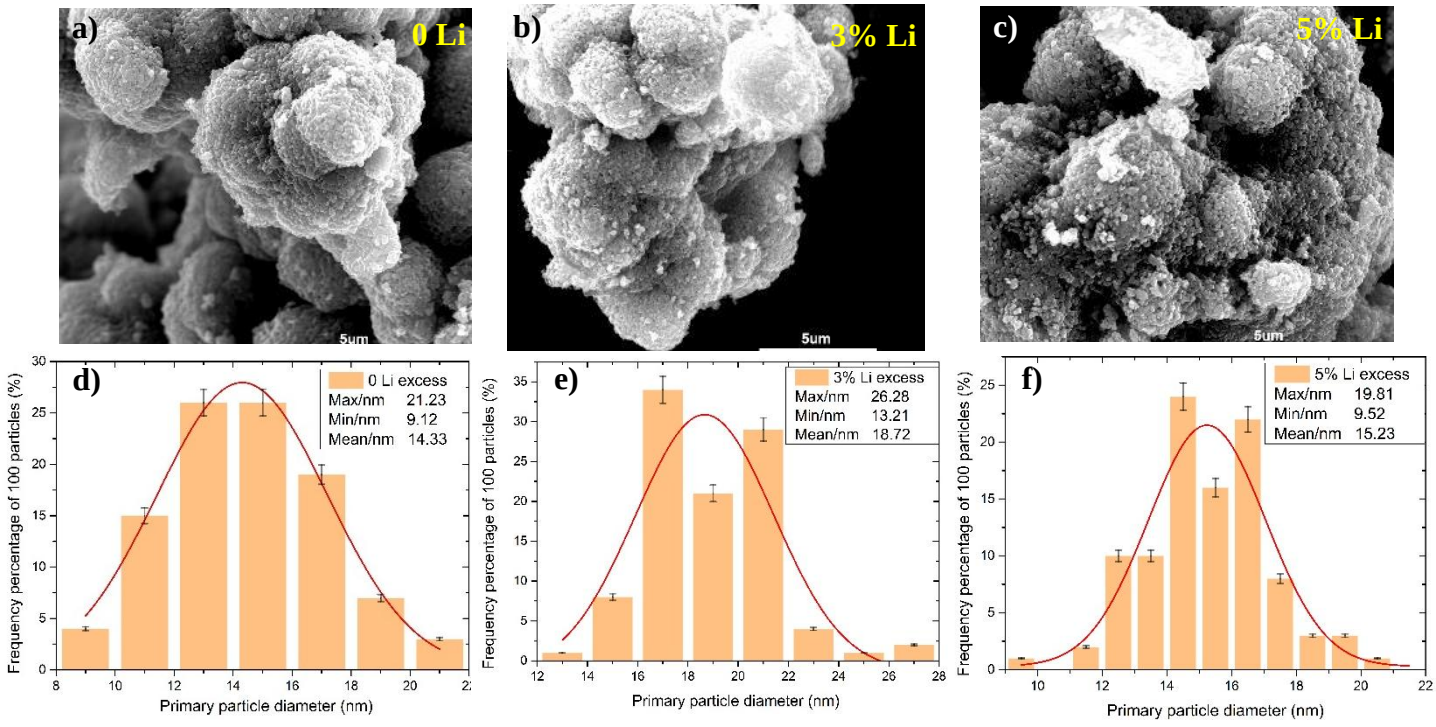

Fig3.8 SEM images (a,b, c) and particle size distribution (d, e, f) of all as-prepared samples.

3.5.3 X-ray diffraction and Rietveld analysis

The X-ray diffraction analysis confirms the successful synthesis of monoclinic Li_2NiO_3 (space group C2/m) across all prepared samples, as evidenced by the characteristic diffraction patterns shown in Fig. 3.9. Rietveld refinement of the diffraction data (Fig. S3.3) reveals distinct compositional differences among the samples with varying lithium stoichiometry. Notably, samples containing 0 and 3% lithium excess exhibit excellent phase purity, with no detectable impurity phases at the characteristic 2θ positions of 21.3°, 30.6°, and 31.8°. In contrast, the sample prepared with 5% excess lithium displays measurable secondary phase formation, suggesting an optimal lithium concentration threshold for phase-pure synthesis.

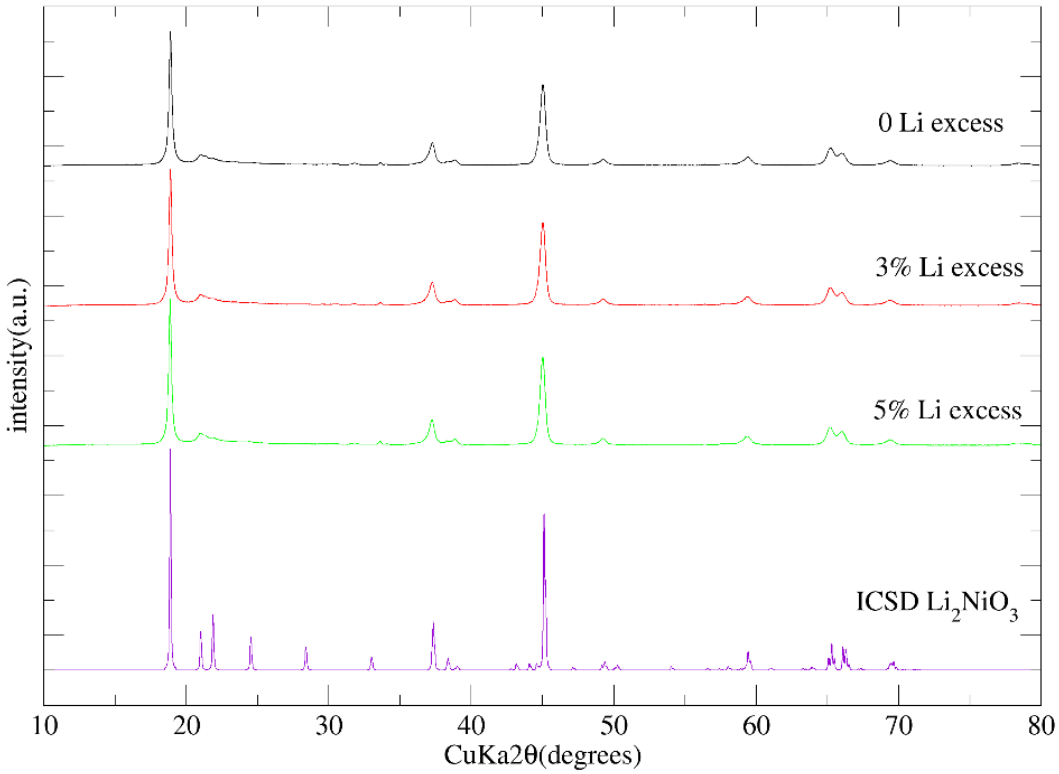

Fig 3.9 PXRD patterns of Li_2NiO_3 with different Li excess (0, 3, and 5%).

Crystallographic analysis demonstrates that the 3% Li-excess material shows reduced (110) peak intensity compared to other compositions, which can be attributed to increased structural disorder along the c-axis direction. Furthermore, the enhanced I(110)/I(020) intensity ratio observed in the 5% Li-excess sample indicates improved structural ordering, likely resulting from sufficient lithium availability preventing defect formation during low-temperature calcination.[22] This observation supports the

hypothesis that controlled lithium excess can effectively mitigate stacking fault generation under moderate thermal conditions.

Crystallographic analysis reveals significant lithium-dependent variations in nickel site occupancy (Table S3.3). The 4g site shows progressive Ni occupation increase (0 to 5% Li excess), while optimal 2b and 4h site ordering occurs at intermediate (3%) and high (5%) lithium concentrations, respectively. These findings suggest lithium stoichiometry plays a crucial role in cation distribution, with g_{total} values following similar trends. Although increased cation mixing may theoretically promote reaction kinetics, excessive nickel incorporation does not necessarily translate to enhanced electrochemical performance-a relationship that will be quantitatively examined in subsequent sections.

Rietveld refinement of the PXRD data (Fig. S3.3) confirms well-defined layered structures for all compositions, as evidenced by excellent fitting quality. Lattice parameter analysis reveals systematic structural evolution, with the 5% Li-excess sample showing both the smallest a/b ratio and most pronounced decreasing trend. This contraction indicates lithium-mediated structural optimization toward an ideal monoclinic configuration.[27] Interestingly, while crystallite size shows a nominal increasing trend with lithium content (Table S3.3), Scherrer analysis indicates statistically insignificant variations among the three samples (0-5% Li excess), suggesting lithium primarily affects cation ordering rather than grain growth under these synthesis conditions.

3.5.4 Electrochemical testing

All synthesized samples were prepared under identical thermal conditions: preheating at 300°C for 12 hours followed by calcination at 550°C for 24 hours (3°C/min heating/cooling rate), using low-NH_3 derived $Ni(OH)_2$ precursors. The resulting materials, designated as Li_2NiO_3-0, Li_2NiO_3-3, and Li_2NiO_3-5 (corresponding to 0, 3 and 5% lithium excess, respectively), were systematically characterized.

Electrochemical analysis reveals that these materials exhibit charge/discharge profiles remarkably similar to $LiMO_2$-Li_2MnO_3 solid solutions (where M = $Ni_{1/2}Mn_{1/2}$ or $Ni_{1/3}Mn_{1/3}Co_{1/3}$).[32,33] As shown in

Figure 3.10, the first-cycle voltage profile displays a characteristic sloping region followed by a distinct plateau at 4.5 V, consistent with the electrochemical behavior reported by Styanova et al. for analogous layered oxide systems.[34] This similarity suggests comparable lithium extraction/insertion mechanisms between these material classes, despite their differing compositions.

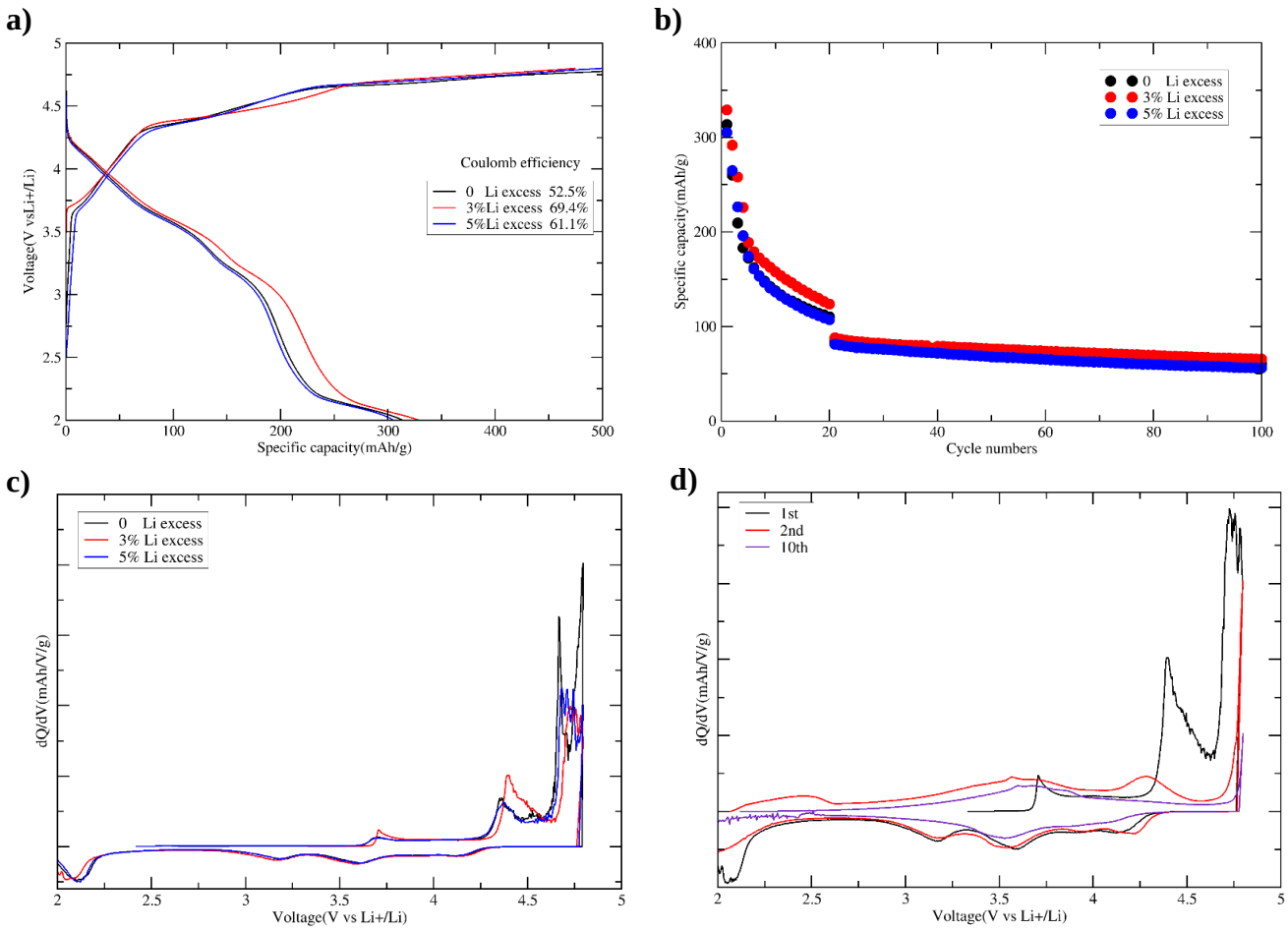

Fig3.10 The electrochemical performance of Li_2NiO_3, synthesis with three Li excess amounts;(a)charge/discharge voltage profiles of Li_2NiO_3 electrodes; (b) cycling performance (first 20 cycles at the rate C/25 and then 20-100 cycles at C/5); (c) differential capacity versus (dQ/dV) for the Li_2NiO_3 electrodes; (d) 1, 2, 10 cycles of dQ/dV for 3% Li excess Li_2NiO_3 electrodes.

The electrochemical profile of all the samples exhibited a sustained plateau at 4.75 V. The presence of this plateau can be ascribed to the initial charge cycle, which is marked by the release of oxygen. This observation is consistent with the results published by Bianchini[12] and Tabuchi.[34] It is worth noting that subsequent discharge cycles display a stark departure from the first charge, with the high-voltage plateau rapidly diminishing. This disparity indicates a fundamental change in the structure

of the host material when lithium is first extracted, resulting in a permanent decrease in capacity.[12] Tabuchi emphasizes that the predominant factor governing these initial electrochemical curves is not the transition metal element, but rather the crystal structure.[35]

Electrochemical performance analysis reveals significant differences among the synthesized materials (Table 3.3). The initial charge capacities measure 596 and 534 mAh/g for Li_2NiO_3-0 and Li_2NiO_3-5 respectively, while their discharge capacities drop substantially to 313 and 319 mAh/g, corresponding to Coulombic efficiencies of 52.5 and 59.7%, respectively. In contrast, Li_2NiO_3-3 demonstrates more balanced electrochemical behavior with 474 mAh/g charge capacity and 329 mAh/g discharge capacity, achieving a superior efficiency of 69.5%. This enhanced performance correlates with the elevated cation disorder (g_{total}) observed in structural characterization (Table S3.3), suggesting optimized Ni/Li mixing may improve reversibility.[40]

Long-term cycling stability remains a critical challenge, as evidenced by the capacity degradation after 100 cycles (Fig. 3.10). The final discharge capacities of 53, 65, and 60 mAh/g for Li_2NiO_3-0, -3, and -5, respectively correspond to a uniform capacity retention of only ~23%. These results underscore the persistent limitations in nickel-rich cathode materials, particularly regarding structural stability during extended cycling. The similar retention rates across all compositions indicate that while lithium stoichiometry affects initial performance, it does not fundamentally resolve the capacity fading mechanism inherent to these materials.

Table3.3 Specific capacity data for the Li_2NiO_3 samples with 0, 3%, 5% Li excess.

Sample	Q1c/(mAh/g)	Q1d/(mAh/g)	Q1d/Q1c	Q50c/(mAh/g)	Q50d/(mAh/g)	Q50d/Q50c	Q50d/Q1d
Li_2NiO-0	596	313	0.525	74	72	0.973	0.230
Li_2NiO-3	474	329	0.694	77	76	0.987	0.231
Li_2NiO-5	534	319	0.597	71	70	0.986	0.219

3.5.5 Conclusion

This case demonstrates that controlled lithium excess during the synthesis of Li_2NiO_3 significantly influences its structural and electrochemical properties. A moderate lithium surplus (3%) optimizes cation ordering by reducing Ni^{2+} occupation in lithium layers and promoting favorable Ni^{3+} surface gradients, resulting in improved charge transfer kinetics. Structural analyses confirm phase purity and refined crystallographic parameters, while electrochemical testing reveals enhanced initial Coulombic efficiency and balanced charge/discharge behavior for the 3% excess sample. However, despite initial performance improvements, all compositions exhibit substantial capacity fading over extended cycling, indicating that lithium stoichiometry adjustment alone is insufficient to overcome the intrinsic stability limitations of Li_2NiO_3 -based cathodes.

3.6 Calcination optimization for heat/cool rate (1, 3 and 5°C/min)

3.6.1 Introduction and experimental design

The thermal treatment protocol represents a critical parameter governing the synthesis of high-nickel lithium-rich oxides, where the heating/cooling rate significantly influences the final product's structural and electrochemical properties. Excessively rapid thermal ramping may compromise precursor conversion efficiency and promote impurity formation, while overly slow rates can induce detrimental lattice contraction effects. Previous studies have demonstrated that intermediate heating/cooling rates around 3°C/min facilitate optimal crystallinity development, as reflected by the enhanced resolution of XRD reflections characteristic of improved long-range structural ordering. [43] This thermal optimization achieves a delicate balance between crystallographic perfection and maintaining functional lithium diffusion pathways, while avoiding excessive volume contraction that would otherwise impede Li^+ mobility during electrochemical cycling. [44,45]

In this investigation, we employed a carefully designed two-stage thermal protocol to synthesize Li_2NiO_3 samples from low-NH_3 derived $Ni(OH)_2$ precursors with 3% lithium excess. The synthesis procedure involved an initial pre-treatment phase at 300°C for 12 hours followed by calcination at 550°C for 24 hours, with systematic variation of heating/cooling rates (1, 3, and 5°C/min) to produce the corresponding Li_2NiO_3-1dm, Li_2NiO_3-3dm, and Li_2NiO_3-5dm variants. This experimental approach enables comprehensive evaluation of thermal kinetic effects on this previously unexplored nickel-rich system, providing crucial insights into the structure-property relationships governing its electrochemical behavior. The selection of 3% lithium excess builds upon our previous findings regarding optimal cation ordering, while the rate variations probe the critical processing parameters specific to this materials system.

3.6.2 SEM

Analysis of the morphological characteristics reveals significant variations in particle size distribution dependent on thermal processing conditions. As evidenced by the SEM micrographs in Fig. 3.11(a-c), samples processed at 1 and 5°C/min heating/cooling rates exhibit secondary particle aggregates averaging 5μm in diameter, while the intermediate 3°C/min rate produces notably larger secondary particles (10-15 μm). Primary particle analysis demonstrates uniform nanoscale dimensions across all samples (15-20 nm), maintaining a distinct dot-like morphology that contrasts with the 100 nm particles reported in comparable systems.[12]

Notably, the Li_2NiO_3-5dm sample displays a pronounced size dependence on thermal history, with maximum particle dimensions reaching 33 nm at slower rates (1-3°C/min) compared to approximately 20 nm at elevated rates. This inverse correlation between heating/cooling rate and ultimate particle size suggests that kinetic factors during calcination significantly influence grain growth behavior. Furthermore, surface analysis indicates enhanced impurity accumulation in the 3°C/min processed sample, consistent with subsequent XRD and Rietveld refinement results discussed in later sections. These observations collectively demonstrate the critical role of thermal processing parameters in governing both morphological development and phase purity in nickel-rich cathode materials.

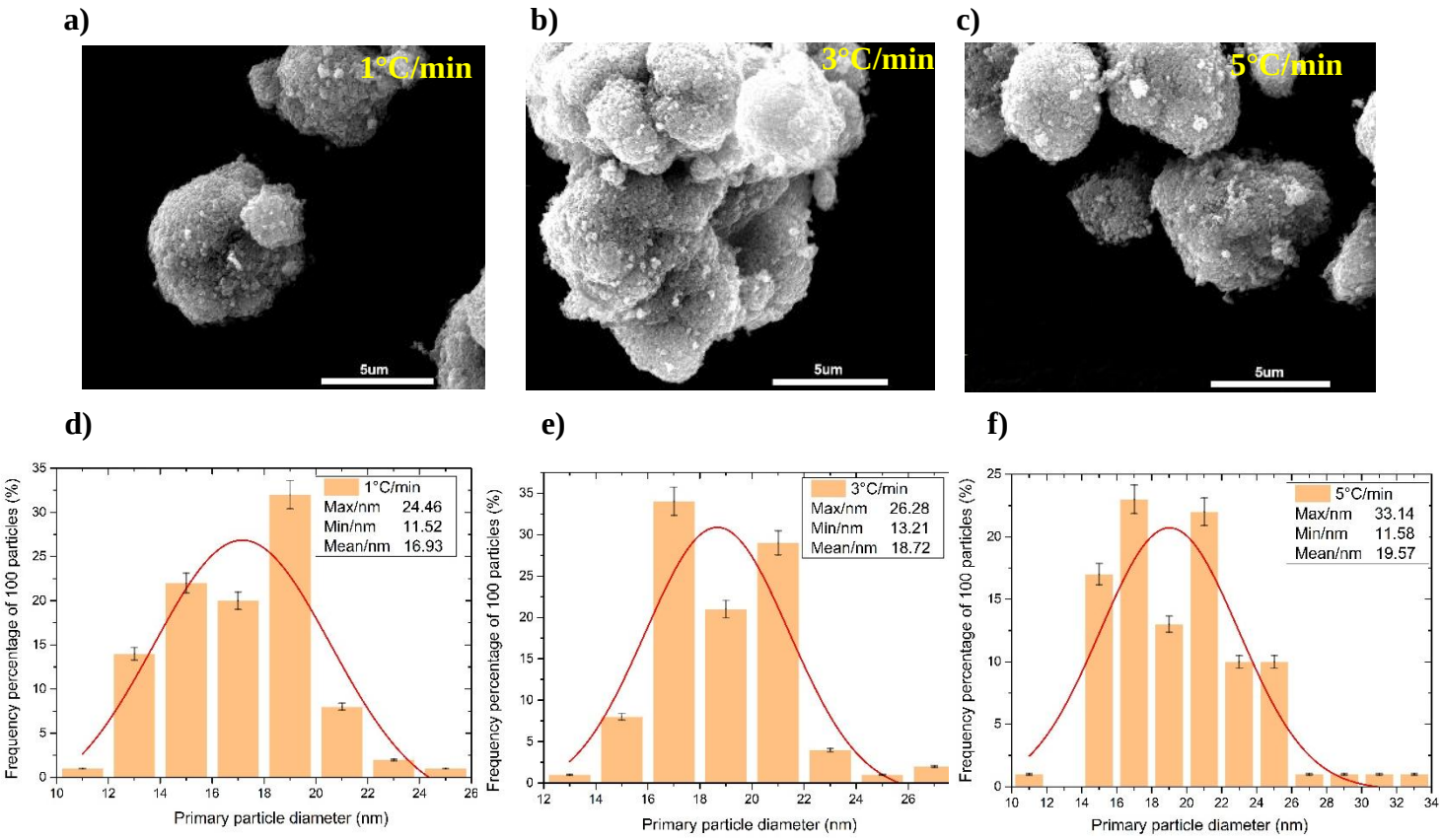

Fig3.11 SEM images (a,b, c) and particle size distribution (d, e, f) of all as-prepared samples.

3.6.3 X-ray diffraction and Rietveld analysis

The PXRD patterns of the Li_2NiO_3, subjected to different heating/cooling rates are displayed in Figure 3.12. These patterns indicate the presence of the C2/m monoclinic phase of Li_2NiO_3, which is of high quality.

Rietveld refinement of the PXRD patterns (Fig. S3.4) confirms excellent agreement between experimental and calculated profiles, validating the phase purity of the synthesized materials. A systematic investigation of impurity evolution reveals significant thermal-rate dependence, as evidenced by the characteristic peaks at 21.3°, 30.6°, and 31.8°. While the sample processed at 1°C/min shows no detectable impurity phases, progressive impurity accumulation becomes apparent in both the 3°C/min and 5°C/min samples, with the latter exhibiting the highest contamination level. This behavior suggests that slower heating rates facilitate more complete precursor conversion, while excessively rapid heating may compromise phase purity.

The structural analysis provides further insight into the thermal-rate effects on crystallographic perfection. The notably suppressed (110) peak intensity observed in the 1°C/min sample reflects substantial c-axis disorder, a characteristic consequence of prolonged intermediate-temperature exposure during slow thermal processing. Conversely, the sample prepared at 3°C/min demonstrates optimal structural ordering, as confirmed by its superior I(110)/I(020) intensity ratio relative to both slower and faster processed counterparts. These collective observations establish 3°C/min as the preferred heating rate for Li_2NiO_3 synthesis, achieving an ideal balance between phase purity and crystallographic integrity while minimizing stacking faults and structural defects.[28]

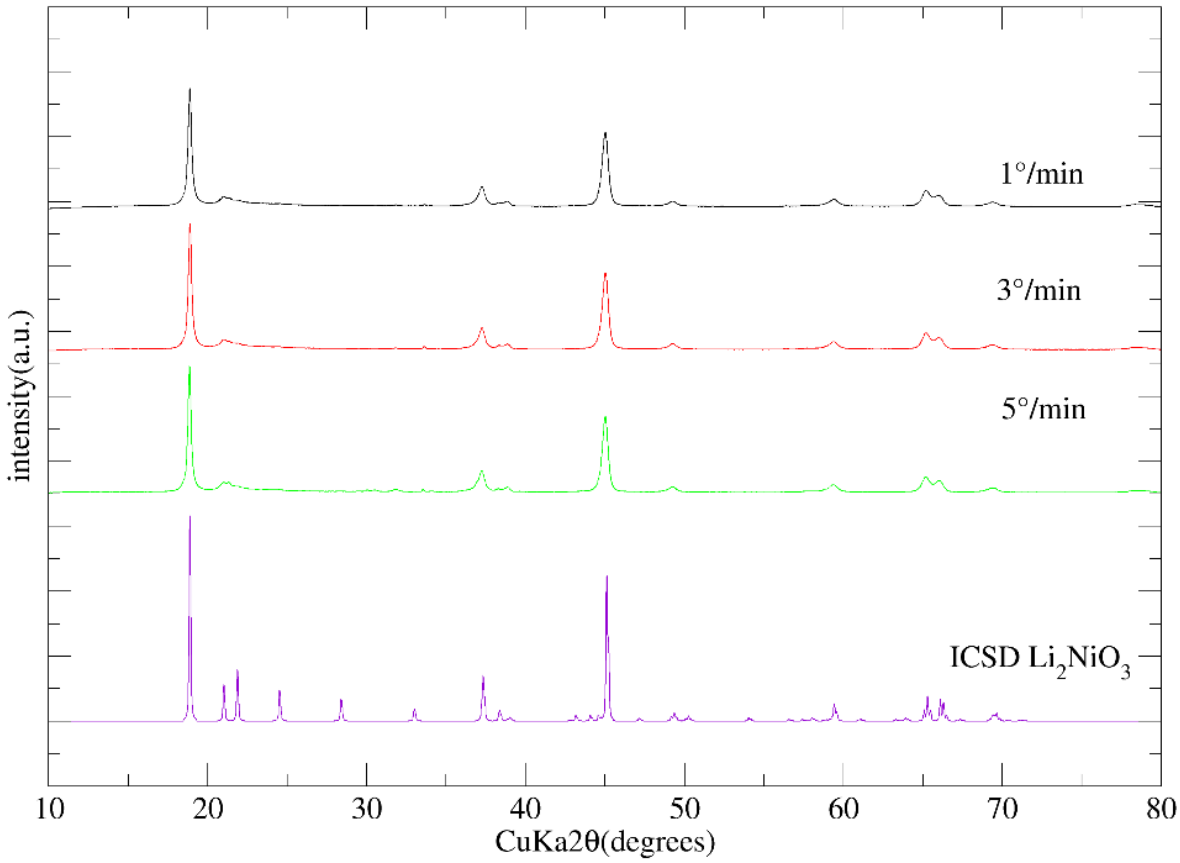

Fig3.12 PXRD patterns of Li_2NiO_3 with different calcination heat/cool rates (1, 3 and 5°C/min).

The crystallite size of the three samples is similar, with one sample slightly larger when heated at a rate of 3°C/min. This size matches the unit cell characteristics and structural information received from GSAS2, as shown in Table S3.4.

When comparing the a/b value of the three samples in Table S3.4, it is observed that the sample with a heating/cooling rate of 5°C/min has the smallest value. This indicates a decreasing trend in the a/b value, suggesting that an increase in the heat/cool rate of calcination leads to the formation of a better monoclinic structure for the element.[27]

According to Table S3.4 (b), the occupancy value of Ni increases on the site 4g, 2h as the heat/cool rate increases, approaching the standard value. The sample with a heating/cooling rate of 3°C/min has the lowest value of Ni occupancy on site 4h and gtotal, which is similar to the usual value. Nevertheless, it is crucial to examine the presence of impurities and defects.

3.6.4 Electrochemical testing

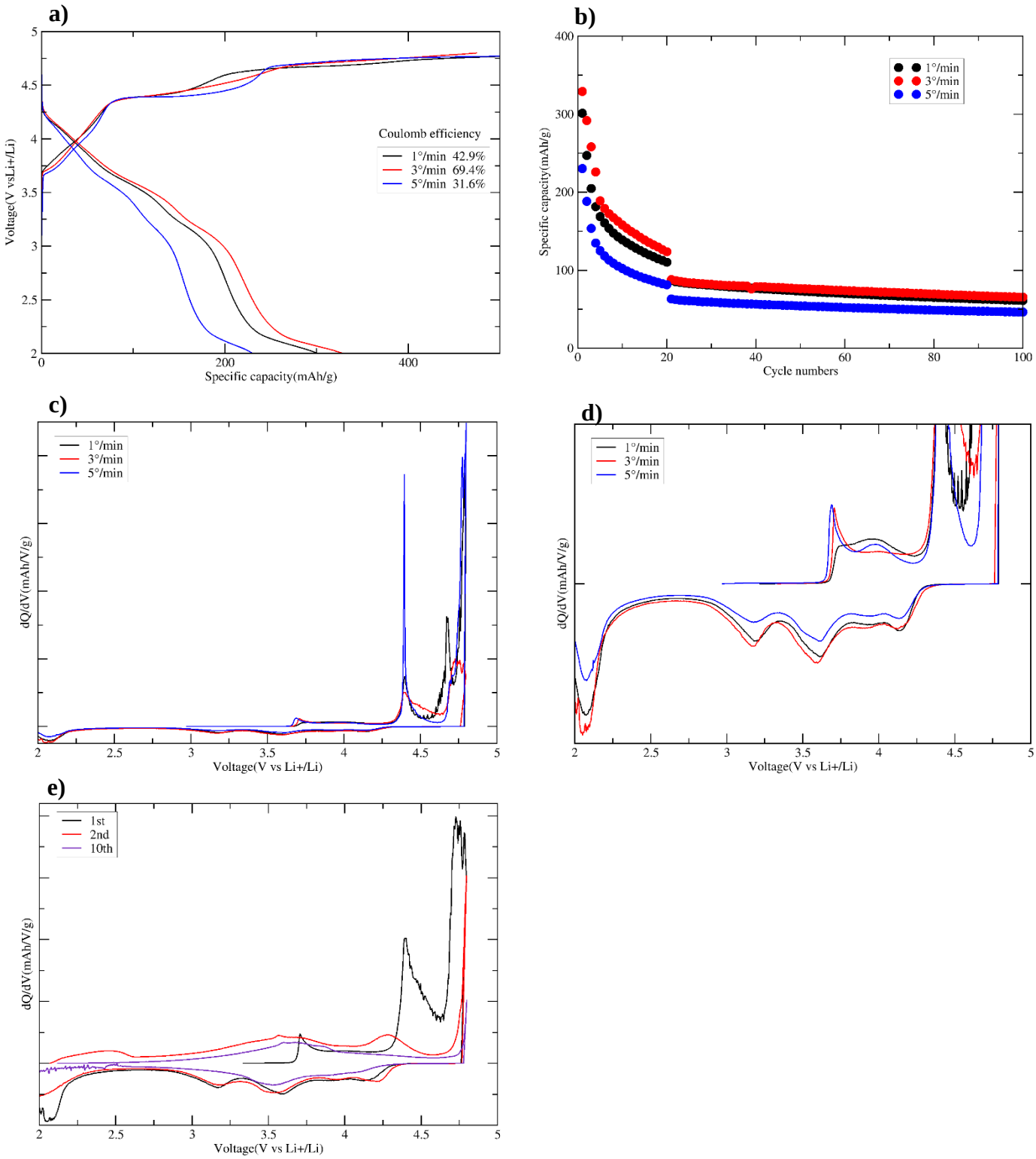

Fig3.13 The electrochemical performance of Li_2NiO_3, synthesis with three level of cool/heat rates (1, 3, 5 °C/min); (a)charge/discharge voltage profiles of Li_2NiO_3 electrodes; (b) cycling performance (first 20 cycles at the rate C/25 and then 20-100 cycles at C/5); (c), (d) differential

capacity versus (dQ/dV) for the Li_2NiO_3 electrodes; (e), 1, 2, 10 cycles of dQ/dV for cool/heat rate 3°C/min Li_2NiO_3 electrodes.

The previous analysis extensively covered the first charging and discharging characteristics. However, in the present scenario, both Li_2NiO_3-1dm and Li_2NiO_3-5dm exhibit significantly higher first charge capacity exceeding 700 mAh/g from Fig3.13. This can be attributed mostly to the chemical redox reaction, which will be the subject of future research. The Li_2NiO_3-5dm exhibits inferior electrochemical performance compared to the other two samples, particularly in terms of capacity retention. This is due to an incomplete reaction between lithium and nickel oxidation under rapid heating and cooling conditions.[33] The capacity retention for all the 3 samples are still low for around 0.24.

Table3.4 Specific capacity data for the Li_2NiO_3 samples with a heat/cool rate at 1, 3, and 5°C/min.

Sample	Q1c/(mAh/g)	Q1d/(mAh/g)	Q1d/Q1c	Q50c/(mAh/g)	Q50d/(mAh/g)	Q50d/Q50c	Q50d/Q1d
Li2NiO3-1dm	701	301	0.429	75	73	0.973	0.242
Li2NiO3-3dm	474	329	0.694	77	76	0.987	0.231
Li2NiO3-5dm	735	264	0.365	70	69	0.985	0.261

3.6.5 Conclusion

A comprehensive investigation of heating/cooling rates (1, 3, and 5°C/min) demonstrates significant variations in the structural and morphological characteristics of Li_2NiO_3 cathode materials. The 3°C/min thermal protocol emerges as the optimal condition, producing materials with superior crystallinity and minimal impurity phases, as confirmed by Rietveld refinement of PXRD patterns. This intermediate heating rate yields enhanced structural ordering, evidenced by an optimal I(110)/I(020) intensity ratio,

while simultaneously maintaining balanced particle growth with secondary particles of 10-15 μm and primary crystallites of 15-20 nm.

In contrast, the slowest heating rate (1°C/min) generates phase-pure materials but introduces substantial c-axis disorder due to prolonged intermediate-temperature exposure, resulting in defective layered structures and inhibited particle growth. Conversely, rapid heating at 5°C/min leads to increased impurity incorporation and compromised phase purity, likely due to incomplete precursor conversion during the shortened thermal treatment.

These findings establish that the 3°C/min heating rate represents the optimal balance between kinetic control and thermodynamic stability for Li_2NiO_3 synthesis, achieving simultaneous optimization of phase purity, crystallographic perfection, and particle morphology. The results align with fundamental principles of solid-state reaction kinetics and provide practical guidelines for processing high-performance nickel-rich cathode materials.

3.7 Calcination optimization for calcination temperatures (550-675°C)

3.7.Introduction and experimental design

Calcination temperature serves as a fundamental determinant of cathode material quality, exhibiting a pronounced influence on both structural integrity and electrochemical performance. Insufficient thermal treatment below optimal temperatures result in incomplete crystallization, yielding materials with defective structures and compromised electrochemical activity. Conversely, excessive calcination temperatures promote lithium volatilization and induce irreversible damage to the layered framework, ultimately degrading the material's performance through structural collapse and diminished phase transition reversibility. This delicate balance between insufficient and excessive thermal energy underscores the necessity for precise temperature control during materials synthesis. [40,46–49]

The current investigation employs a systematic approach to establish the optimal calcination window for Li_2NiO_3 cathode materials. Using carefully prepared low-NH_3 $Ni(OH)_2$ precursors with 3% lithium excess, the study examines a temperature range from 550 to 675°C at 25°C intervals. All samples undergo identical pre-treatment at 300°C for 12 hours followed by a controlled heating/cooling rate of 3°C/min during the 24-hour calcination process. This experimental design facilitates comprehensive evaluation of temperature-dependent structural evolution while maintaining consistent synthesis kinetics, thereby enabling accurate determination of the thermal stability window for high-performance Li_2NiO_3 cathodes.

The selected temperature range and experimental parameters were specifically designed to probe several critical aspects of materials behavior: the lower threshold for complete crystallization, the onset temperature for lithium loss, and the maximum temperature before structural degradation. By maintaining identical heating rates and precursor compositions across all samples, the study isolates temperature as the sole variable, ensuring unambiguous interpretation of calcination temperature effects on the final material properties.

3.7.2 SEM

The SEM images from different temperatures are shown in Fig3.14, the samples were identified as T-550, T- 575, T-600, T-625, T-650, T-660, and T-675. The primary particle size of the products increases as the calcination temperature rises. The particle sizes for T-550 and T-575 are approximately 20 nm, T-600 and T- 625 are around 30 nm, and T-650 and T-660 are around 35 nm (in comparison to Bianchini's study where the particle size was 100 nm.[12] The particle size for T-675 is approximately 60 nm. The significant rise is mostly attributed to the potential phase transition to $LiNiO_2$, as elaborated in the XRD section.

a)

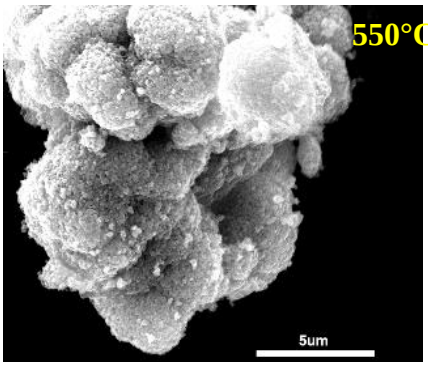

b)

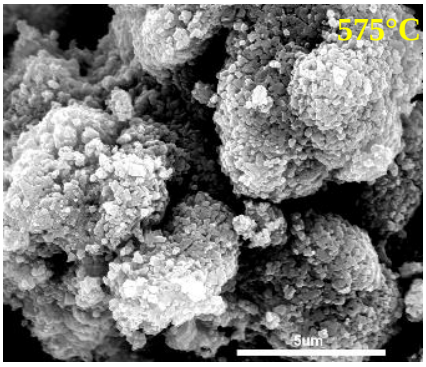

c)

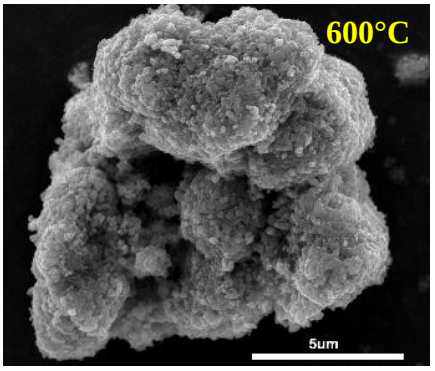

d)

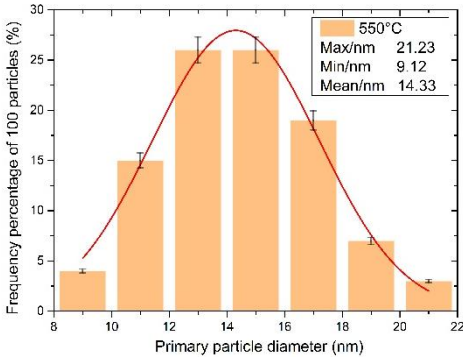

e)

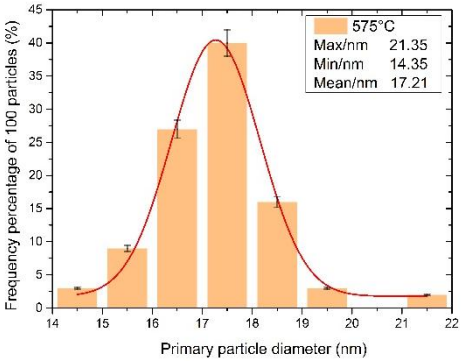

f)

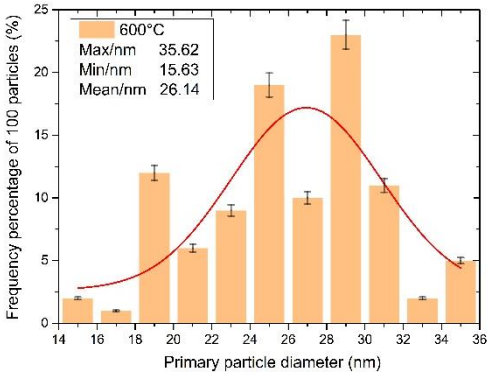

g)

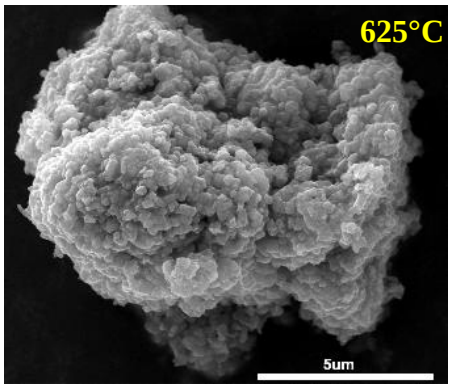

h)

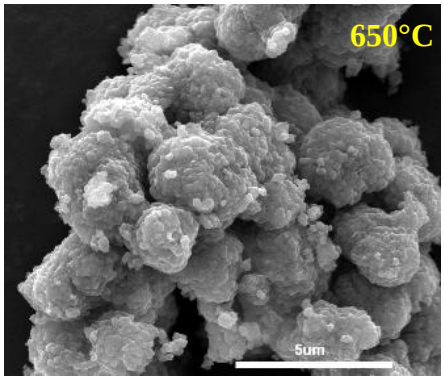

i)

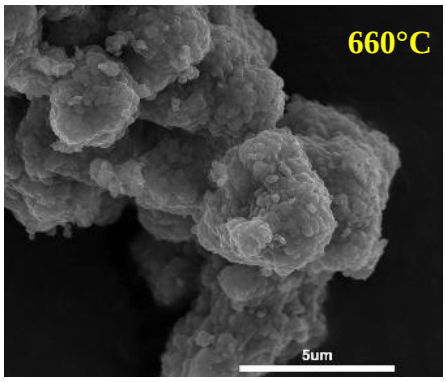

j)

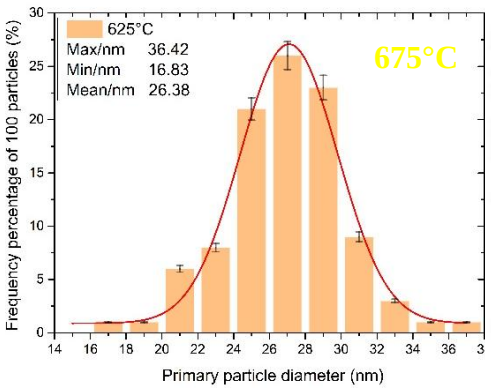

k)

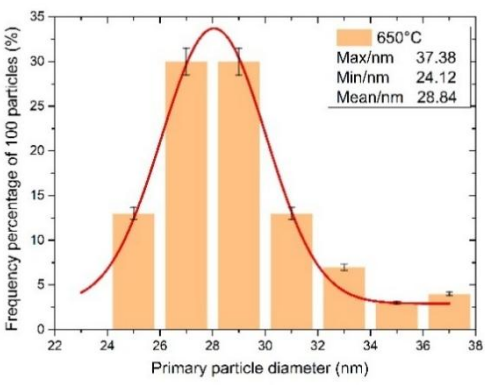

l)

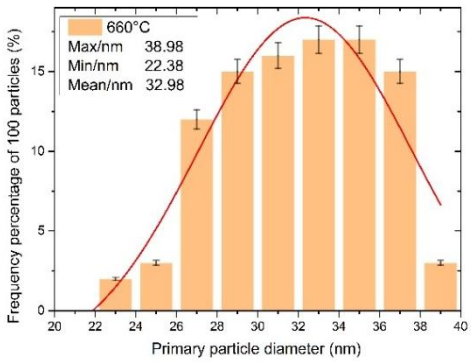

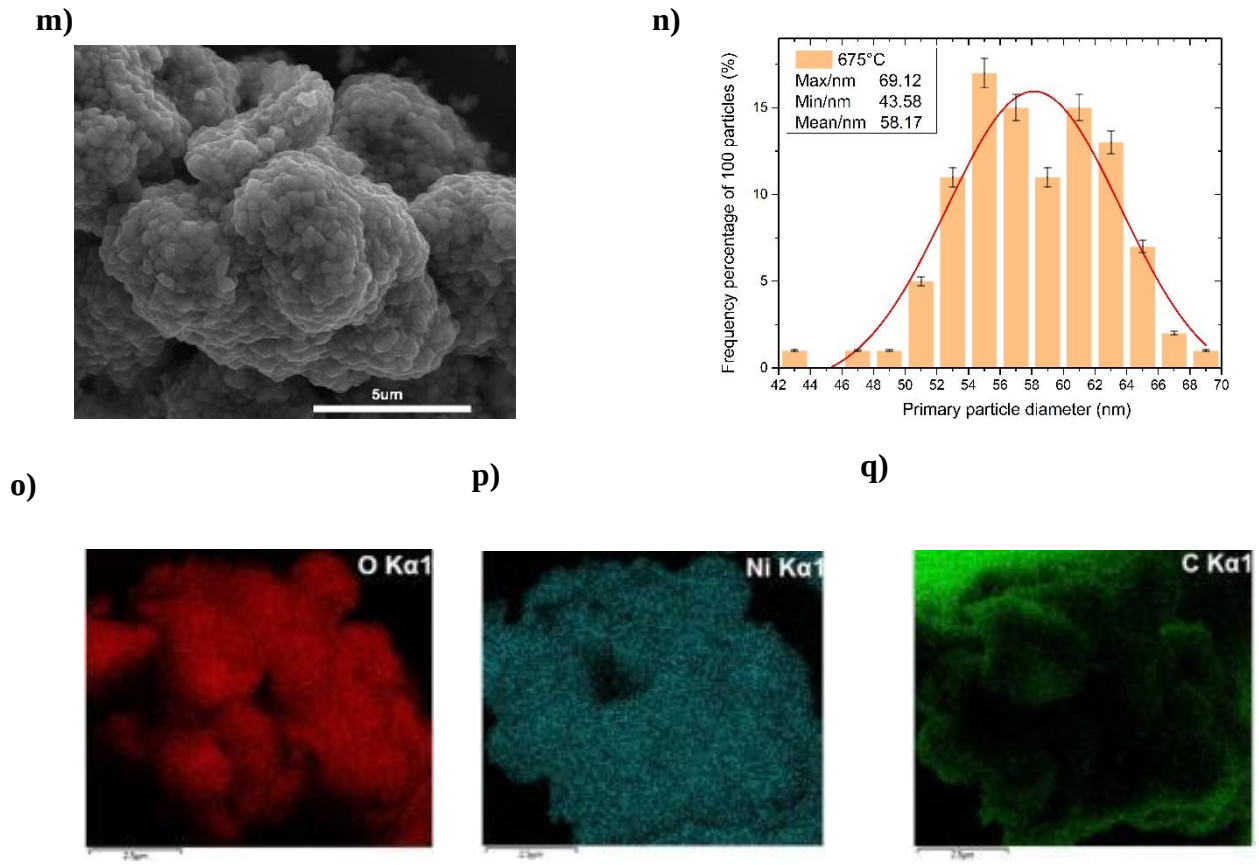

Fig3.14 SEM images (a, b, c,g, h, I, m) and particle size distribution (d, e, f, j, k, l, n) of all as-prepared samples, revealing growing primary particle sizes when increasing the calcination temperature; (o), (p), (q) represents O, Ni, C element distribution mapping for the surface of Li_2NiO_3 650°C. The crystallographic and morphological characteristics of Li_2NiO_3 exhibit significant dependence on calcination temperature, as revealed by comprehensive characterization. X-ray diffraction analysis demonstrates a progressive sharpening of the (001) plane peak at 18.7° with increasing temperature, where the full width at half maximum systematically decreases from 0.458 μm at 550°C to 0.207 μm at 675°C. This trend reflects enhanced crystallinity and grain growth under elevated thermal conditions, consistent with established solid-state reaction kinetics.[22]

Microstructural evolution follows a distinct temperature-dependent pathway, as evidenced by scanning electron microscopy. Lower temperature samples (550-600°C) display aggregated primary particles with irregular morphologies, while higher temperature processing (625-675°C) yields well-defined polyhedral crystals with smooth surfaces. This morphological transition correlates with the thermal decomposition of residual Li_2CO_3 impurities, which become increasingly volatile as the temperature approaches their melting point near 700°C. The development of faceted polyhedral structures at higher temperatures can be attributed to the preferential exposure of low-index crystal planes in lithium-rich materials, as described in previous studies.[50]

Elemental mapping confirms the presence of surface Li_2CO_3 through characteristic nickel-deficient regions exhibiting uniform oxygen and carbon distribution. These impurities likely form through post-synthesis atmospheric exposure, where lithium oxide reacts with ambient carbon dioxide during sample handling.[50] The temperature-dependent microstructural changes directly impact electrochemical performance parameters, creating a fundamental trade-off between the enhanced reaction kinetics afforded by high-surface-area low-temperature materials and the improved structural stability of high-crystallinity high-temperature samples. This critical structure-property relationship will be examined in detail through subsequent electrochemical characterization.[22]

3.7.3 X-ray diffraction and Rietveld analysis

X-ray diffraction analysis reveals significant temperature-dependent structural evolution in the synthesized Li_2NiO_3 materials (Figure 3.14a). Samples prepared between 550-625°C consistently adopt the characteristic monoclinic Li_2NiO_3 structure with C2/m space group symmetry, featuring alternating lithium and transition metal layers separated by oxygen planes. This layered arrangement shares structural similarities with the $R\bar{3}m$ rock-salt configuration, but distinguishes itself through unique cation ordering in

the transition metal layers, specifically through the formation of Ni_2Li mixed cation layers described by the $Li(Li_{1/3}Ni_{2/3})O_2$ structural notation.[22]

The diffraction patterns demonstrate progressive peak sharpening with increasing calcination temperature, reflecting enhanced crystallinity and reduced structural disorder. Two characteristic reflections at $2\theta = 65.2°$ and 65.8°, corresponding to the (−133) and (−331) crystallographic directions respectively, serve as sensitive indicators of monoclinic structure development. Materials synthesized at the lowest temperature (550°C) exhibit substantial structural disorder, manifested through pronounced peak broadening that suggests significant packing imperfections and limited long-range order. This disorder particularly affects key reflections in the 20-34° range, including the superlattice peak (20-30°) and specific (hkl) planes such as (020), (110), (-111), (021), and (111).[40]

The temperature-dependent structural evolution becomes particularly evident when comparing the well-defined (110) and (020) reflections, which serve as fingerprint peaks for Li_2MnO_3 and Li_2NiO_3 phases. While low-temperature synthesis yields materials with considerable structural instability and poor diffraction quality, processing at elevated temperatures (650-675°C) produces highly crystalline products with sharp, well-resolved peaks. This transition from disordered to ordered structures with increasing calcination temperature underscores the critical role of thermal energy in achieving optimal crystallographic perfection in nickel-rich layered oxide materials.

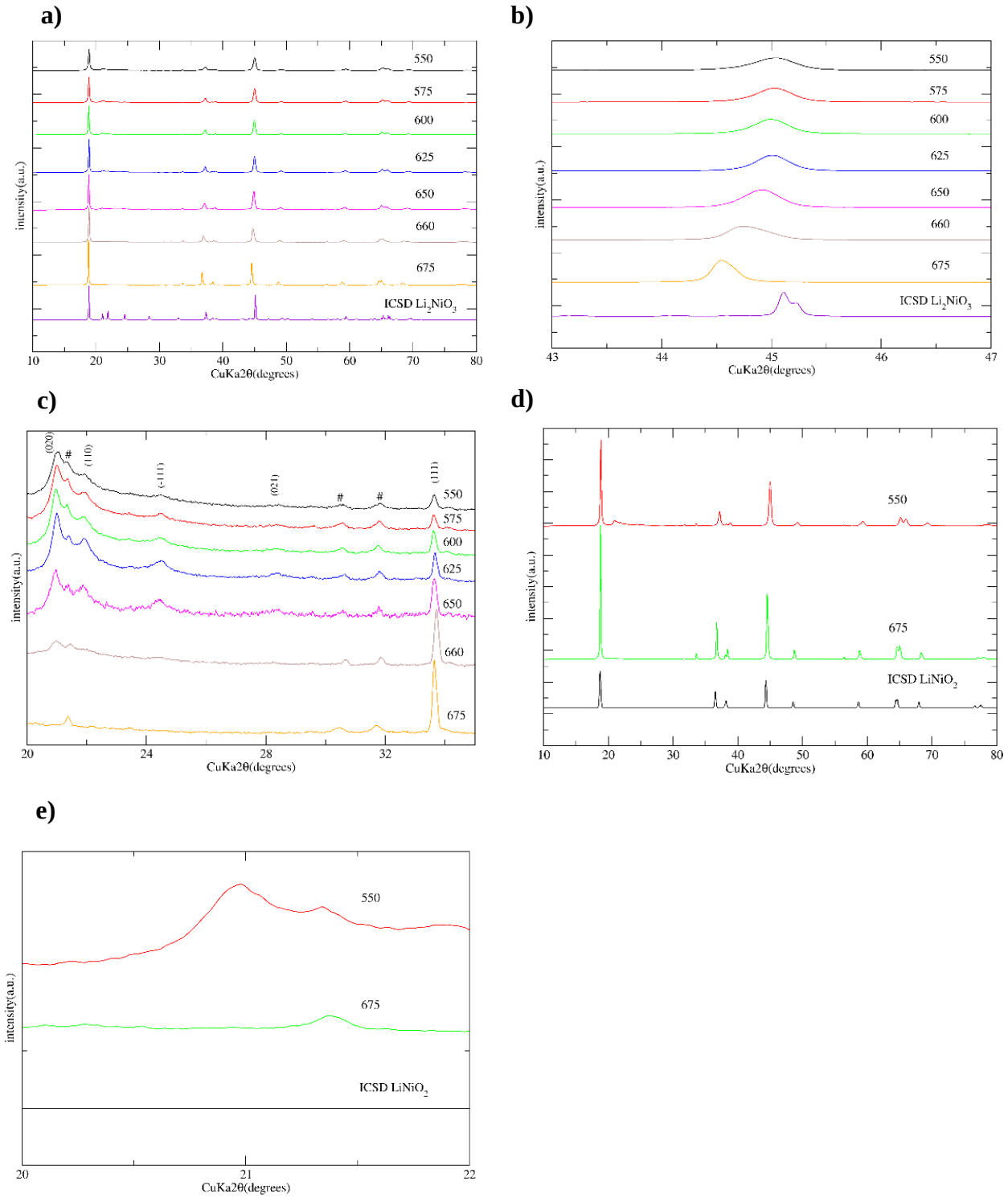

Figure 3.15 PXRD patterns of Li_2NiO_3 layered materials synthesized at calcination temperatures ranging from 550 to 675°C. The diffraction patterns reveal a gradual phase evolution, with a slight shift toward lower angles as the temperature increases.(a) The PXRD patterns (10–80°) are compared with reference ICSD 153094 data, demonstrating structural changes with temperature.(b) An expanded view (43–47°) highlights

peak position shifts, with the 675°C sample showing a tendency toward $LiNiO_2$ phase formation.(c) The expanded region (20–35°) further illustrates structural modifications induced by calcination temperature.(d) A direct comparison between the 550°C and 675°C samples and ICSD 78687 reference data emphasizes phase differences.(e) The magnified section (20–22°) provides additional insight into peak shifts and structural transitions.

The thermal treatment temperature significantly influences the structural characteristics of Li_2NiO_3, as evidenced by comprehensive X-ray diffraction analysis. (Fig3.15 a, b) Co-precipitated powders subjected to 550-575°C thermal treatment exhibit pronounced peak broadening, particularly affecting the (020), (110), (-111), and (021) reflections, which merge into asymmetric diffuse scattering features. This phenomenon suggests the presence of substantial structural disorder at lower calcination temperatures.[40]

Lattice parameter analysis reveals a systematic expansion along the a-axis with increasing temperature, progressing from 4.917(3) Å at 550°C to 4.938(1) Å at 650°C.[54] This thermal expansion correlates with the nickel oxidation state distribution, where the larger ionic radii of Ni^{3+} (0.70 Å) and Ni^{2+} (0.69 Å) compared to Ni^{4+} (0.62 Å) dominate at higher temperatures. The absence of Ni^{4+} in 650°C-synthesized materials potentially contributes to their diminished electrochemical performance, despite the theoretical expectation of tetravalent nickel in the Li_2NiO_3 structure.

Materials processed at 650-675°C demonstrate structural similarities to layered $LiNiO_2$, characterized by the disappearance of the characteristic 20-23° superlattice reflection while retaining minor peaks at approximately 33° and 56°. This observation suggests partial lithium-nickel disorder, where the loss of long-range stacking order along the c-direction occurs despite maintained in-plane cation arrangement. The superlattice peak[27] attenuation reflects this compromised three-dimensional ordering, with increased defect density at lower temperatures further contributing to peak broadening through the introduction of stacking faults perpendicular to the (001) plane.[56]

From a thermodynamic perspective, the elevated defect concentration in low-temperature samples creates a metastable high-energy state that facilitates lithium ion diffusion by reducing the activation barrier for cation migration. This structural characteristic manifests electrochemically through lowered lithium extraction potentials and enhanced reaction kinetics, as will be discussed in subsequent sections. The intrinsic relationship between calcination temperature, structural perfection, and electrochemical activity underscores the importance of optimized thermal processing in tailoring Li_2NiO_3 performance characteristics.[32, 57, 5]

X-ray diffraction analysis reveals consistent impurity characteristics across all synthesized samples, with distinct peaks observed in the 30-35° range (Fig. 3.15). Rietveld refinement confirms these features originate from Li_2CO_3 contamination, suggesting persistent carbonate formation during material preparation. The thermal treatment temperature significantly influences the diffraction patterns, as evidenced by systematic peak shifts toward lower angles with increasing calcination temperature from 550°C to 675°C (Fig. 3.15b). This angular displacement correlates with crystallite growth at elevated temperatures, consistent with established principles of thermal-induced particle coarsening in oxide materials.[11]

A critical structural transition occurs between 650-675°C, where Li_2NiO_3 undergoes transformation toward a $LiNiO_2$-type configuration. This phase evolution manifests through two key spectroscopic changes: the disappearance of the characteristic 20-23° superlattice reflection and measurable alterations in peak positions (Figs. 3.15 a, b). The vanishing superlattice signal particularly indicates disruption of the long-range cation ordering that defines the Li_2NiO_3 structure, while the modified peak locations reflect fundamental changes in unit cell dimensions accompanying the phase transition.

These structural modifications demonstrate the temperature-sensitive nature of nickel-based layered oxides, where relatively modest thermal variations can induce significant crystallographic reorganization. The persistence of Li_2CO_3 impurities across the entire temperature range suggests that carbonate contamination represents an intrinsic challenge in the synthesis of these materials, requiring specific

mitigation strategies beyond simple thermal treatment optimization. Rietveld refinement of PXRD data using the GSAS2 software package confirms the successful indexing of all samples to the monoclinic C2/m Li_2NiO_3 structure (ICSD No. 153094).[12] The refined unit cell parameters consistently exceed those of stoichiometric Li_2NiO_3 across the entire temperature range (550-675°C), suggesting the formation of a $LiNiO_2$-Li_2NiO_3 solid solution. This interpretation is further supported by the systematic increase in nickel content per formula unit with rising calcination temperature, as evidenced by the values exceeding the theoretical 0.67 stoichiometry in Table S3.5c.

The phase evolution exhibits distinct temperature dependence, with the 675°C sample showing complete transformation to $LiNiO_2$, characterized by the disappearance of characteristic (110) and (020) superlattice reflections. This structural transition accompanies significant changes in cation site occupancy, particularly for the 4g, 2b, g4g, and g2b positions between 625-660°C. The observed occupancy trends strongly indicate progressive nickel migration into lithium sites, facilitated by the similar ionic radii of Ni^{2+} (0.69 Å) and Li^+ (0.76 Å). This cation mixing suggests the stabilization of mixed Ni^{2+}/Ni^{3+} oxidation states rather than the expected Ni^{4+}, especially at elevated temperatures where higher oxidation states become thermodynamically unfavorable.[9]

Quantitative phase analysis reveals an increasing Li_2CO_3 impurity fraction with temperature, though all refinements demonstrate satisfactory agreement between experimental and calculated patterns. The residual discrepancies primarily originate from asymmetric peak broadening, particularly evident in the (020) and (110) reflections (Figure S3.5). Comparative analysis with reference data shows close correspondence in lattice parameters, with minor expansion observed in our samples potentially attributable to differences in cation disorder. The 550°C sample exhibits particularly pronounced Li/Ni mixing, as reflected in the distinct occupancy patterns at the 2b and 4h crystallographic sites.[2] The LNO675 sample was successfully refined against the $LiNiO_2$ reference structure (ICSD 78687)[3], yielding lattice parameters of a = 2.8744(3) Å and c = 14.1807(0) Å with a unit cell volume of 101.496(4) $Å^3$, demonstrating excellent

agreement with standard values. The corresponding diffraction pattern (Fig. 3.15d) confirms the complete transformation to a well-defined hexagonal phase at this elevated calcination temperature.

In the ideal Li_2NiO_3 structure, the ($Li_{1/3}Ni_{2/3}$) cation planes exhibit specific ordering along the monoclinic c-axis.[27] However, the existence of nearly degenerate stacking vectors (energy differences < 2 meV) leads to the formation of stacking faults. [55,58] These structural imperfections manifest most prominently in the 20-34° 2θ range, causing characteristic broadening of the (020), (110), (-111), (021), and (111) reflections.[27] The relative concentration of stacking faults can be semi-quantitatively assessed through the I(110)/I(020) intensity ratio, which decreases systematically from 0.84-0.89 with increasing annealing temperature, indicating improved structural ordering.[28]

Crystallite size analysis reveals a complex temperature dependence: initial growth from 550-625°C, stabilization at 650-660°C, followed by a dramatic increase to ~50 nm at the highest temperatures. This bimodal behavior reflects competing phenomena-the expected thermal-induced grain growth at lower temperatures and the phase transformation to $LiNiO_2$ above 650°C. While the Scherrer equation provides useful trends, its accuracy may be limited for these non-spherical particles, particularly given the anisotropic nature of the stacking fault effects on diffraction line broadening.[12,39]

3.7.4 Electrochemical testing

The electrochemical performance of these materials exhibits significant temperature-dependent variations, with the T-550 sample demonstrating superior initial cycle behavior, Fig 3.16. This sample achieves a notably higher coulombic efficiency compared to other compositions (250-300 $mAhg^{-1}$), delivering an initial charge capacity of approximately 320 $mAhg^{-1}$. All samples undergo characteristic electrochemical processes involving lithium extraction and nickel oxidation, where Ni^{2+} oxidizes to Ni^{3+}/Ni^{4+} between 2.5-4.4 V. A distinct oxygen release mechanism occurs between 4.4-4.6 V for most samples, except for T-675 which follows a different electrochemical pathway.

The voltage profiles reveal fundamental differences in charge storage mechanisms. Samples T-550 through T-650 display the characteristic voltage plateau signature of monoclinic Li_2MnO_3/Li_2NiO_3 materials, featuring both the nickel redox activity and oxygen release processes, Fig 3.16. In contrast, the T-675 sample exhibits electrochemical behavior more typical of $LiNiO_2$, with a continuous voltage increase during charge and abrupt capacity fade during discharge. This difference correlates with the structural transformation observed in XRD analysis.[60]

The oxygen release phenomenon represents a critical challenge for these materials, accounting for >100 $mAhg^{-1}$ irreversible capacity loss in the first cycle (Fig. 3.16b). This process initiates when the Fermi level enters the oxygen valence band at approximately 4.4 V, triggering surface oxygen loss and concomitant lithium extraction. The resulting oxygen vacancies facilitate transition metal migration from surface to bulk, progressively filling the octahedral sites vacated by lithium ions. This structural reorganization ultimately forms a layered MO_2 configuration with nickel and manganese occupying the transition metal sites.[41,42,51]

During discharge, the material undergoes complex phase transformations. The initial voltage decay from 4.4 V to 3.6 V corresponds to a layered-to-spinel structural transition. (Fig3.16 a) Subsequent lithium reinsertion between 3.6-3.3 V produces cation-disordered $LiNiO_2$, while below 3 V, lithium ions predominantly return to their original positions, relieving oxygen-oxygen repulsion forces. These multistep structural changes highlight the dynamic nature of these cathode materials during electrochemical cycling.[43,57]

The T-675 sample demonstrates superior cycling stability compared to other compositions, exhibiting only 10% capacity loss during cycles 10-20 and maintaining approximately 130 $mAhg^{-1}$ at the 60th cycle. This performance aligns closely with established data for $LiNiO_2$ systems[61], while other variants show significantly faster degradation, retaining only 75 mAh/g at the same cycle number. (Fig3.16 b) Long-

term cycling reveals similar trends, with the T-550 sample delivering 70 $mAhg^{-1}$ at the 100th cycle compared to 50-65 $mAhg^{-1}$ for intermediate temperature variants.

Structural characterization provides crucial insights into these performance differences. While both T-650 and T-675 samples lack the characteristic 20-23° superlattice reflection, Rietveld refinement distinguishes their phase composition - the former retains Li_2NiO_3 characteristics while the latter predominantly adopts the $LiNiO_2$ structure. This phase distinction is further supported by electrochemical behavior (Figs. 3.15a,b), where T-675 shows negligible oxygen release activity in the 4.4-4.6 V window, consistent with its hexagonal symmetry.[62]

Differential capacity analysis reveals distinct redox processes among the samples. The T-550-600 variants exhibit a single oxidation peak at 3.7 V during initial charging, while T-625-675 samples display two oxidation features (4.6 and 4.7 V) corresponding to Li_2O extraction and proton exchange processes.(Fig3.16 c, d) The main reduction peak at 3.6 V for T-550-650 samples signifies lithiation of MnO_2 to $LiMnO_2$, with subsequent nickel reduction shifting from 3.7 V to 3.5 V, indicative of spinel phase formation. Notably, higher temperature samples show attenuated transformation kinetics, as evidenced by reduced peak intensities at 3.6 V.[61-65]

The T-675 sample exhibits unique electrochemical signatures (Fig3.16 g) consistent with $LiNiO_2$ phase transitions. During charging, sequential structural transformations occur from hexagonal (H1) to monoclinic (M) at 3.6 V, followed by M→H2 at 4.1 V and H2→H3 at 4.3 V, with reverse transitions during discharge. These observations, combined with XRD data, confirm the complete structural conversion to $LiNiO_2$ at the highest calcination temperature.[61,66]

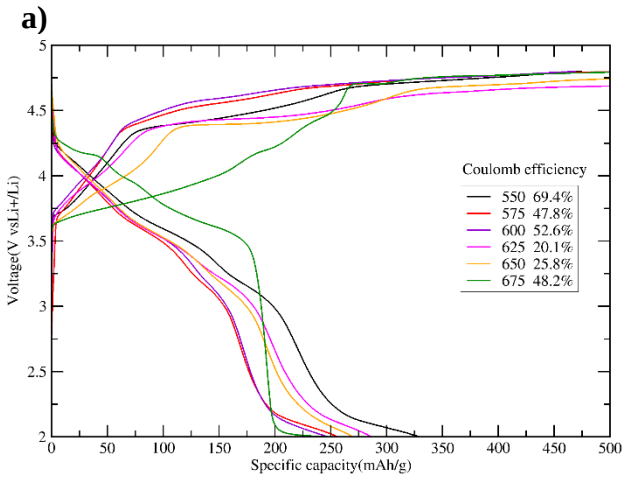
a)
Voltage(V vsLi+/Li)
Specific capacity(mAh/g)
Coulomb efficiency
550 69.4%
575 47.8%
600 52.6%
625 20.1%
650 25.8%
675 48.2%

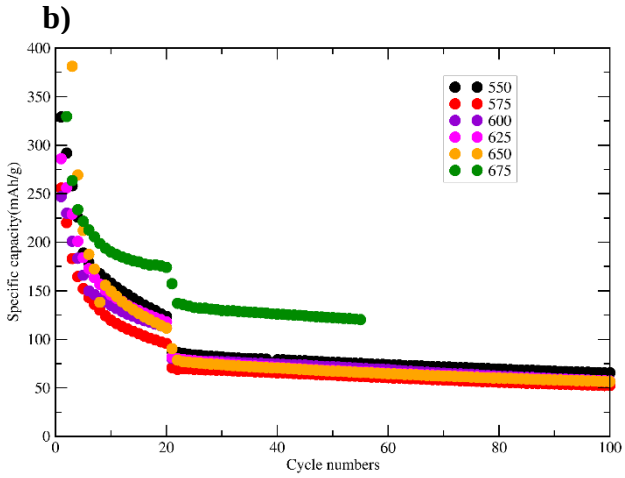
b)
Specific capacity(mAh/g)
Cycle numbers
550
575
600
625
650
675

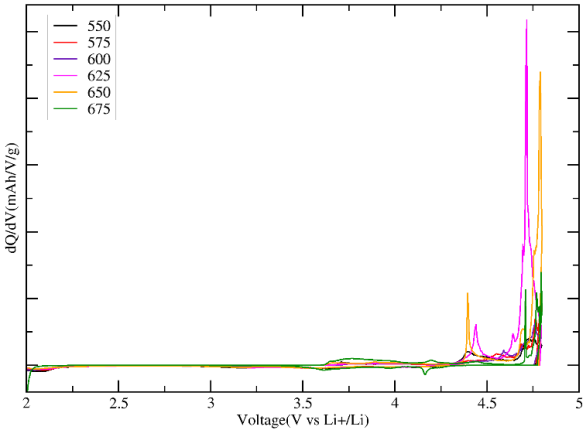
c)
dQ/dV(mAh/V/g)
Voltage(V vs Li+/Li)
550
575
600
625
650
675

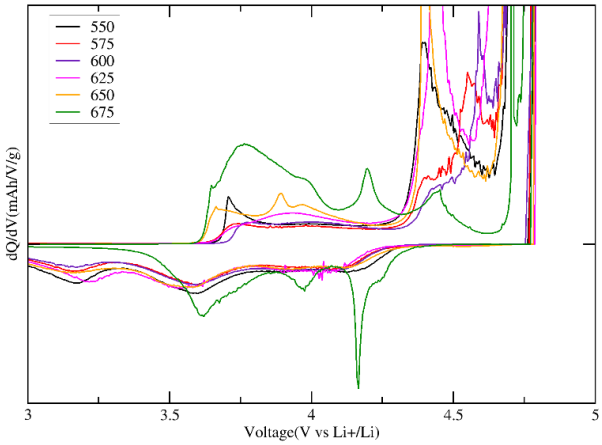
d)
dQ/dV(mAh/V/g)
Voltage(V vs Li+/Li)
550
575
600
625
650
675

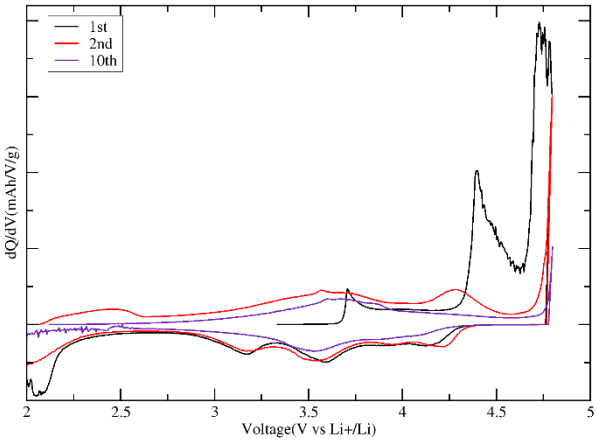
e)
dQ/dV(mAh/V/g)
Voltage(V vs Li+/Li)
1st
2nd
10th

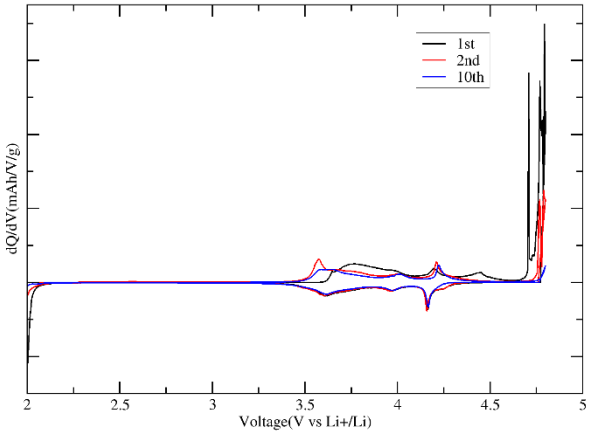
f)
dQ/dV(mAh/V/g)
Voltage(V vs Li+/Li)
1st
2nd
10th

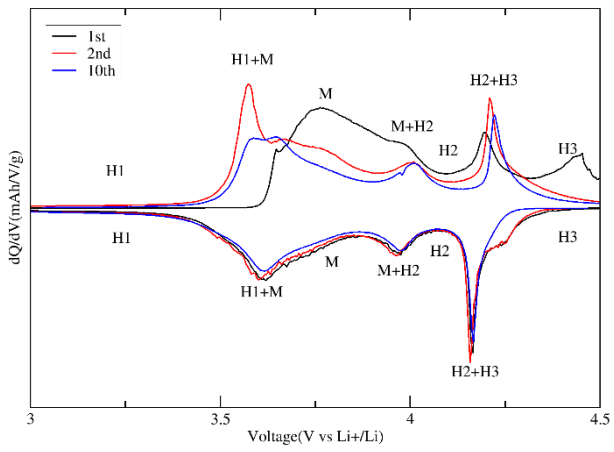
g)
dQ/dV(mAh/V/g)
Voltage(V vs Li+/Li)
1st
2nd
10th
H1+M
M
M+H2
H2
H2+H3
H3
H1
H1
M
M+H2
H2
H3
H1+M
H2+H3

Fig3.16 The electrochemical performance of different calcination temperature levels of Li_2NiO_3-$LiNiO_2$ series samples; (a)charge/discharge voltage profiles of Li_2NiO_3-$LiNiO_2$ electrodes; (b) cycling performance(first 20 cycles at the rate C/25 and then 20-100 cycles at C/5; (c), (d) differential capacity versus (dQ/dV) for the Li_2NiO_3-$LiNiO_2$ electrodes; (e), (f) 1, 2, 10 cycles of dQ/dV curves of Li_2NiO_3-550 electrodes; (g) 1, 2, 10 cycles of dQ/dV curves of $LiNiO_2$-675 electrodes with process of phase transformation.

3.7.5 Conclusion

The calcination temperature profoundly influences both the structural characteristics and electrochemical behavior of Li_2NiO_3 cathode materials. As the processing temperature increases from 550°C to 675°C, a gradual structural evolution occurs from monoclinic Li_2NiO_3 to hexagonal $LiNiO_2$, accompanied by significant changes in electrochemical performance.

Materials synthesized at lower temperatures (550-625°C) maintain the characteristic monoclinic Li_2NiO_3 structure but exhibit substantial capacity fade during cycling, primarily due to oxygen release mechanisms between 4.4-4.6V. These samples demonstrate higher initial capacities but suffer from rapid degradation, with the layered-to-spinel phase transition during discharge contributing to structural instability.

In contrast, samples processed at 650-675°C undergo complete transformation to the $LiNiO_2$ structure, exhibiting fundamentally different electrochemical behavior. The high-temperature variants show superior cycling stability with 90% capacity retention after 20 cycles, albeit with lower initial capacities. Their continuous voltage profiles and characteristic phase transitions during cycling confirm the structural conversion to hexagonal symmetry.

The temperature-dependent performance characteristics reveal an inherent trade-off between capacity and stability. While lower temperatures promote higher initial activity through defect-mediated kinetics, higher temperatures yield more stable structures at the expense of reduced capacity.

Intermediate temperatures around 625°C appear to offer a balance between these competing factors, though oxygen release remains a fundamental limitation for the Li_2NiO_3 system.

These findings provide critical insights for optimizing nickel-rich cathode materials, demonstrating how calcination temperature can be precisely controlled to tailor both structural characteristics and electrochemical performance for specific battery applications.

3.8 Conclusion (Optimization of Li_2NiO_3 Synthesis and Phase Stability)

This chapter systematically investigated the critical parameters governing the synthesis and performance of Li_2NiO_3 cathode materials. Comprehensive characterization revealed that optimal material properties are achieved through a two-stage thermal treatment process consisting of 12-hour preheating at 300°C followed by 24-hour calcination at 550°C, using a controlled heating/cooling rate of 3°C /min under oxygen atmosphere. These conditions, combined with 3% lithium excess and low NH_3 concentration precursors, yield phase-pure Li_2NiO_3 with enhanced electrochemical performance.

The study demonstrated the crucial role of preheating in facilitating proper precursor decomposition and subsequent crystallization. Through combined XRD analysis, Rietveld refinement, and SEM characterization, we established that this thermal protocol promotes optimal cation ordering while minimizing impurity formation. Electrochemical evaluation confirmed these structural advantages translate to superior performance metrics.

A significant finding concerns the thermal stability limit of the Li_2NiO_3 phase. Under high-temperature conditions (675°C), even in oxygen-rich environments, the material undergoes irreversible transformation to $LiNiO_2$. This phase transition, thoroughly characterized through multiple techniques, reveals the thermodynamic instability of Ni^{4+} in this system, with reduction to Ni^{2+}/Ni^{3+} states being energetically favorable.

For the monoclinic Li_2NiO_3 phase, the research identified several promising directions for further optimization at lower calcination temperatures. Surface modification approaches such as coating and bulk engineering strategies including selective doping represent potential avenues to enhance both structural stability and electrochemical performance while maintaining the advantageous characteristics of the Li_2NiO_3 framework.

These findings provide a comprehensive foundation for developing high-performance nickel-rich cathode materials, establishing clear structure-property relationships and identifying key parameters for controlled materials synthesis. The insights gained from this systematic investigation offer valuable guidance for future optimization of layered oxide cathode materials.

Supporting information:

a) short calcination

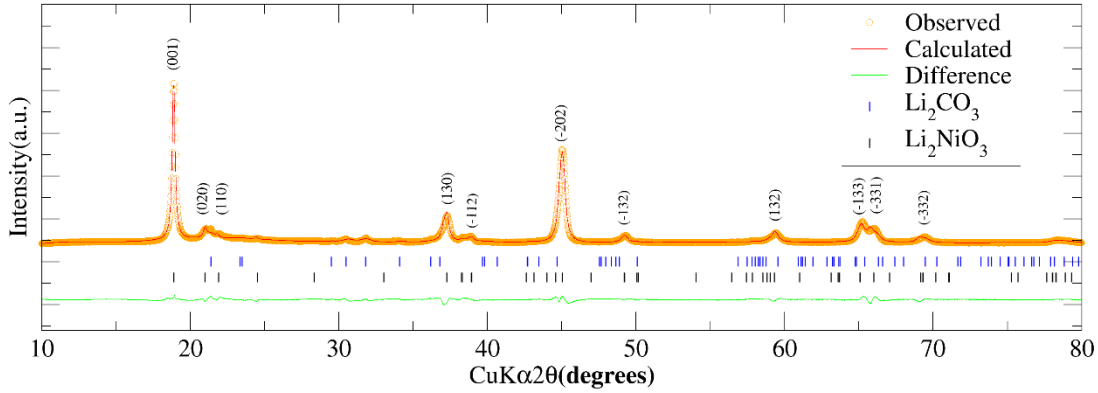

b) no preheat

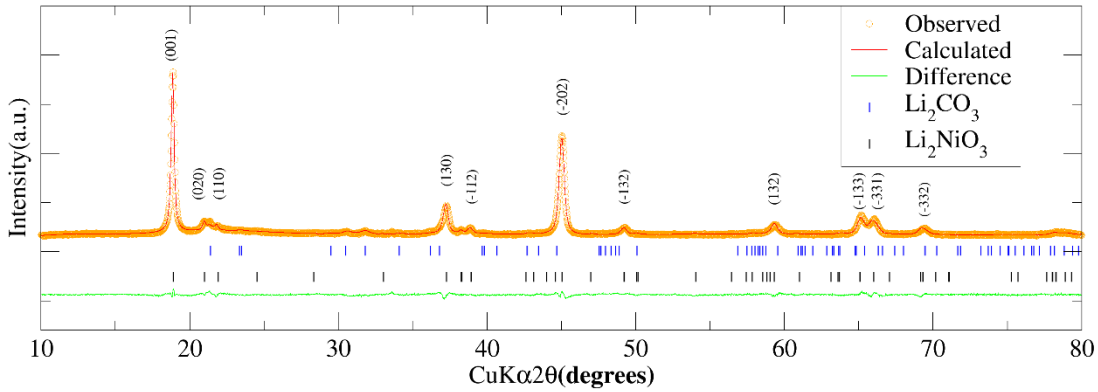

c) Preheat and calcination

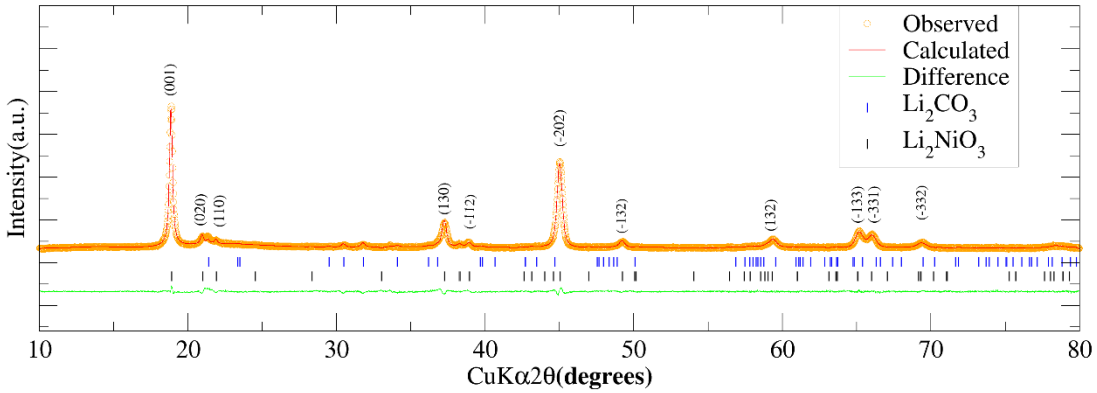

Fig S3.1 Rietveld refinements of lab PXRD data of Li_2NiO_3 synthesized in conditions of a) short calcination time, b) no preheat, c) preheat and calcination.

Table S3.1 Calculated structural parameters for the monoclinic layered rock-salt Li_2NiO_3 (C2/m) from X-ray Rietveld analysis for samples with: a short calcination time, no preheat, and preheat and calcination.

a) Lattice parameters and crystallite sizes from Scherrer equation for the Li_2NiO_3

Sample	short calcination	no preheat	Li_2NiO_3 preheat and calcination
a(Å)	4.927(1)	4.926(6)	4.925(6)
b(Å)	8.465(3)	8.465(4)	8.465(5)
c(Å)	4.98(1)	4.98(1)	4.97(9)
β (°)	109.25(2)	109.23(9)	109.23(2)
V($Å^3$)	196.11(4)	196.08(9)	196.0(5)
R_{wp}	0.03042	0.02995	0.03305
X^2	2.5	2.38	2.662
Crystallite Size (nm)	18.66±1.36	20.39±1.44	20.95±1.74

b) Transition metal (Ni) occupancy(g) at each site and Li_2NiO_3 calculated Ni per chemical formula

Sample	low NH_3 Li_2NiO_3	mid NH_3 Li_2NiO_3	high NH_3 Li_2NiO_3	Li_2NiO_3 standard
g_{4g}	0.751(4)	0.753(4)	0.754(1)	0.78(2)
g_{2b}	0.561(9)	0.567(4)	0.557(4)	0.41(2)
g_{2c}	0	0	0	0
g_{4h}	0.052(0)	0.059(7)	0.028(2)	0.02(2)
g_{total}[a]	0.722(9)	0.731(2)	0.707(3)	0.67(3)

g_{total}[a] means transition metal (Ni) content per chemical formula, calculated from equation

$g_{total}=(2g_{4g}+g_{2b})/3+(g_{2c}+2g_{4h})/3$.[35]

a) low NH_3

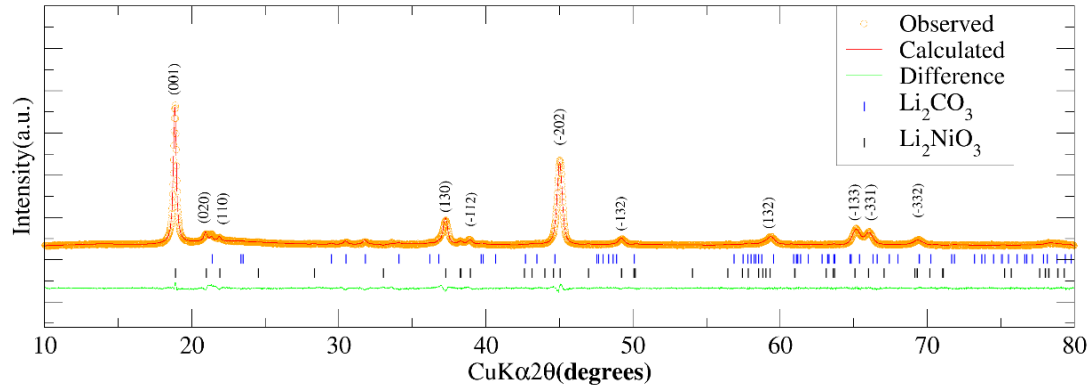

b) mid NH_3

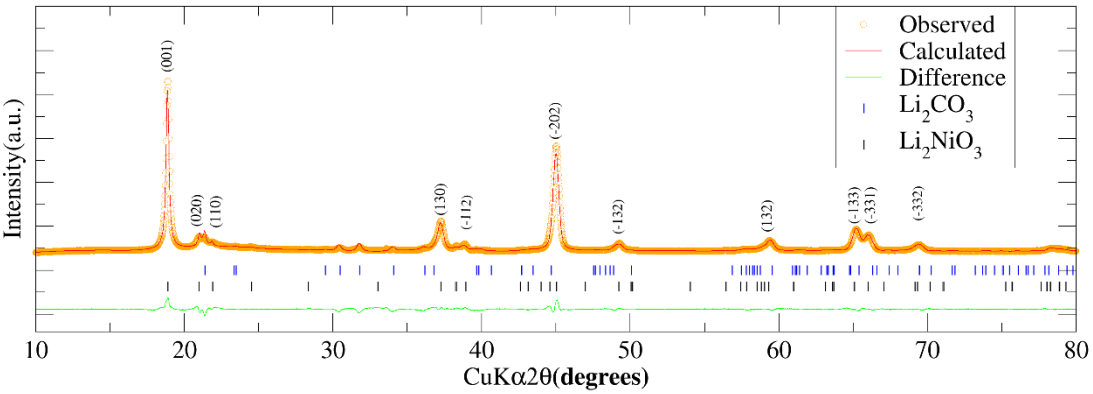

c) high NH_3

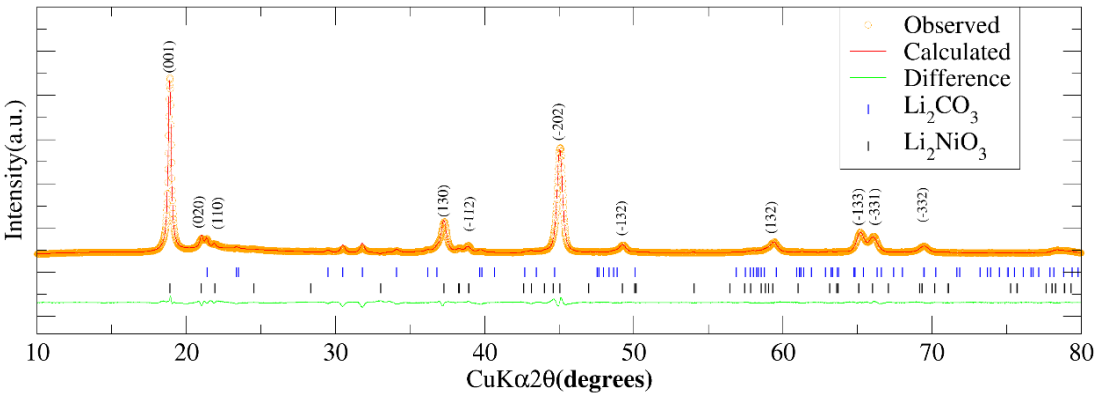

Fig S3.2 Rietveld refinements of lab PXRD data of Li_2NiO_3 synthesised by precursors made with different NH_3 concentration, low to high from a) to c), respectively.

Table S3.2

a) Lattice parameters and crystallite sizes from Scherrer equation for Li_2NiO_3

Sample	low NH_3 Li_2NiO_3	mid NH_3 Li_2NiO_3	high NH_3 Li_2NiO_3
a(Å)	4.92(3)	4.92(3)	4.91(3)
b(Å)	8.466(6)	8.464(7)	8.464(6)
c(Å)	4.98(3)	4.97(3)	4.98(3)
β (°)	109.18(2)	109.20(9)	109.19(9)
V($Å^3$)	195.7(2)	196.0(2)	195.8(2)
R_{wp}	0.0327	0.03078	0.02602
X^2	2.26	2.496	2.256
Crystallite Size (nm)	20.95±1.74	19.93±1.99	20.34±2.10

b) Transition metal (Ni) occupancy(g) at each site and Li_2NiO_3 calculated Ni per chemical formula

Sample	low NH_3 Li_2NiO_3	mid NH_3 Li_2NiO_3	high NH_3 Li_2NiO_3	Li_2NiO_3 standard
g_{4g}	0.754(1)	0.754(3)	0.755(4)	0.78(2)
g_{2b}	0.557(4)	0.526(2)	0.533(5)	0.41(2)
g_{2c}	0	0	0	0
g_{4h}	0.028(2)	0.038(8)	0.033(0)	0.02(2)
g_{total}[a]	0.707(3)	0.704(1)	0.703(3)	0.67(3)

a) 0 Li excess

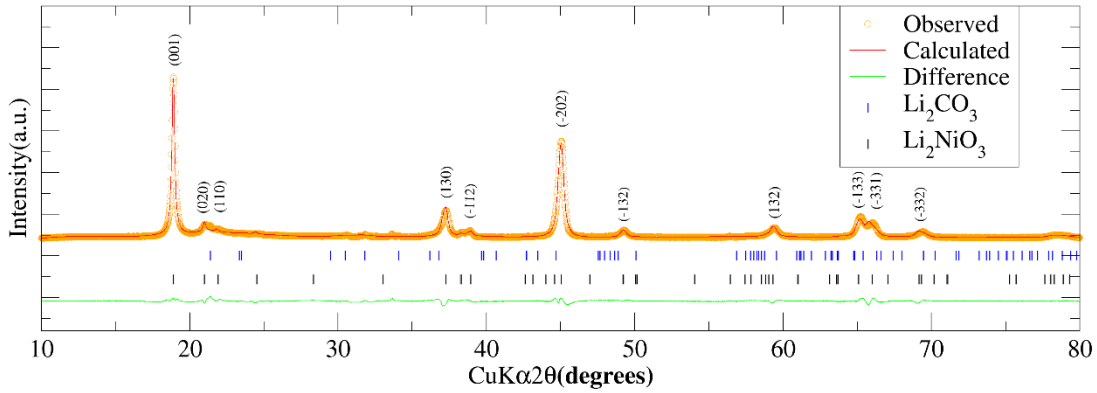

b) 3% Li excess

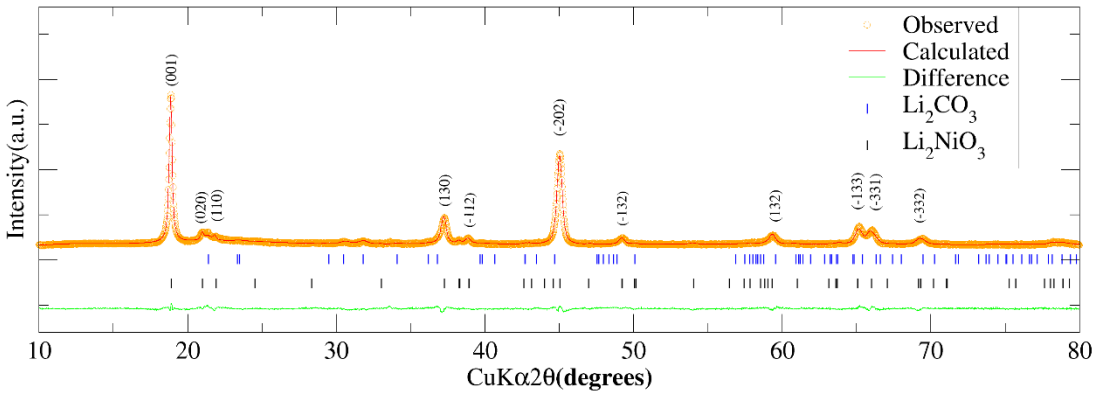

c) 5% Li excess

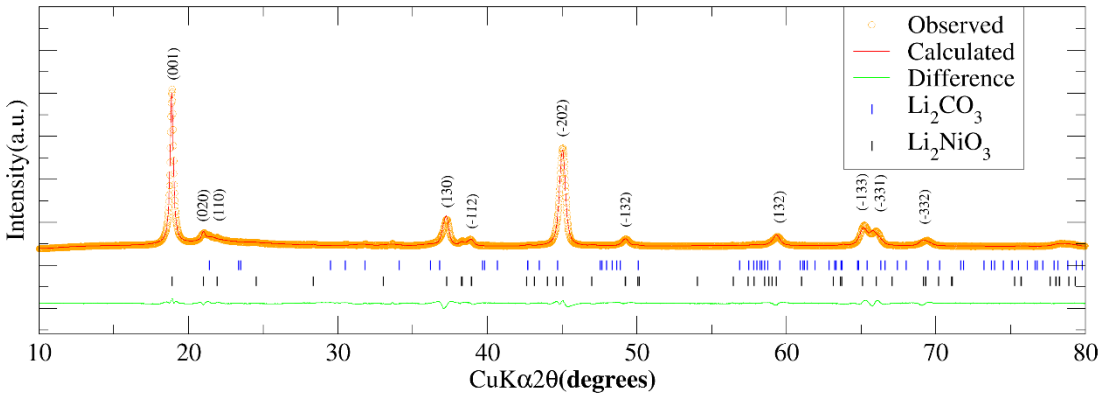

Fig S3.3 Rietveld refinements of lab PXRD data of Li_2NiO_3 synthesised by different Li excess amount, 0, 3%, 5% for a), b), and c) respectively.

Table S3.3

a) Lattice parameters and crystallite sizes from Scherrer equation for the Li_2NiO_3

Sample	0 Li excess Li_2NiO_3	3% Li excess Li_2NiO_3	5% Li excess Li_2NiO_3
a(Å)	4.926(4)	4.925(6)	4.917(3)
b(Å)	8.468(2)	8.465(5)	8.466(6)
c(Å)	4.97(9)	4.97(9)	4.98(3)
β (°)	109.23(8)	109.23(2)	109.18(2)
V($Å^3$)	196.1(4)	196.0(5)	195.7(2)
R_{wp}	0.03129	0.03305	0.0327
X^2	2.632	2.662	2.26
Crystallite Size (nm)	19.47±1.58	20.68±2.90	20.95±1.78

5% Li excess NH_3

b) Transition metal(Ni) occupancy(g) at each site and Li_2NiO_3 calculated Ni per chemical formula

Sample	0 Li excess Li_2NiO_3	3% Li excess Li_2NiO_3	5% Li excess Li_2NiO_3	Li_2NiO_3 standard
g_{4g}	0.739(6)	0.745(3)	0.754(1)	0.78(2)
g_{2b}	0.578(0)	0.540(8)	0.557(4)	0.41(2)
g_{2c}	0	0	0	0
g_{4h}	0.055(2)	0.079(8)	0.028(2)	0.02(2)
g_{total}[a]	0.722(5)	0.730(3)	0.707(3)	0.67(3)

a) 1°C/min

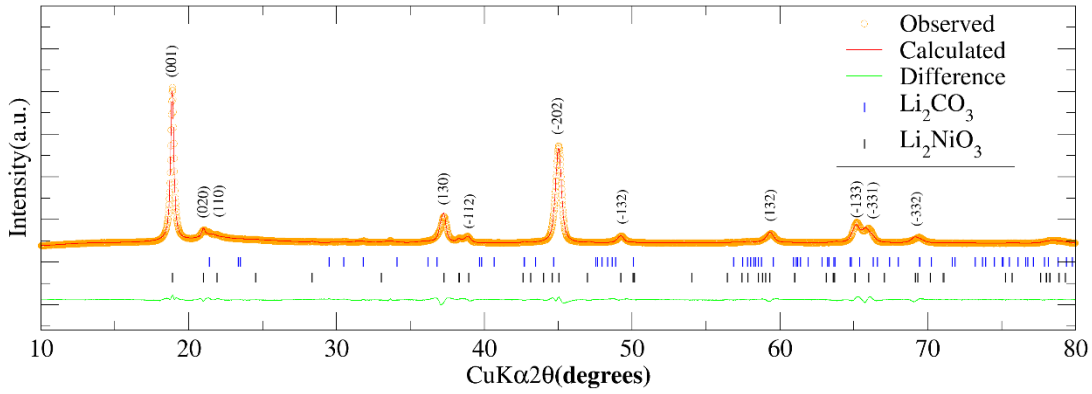

b) 3°C/min

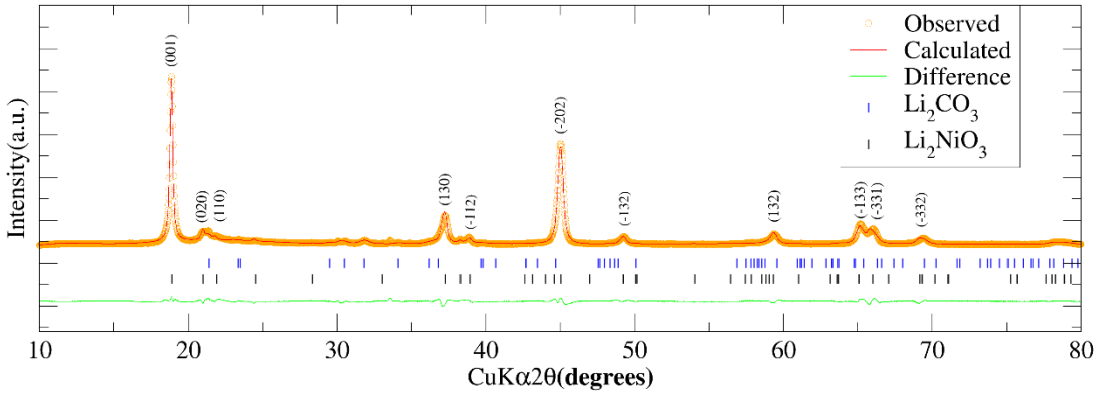

c) 5°C/min

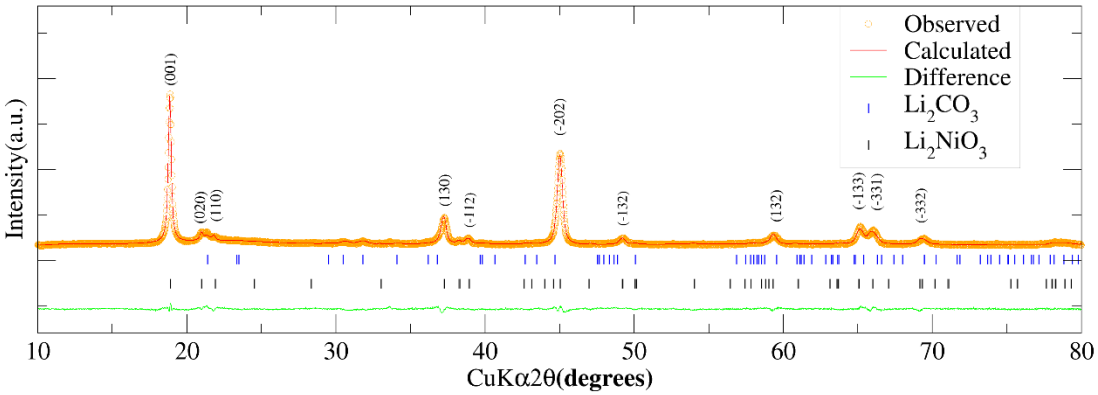

Fig S3.4 Rietveld refinements of lab PXRD data of Li_2NiO_3 synthesised with different calcination heat/cool rate (1, 3 and 5°C/min) for a), b) and c) respectively.

Table S3.4

a) Lattice parameters and crystallite sizes from Scherrer equation for the Li_2NiO_3

Sample	1°C/min Li_2NiO_3	3°C/min Li_2NiO_3	5°C/min Li_2NiO_3
a(Å)	4.926(1)	4.925(6)	4.921(7)
b(Å)	8.466(5)	8.465(5)	8.465(4)
c(Å)	4.97(9)	4.97(9)	4.97(9)
β (°)	109.21(3)	109.23(2)	109.20(2)
V($Å^3$)	196.1(1)	196.1(5)	195.9(1)
R_{wp}	0.02606	0.03305	0.02822
X^2	1.816	2.662	2.117
Crystallite Size (nm)	19.32±1.67	20.68±2.90	20.37±2.18

b)Transition metal (Ni) occupancy(g) at each site and Li_2NiO_3 calculated Ni per chemical formula

Sample	1°/min Li_2NiO_3	3°/min Li_2NiO_3	5°/min Li_2NiO_3	Li_2NiO_3 standard
g_{4g}	0.748(1)	0.754(1)	0.755(5)	0.78(2)
g_{2b}	0.536(8)	0.557(4)	0.565(2)	0.41(2)
g_{2c}	0	0	0	0
g_{4h}	0.055(2)	0.028(2)	0.040(5)	0.02(2)
g_{total}[a]	0.725(4)	0.707(3)	0.719(0)	0.67(3)

a) 550

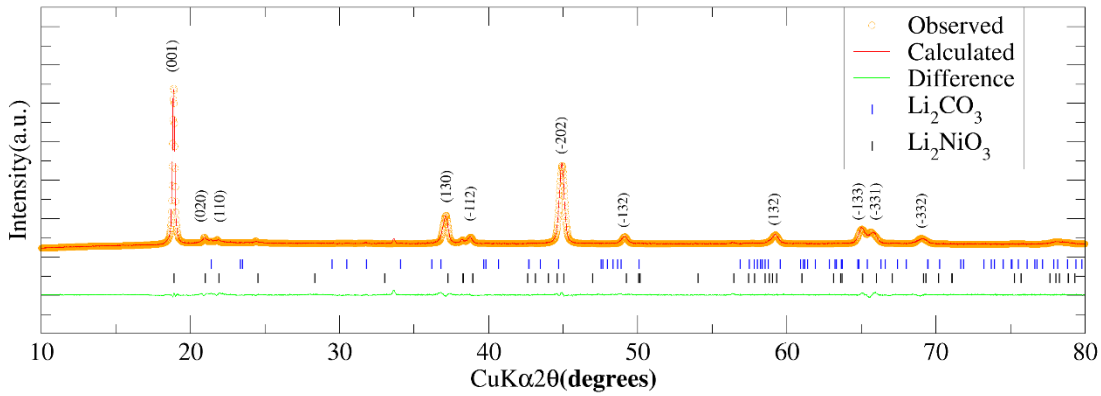

b) 575

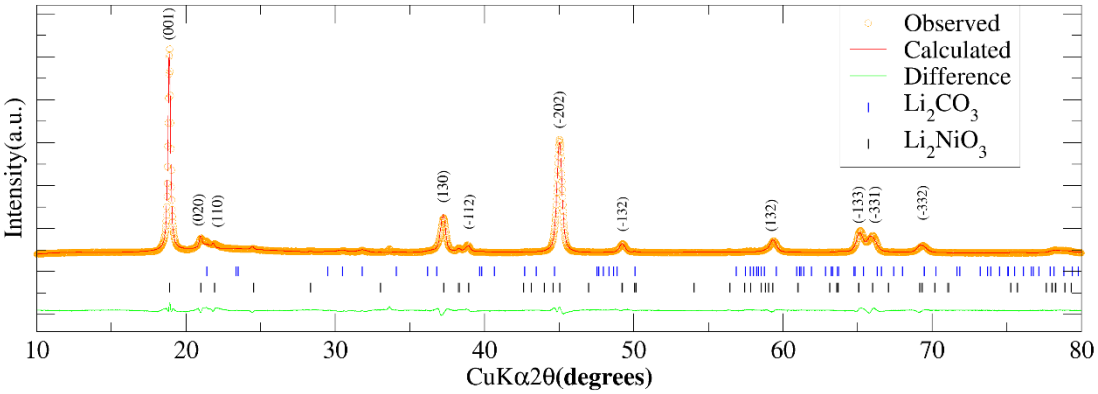

c) 600

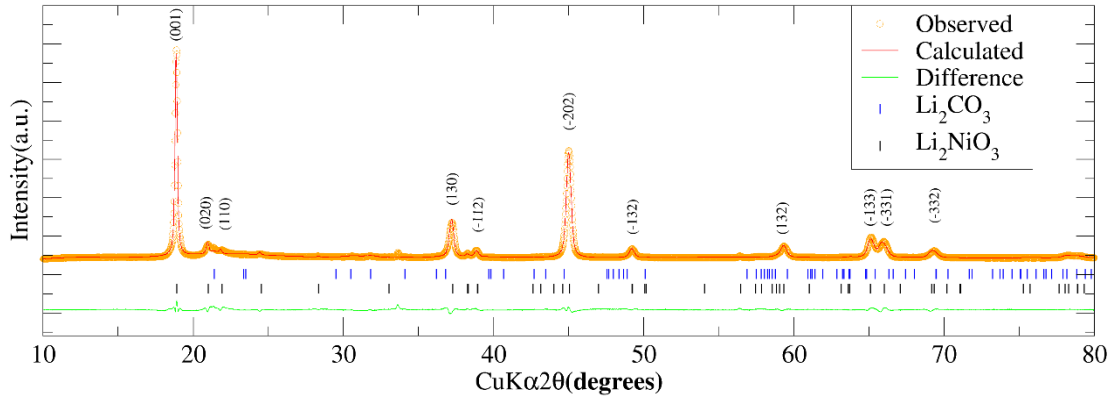

d) 625

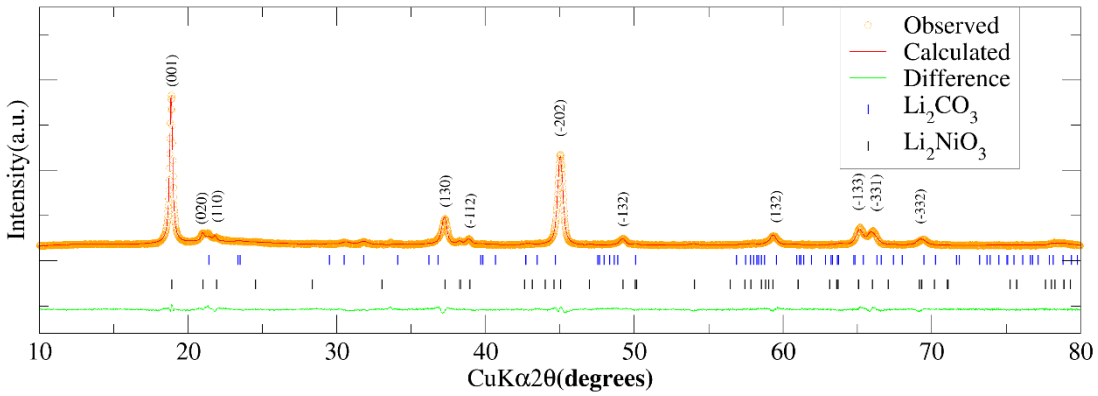

e) 650

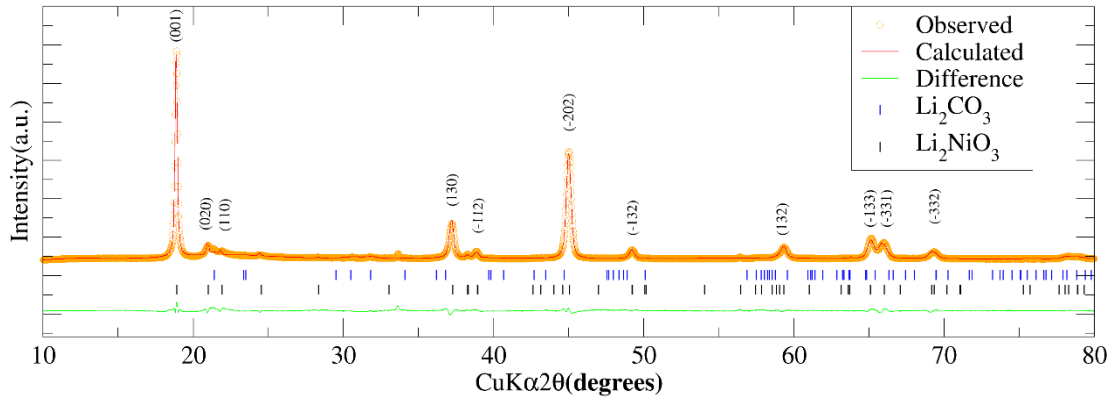

e) 660

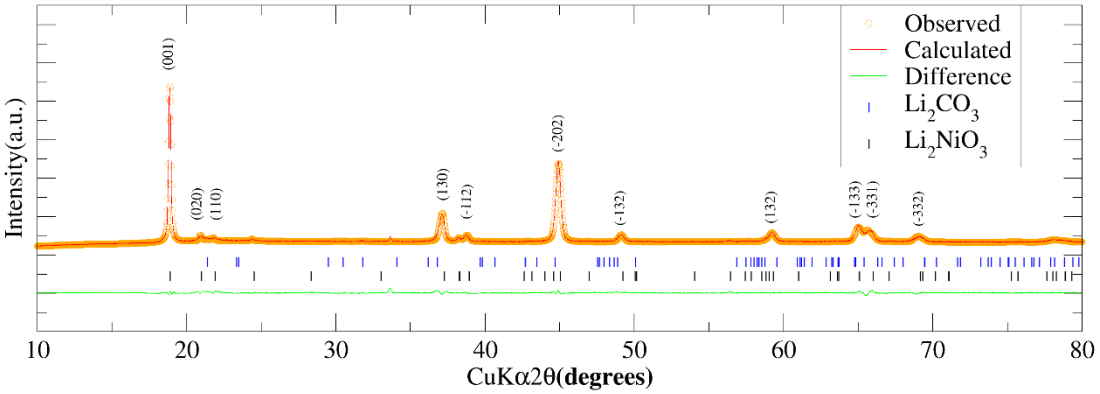

f) 675

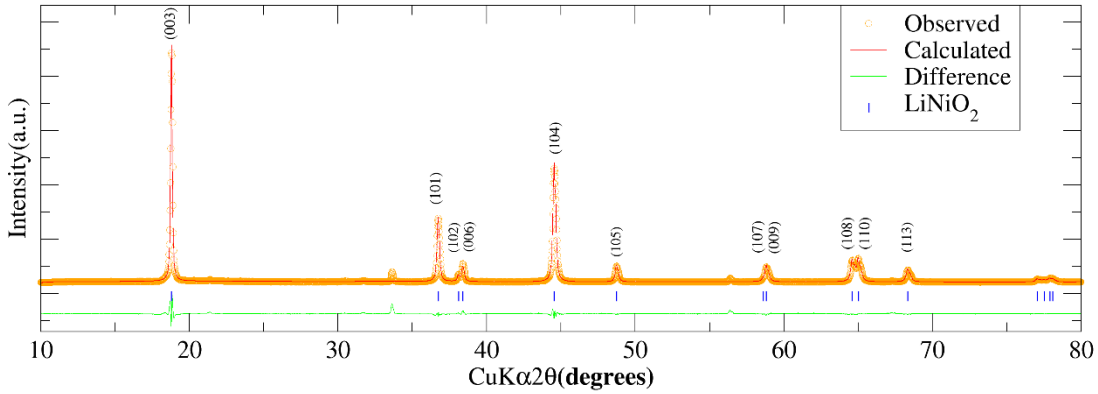

Fig3.5 a)-g) Rietveld refinements of lab PXRD data of Li_2NiO_3 phases synthesised from 550 to 660°, orange dots represent observed data and red solid line is the calculated pattern, the green line represents the difference curve. Upper ticks are from Li_2CO_3, lower ticks from Li_2NiO_3. h) PXRD data of LNO675 phases refined with hexagonal phase $LiNiO_2$.

Table3.5 a) Calculated lattice parameters for Li_2NiO_3 from 550-660°C samples obtained from Rietveld refinements of lab PXRD data. b) Structure parameter details for sample from 550°C.

a) Lattice parameters and crystallite sizes from Scherrer equation for 550-660°C Li_2NiO_3 phases

Sample	$Li_2NiO_3$550	$Li_2NiO_3$575	$Li_2NiO_3$600	$Li_2NiO_3$625	$Li_2NiO_3$650	$Li_2NiO_3$660
a(Å)	4.917(3)	4.919(8)	4.920(4)	4.923(3)	4.938(1)	4.961(1)
b(Å)	8.466(6)	8.471(6)	8.478(1)	8.484(1)	8.499(4)	8.541(7)
c(Å)	4.98(3)	4.98(1)	4.982(3)	4.984(3)	4.988(9)	4.992(9)
β (°)	109.18(2)	109.21(1)	109.21(6)	109.23(8)	109.28(1)	109.29(4)
V($Å^3$)	195.7(2)	196.0(1)	196.2(6)	193.5(7)	197.6(4)	199.6(9)
R_{wp}	0.0327	0.02851	0.02937	0.03014	0.02916	0.03651
X^2	2.26	2.146	2.256	2.396	3.34	3.496
I(110)/I(020)	0.84	0.85	0.86	0.88	0.89	0.91
Crystallite Size (nm)	20.68±2.90	23.18±1.78	25.25±1.84	26.75±1.60	26.79±2.02	27.65±1.44

*LNO675 crystallite size is 50 nm

b) Structural parameter details for the Li_2NiO_3 phase from the sample prepared at 550°C

		atomic position				
atoms	Wycyoff position	x/a	y/b	z/c	Biso	Occ
Ni	4g	0	0.174(8)	0	0.66(3)	0.75(4)
Li_{Ni}	4g	0	0.174(8)	0	0.33(7)	0.24(6)
Li	2b	0	0.5	0	0.36(6)	0.44(3)
Ni_{Li}	2b	0	0.5	0	0.63(4)	0.55(7)
Li	2c	0	0	0.5	1.00	1.00
Ni_{Li}	2c	0	0	0.5	0	0
Li	4h	0	0.66(2)	0.5	0.94(6)	0.97(2)
Ni_{Li}	4h	0	0.66(2)	0.5	0.05(4)	0.02(8)
O	4i	0.173(4)	0	0.172(5)	0.9	0.9
O	8j	0.270(8)	0.316(2)	0.238(8)	1.0	1.0

c) Transition metal (Ni) occupancy(g) at each site and Li_2NiO_3 calculated Ni per chemical formula

Sample	$Li_2NiO_3$550	$Li_2NiO_3$575	$Li_2NiO_3$600	$Li_2NiO_3$625	$Li_2NiO_3$650	$Li_2NiO_3$660	Li_2NiO_3 standard
g_{4g}	0.754(1)	0.768(7)	0.771(1)	0.801(0)	0.794(4)	0.855(2)	0.78(2)
g_{2b}	0.557(4)	0.554(1)	0.569(2)	0.573(3)	0.681(1)	0.820(7)	0.41(2)
g_{2c}	0	0	0	0	0	0	0
g_{4h}	0.028(2)	0.034(5)	0.028(0)	0.026(3)	0.073(3)	0.018(1)	0.02(2)
g_{total}[a]	0.707(3)	0.720(1)	0.722(4)	0.741(9)	0.805(5)	0.855(7)	0.67(3)

d) Lattice parameters and Ni occupancy and calculated transition metal content per chemical formula for hexagonal LNO

Sample	a(Å)	c(Å)	V($Å^{-3}$)	g_{3a}	g_{3b}	g_{total}[b]
LNO675	2.86742(8)	14.1962(3)	100.874(2)	0.0135(2)	0.9512(4)	0.9647(6)
LNOstandard[34]	2.87444(3)	14.18070(15)	101.4964(18)	0.0103(6)	1	1.010(1)

g_{total}[b] means Ni chemical formula, $g_{total}=g_{3a}+g_{3b}$.

References

(1) Ghosh, S.; Bhattacharjee, U.; Bhowmik, S.; Martha, D. S. K. A Review on High-Capacity and High-Voltage Cathodes for Next-Generation Lithium-Ion Batteries. *J. Energy Power Technol.* **2022**, *4* (1), 1–77. https://doi.org/10.21926/jept.2201002.

(2) Thao, L. T.; Truong, P. V.; Bo, N. V.; The Son, L.; Tuan, N. V.; Tien Phat, D.; Quang Dat, N.; Ky, N. V.; Lan, N. T.; Nguyen, T. V. Augmenting Electrochemical Performance of Nickel-Rich NMC for Lithium-Ion Batteries by Combining Material Synthesis Modification and Redistribution of Transition Metal Ion Concentration. *J. Phys. Chem. Solids* **2023**, *183*, 111616. https://doi.org/10.1016/j.jpcs.2023.111616.

(3) El Kharbachi,A.; Zavorotynska, O.; Latroche, M.; Cuevas,F.; Yartys,V.; Fichtner, M. Exploits, Advances and Challenges Benefiting beyond Li-Ion Battery Technologies. *J. Alloys Compd.* **2020**, 817, 153261. https://doi.org/10.1016/j.jallcom.2019.153261.

(4) Kim, M.; Kang,B.; Jeon,M.; Ko,M.; Chae, S. Co-Precipitation under Various Conditions (pH, Ammonia Concentration, and Temperature) for Co-Free Precursor Synthesis. *J. Korean Battery Soc.* **2023**, *2*, 158–164. https://doi.org/10.53619/KOBS.2022.12.2.2.158.

(5) Ghosh,A.; Foster, J. M.; Offer, G.; Marinescu, M. A Shrinking-Core Model for the Degradation of High-Nickel Cathodes (NMC811) in Li-Ion Batteries: Passivation Layer Growth and Oxygen Evolution. *J. Electrochem. Soc.* **2021**, *168* (2), 020509. https://doi.org/10.1149/1945-7111/abdc71.

(6) Rong, H.; Xu, M.; Xing, L.; Li, W. Enhanced Cyclability of $LiNi_{0.5}Mn_{1.5}O_4$ Cathode in Carbonate Based Electrolyte with Incorporation of Tris (Trimethylsilyl)Phosphate (TMSP). *J. Power Sources* **2014**, *261*, 148–155. https://doi.org/10.1016/j.jpowsour.2014.03.032.

(7) Ruess, R.; Schweidler, S.; Hemmelmann, H.; Conforto, G.; Bielefeld,A.; Weber, D. A.; Sann, J.; Elm, M. T.; Janek, J. Influence of NCM Particle Cracking on Kinetics of Lithium-Ion Batteries with Liquid or Solid Electrolyte. *J. Electrochem. Soc.* **2020**, *167* (10), 100532. https://doi.org/10.1149/1945-7111/ab9a2c.

(8) Tan, L.; Li, Z.; Tong, Z.; Wang, Z.; Li, Y.; Wang, L.; Shang, Y.; Bi, J.; Lei, S. Research Progress on Lithium-Rich Manganese-Based Lithium-Ion Batteries Cathodes. *Ceram. Int.* **2024**, 50 (4), 5877–5892. https://doi.org/10.1016/j.ceramint.2023.11.386.

(9) Shinova, E.; Zhecheva, E.; Stoyanova, R.; Bromiley, G. D. High-Pressure Synthesis of Solid Solutions between Trigonal $LiNiO_2$ and Monoclinic $Li[Li_{1/3}Ni_{2/3}]O_2$. *J. Solid State Chem.* **2005**, *178* (5), 1661–1669. https://doi.org/10.1016/j.jssc.2005.03.007.

(10) Wang, L.; Shi, Q.; Zhan, C.; Liu, G. One-Step Solid-State Synthesis of Ni-Rich Cathode Materials for Lithium-Ion Batteries. *Materials* **2023**, *16* (8), 3079. https://doi.org/10.3390/ma16083079.

(11) Li, Y.; Wang, X.; Ding, L.; Li, Y.; He, R.; Li, J. Changing the Calcination Temperature to Tune the Microstructure and Polishing Properties of Ceria Octahedrons. *RSC Adv.* **2022**, 12 *(*26), 16554–16560. https://doi.org/10.1039/D2RA02367A.

(12) Bianchini, M.; Schiele, A.; Schweidler, S.; Sicolo, S.; Fauth, F.; Suard, E.; Indris, S.; Mazilkin,A.; Nagel, P.; Schuppler, S.; Merz, M.; Hartmann, P.; Brezesinski, T.; Janek, J. From $LiNiO_2$ to $Li2NiO_3$: Synthesis, Structures and Electrochemical Mechanisms in Li-Rich Nickel Oxides. *Chem. Mater.* **2020**, *32* (21), 9211–9227. https://doi.org/10.1021/acs.chemmater.0c02880.

(13) Bianchini, M.; Roca-Ayats, M.; Hartmann, P.; Brezesinski, T.; Janek, J. There and Back Again—The Journey of $LiNiO_2$ as a Cathode Active Material. *Angew. Chem. Int. Ed.* **2019**, *58* (31), 10434–10458. https://doi.org/10.1002/anie.201812472.

(14) Li,N.; Sallis, S.; Papp, J. K.; McCloskey, B. D.; Yang,W.; Tong,W. Correlating the Phase Evolution and Anionic Redox in Co-Free Ni-Rich Layered Oxide Cathodes. *Nano Energy* **2020**, 78, 105365. https://doi.org/10.1016/j.nanoen.2020.105365.

(15) Guo, F.; Xie, Y.; Zhang, Y. Tuning Li-Excess to Optimize Ni/Li Exchange and Improve Stability of Structure in $Li_{0.8}Ni_{0.1}Co_{0.1}MnO_2$ Cathode Material for Lithium-Ion Batteries. *Nano Res.* **2022**, *15* (10)8962–8971. https://doi.org/10.1007/s12274-022-4532-y.

(16) Bruce, P. G.; Scrosati, B.; Tarascon, J.-M. Nanomaterials for Rechargeable Lithium Batteries. *Angew. Chem. Int. Ed.* **2008**, *47* (16), 2930–2946. https://doi.org/10.1002/anie.200702505.

(17) Balaya, P.; Bhattacharyya, A. J.; Jamnik, J.; Zhukovskii, Yu. F.; Kotomin, E. A.; Maier, J. Nanoionics in the Context of Lithium Batteries. J. Power Sources 2006, 159 (1), 171–178. https://doi.org/10.1016/j.jpowsour.2006.04.115.

(18) Aricò, A. S.; Bruce, P.; Scrosati, B.; Tarascon, J.-M.; van Schalkwijk, W. Nanostructured Materials for Advanced Energy Conversion and Storage Devices. Nat. Mater. 2005, 4 (5), 366–377. https://doi.org/10.1038/nmat1368.

(19) Maier, J. Size Effects on Mass Transport and Storage in Lithium Batteries. *J. Power Sources* **2007**, *174*(2), 569–574. https://doi.org/10.1016/j.jpowsour.2007.06.246.

(20) Martha, S. K.; Sclar, H.; Szmuk Framowitz, Z.; Kovacheva, D.; Saliyski, N.; Gofer, Y.; Sharon, P.; Golik, E.; Markovsky, B; Aurbach, D. A Comparative Study of Electrodes Comprising Nanometric and Submicron Particles of $LiNi_{0.50}Mn0.50O_2$, $LiNi_{0.33}Mn_{0.33}Co_{0.33}O_2$, and $LiNi_{0.40}Mn_{0.40}Co_{0.20}O_2$ Layered Compounds. *J. Power Sources* **2009**, *189* (1), 248–255. https://doi.org/10.1016/j.jpowsour.2008.09.090.

(21) Sclar, H.; Kovacheva, D.; Zhecheva, E.; Stoyanova, R.; Lavi,R.; Kimmel, G.; Grinblat,J.; Girshevitz, O.; Amalraj, F.; Haik, O.; Zinigrad, E.; Markovsky, B.; Aurbach, D. On the Performance of $LiNi_{1/3}Mn_{1/3}Co_{1/3}O_2$ Nanoparticles as a Cathode Material for Lithium-Ion Batteries. *J. Electrochem. Soc.* **2009**, *156*, A938. https://doi.org/10.1149/1.3212850.

(22) Park, S.-H.; Sato, Y.; Kim, J.-K.; Lee, Y.-S. Powder Property and Electrochemical Characterization of Li_2MnO_3. Material. *Mater. Chem. Phys.***2007**,*102*(2–3),225–230. https://doi.org/10.1016/j.matchemphys.2006.12.008.

(23) Rougier, A.; Gravereau, P.; Delmas, C. Optimization of the Composition of the $Li_{1-z}Ni_{1+z}O_2$ Electrode Materials: Structural, Magnetic, and Electrochemical Studies. *J. Electrochem. Soc.* **1996**. https://doi.org/10.1149/1.1836614.

(24) Zheng, J.; Ye, Y.; Liu, T.; Xiao, Y.; Wang, C.; Wang, F.; Pan, F. Ni/Li Disordering in Layered Transition Metal Oxide: Electrochemical Impact, Origin, and Control. *Acc. Chem. Res.* **2019**, 52 *(*8), 2201–2209. https://doi.org/10.1021/acs.accounts.9b00033.

(25) I. Ahmed, M. L. Saboungi, D. L. Price, Crystal structure of $(Li_xK_{1-x})_2CO_3$ (x = 0, 0.43, 0.5, 0.62, 1) by neutron powder diffraction analysis, *J. Solid State Chem.* **1997**, *134*(2), 317–321. https://doi.org/10.1006/jssc.1997.0209.

(26) Li, J.; Liu, H.; Xia, J.; Cameron, A. R.; Nie, M.; Botton, G. A.; Dahn, J. R. The Impact of Electrolyte Additives and Upper Cut-off Voltage on the Formation of a Rocksalt Surface Layer in $LiNi_{0.8}Mn_{0.1}Co_{0.1}O_2$ Electrodes. *J. Electrochem. Soc.* **2017**, *164* (4), A655. https://doi.org/10.1149/2.0651704jes.

(27) Meng,Y. S.; Ceder, G.; Grey, C. P.; Yoon, W.-S.; Jiang, M.; Bréger, J.; Shao-Horn,Y. Cation Ordering in Layered O3 Li $[Ni_xLi_{1/3-2x/3}Mn_{2/3-x/3}]O_2$ ($0 \leq x \leq 1/2$) Compounds. *Chem. Mater.* **2005**, *17* (9), 2386–2394. https://doi.org/10.1021/cm047779m.

(28) Boulineau, A.; Croguennec, L.; Delmas, C.; Weill, F. Structure of Li_2MnO_3 with Different Degrees of Defects. *Solid State Ion.* **2010**, *180* (40), 1652–1659. https://doi.org/10.1016/j.ssi.2009.10.020.

(29) Lee, M.-H.; Kang, Y.-J.; Myung, S.-T.; Sun, Y.-K. Synthetic Optimization of Li $[Ni_{1/3}Co_{1/3}Mn_{1/3}]O_2$ via Co-Precipitation. *Electrochimica Acta* **2004**, *50*(4), 939–948. https://doi.org/10.1016/j.electacta.2004.07.038.

(30) Noh, M.; Cho, J. Optimized Synthetic Conditions of $LiNi_{0.5}Co_{0.2}Mn_{0.3}O_2$ Cathode Materials for High-Rate Lithium Batteries via Co-Precipitation Method. *J. Electrochem. Soc.* **2013**, 160 *(*1), A105–A111. https://doi.org/10.1149/2.004302jes.

(31) Holzwarth, U.; Gibson, N. The Scherrer Equation versus the "Debye-Scherrer Equation." *Nat. Nanotechnol.* **2011**, *6* (9), 534–534. https://doi.org/10.1038/nnano.2011.145.

(32) Jain, G.; Yang, J.; Balasubramanian, M.; Xu, J. J. Synthesis, Electrochemistry, and Structural Studies of Lithium Intercalation of a Nanocrystalline Li_2MnO_3 -like Compound. *Chem. Mater.* **2005**, *17* (15), 3850–3860. https://doi.org/10.1021/cm0503329.

(33) Thackeray, M. M.; Kang, S.-H.; Johnson, C. S.; Vaughey, J. T.; Benedek, R.; Hackney, S. A. Li_2MnO_3-Stabilized $LiMO_2$ (M = Mn, Ni, Co) Electrodes for Lithium-Ion Batteries. *J. Mater. Chem.* **2007**, *17* (30), 3112–3125. https://doi.org/10.1039/B702425H.

(34) Stoyanova, R.; Zhecheva, E.; Alcántara, R.; Tirado, J. L.; Bromiley, G.; Bromiley, F.; Boffa Ballaran, T. Lithium/Nickel Mixing in the Transition Metal Layers of Lithium Nickelate: High-Pressure Synthesis of Layered $Li[Li_xNi_{1-x}]O_2$ Oxides as Cathode Materials for Lithium-Ion Batteries. *Solid State Ion.* **2003**, *161* (3), 197–204. https://doi.org/10.1016/S0167-2738(03)00280-7.

(35) Tabuchi, M.; Kuriyama, N.; Takamori, K.; Imanari,Y.; Nakane, K. Appearance of Lithium-Excess $LiNiO_2$ with High Cyclability Synthesized by Thermal Decomposition Route from $LiNiO_2$ -Li_2NiO_3 Solid Solution. *J. Electrochem. Soc.* **2016**, *163* (10), A2312–A2317. https://doi.org/10.1149/2.0861610jes.

(36) Kalyani, P.; Chitra, S.; Mohan, T.; Gopukumar, S. Lithium Metal Rechargeable Cells Using Li_2MnO_3 as the Positive Electrode. *J. Power Sources* **1999**, 80 (1–2), 103–106. https://doi.org/10.1016/S0378- 7753(99)00066-X.

(37) Wu, Y.; Manthiram, A. Effect of Surface Modifications on the Layered Solid Solution Cathodes $(1-z)\ Li[Li_{1/3}Mn_{2/3}]O_2$-$(z)Li[Mn_{0.5}$-$yNi_{0.5}$-$yCo_2y]O_2$. *Solid State Ion.* **2009**, *180*(1), 50–56. https://doi.org/10.1016/j.ssi.2008.11.002.

(38) Armstrong,A. R.; Holzapfel, M.; Novák, P.; Johnson, C. S.; Kang, S.-H.; Thackeray, M. M.; Bruce, P. G. Demonstrating Oxygen Loss and Associated Structural Reorganization in the Lithium Battery Cathode $Li[Ni_{0.2}Li_{0.2}Mn_{0.6}]O_2$. *J. Am. Chem. Soc.* **2006**, *128* (26), 8694–8698. https://doi.org/10.1021/ja062027. (39) Riewald, F.; Kurzhals, P.; Bianchini, M.; Sommer, H.; Janek, J.; Gasteiger, H. A. The LiNiO2 Cathode Active Material: A Comprehensive Study of Calcination Conditions and Their Correlation with Physicochemical Properties Part II. Morphology. *J. Electrochem. Soc.* **2022**, 169 (2), 020529. https://doi.org/10.1149/1945-7111/ac4bf3.

(40) Yu, D.; Yanagida, K.; Kato, Y.; Nakamura, H. Electrochemical Activities in Li_2MnO_3. *J. Electrochem. Soc.* **2009**, *156*. https://doi.org/10.1149/1.3110803.

(41) Kong,J.-Z.; Wang, S.-S.; Tai,G.-A.; Zhu,L.; Wang, L.-G.; Zhai,H.-F.; Wu,D.; Li,A.-D.; Li,H. Enhanced Electrochemical Performance of $LiNi_{0.5}Co_{0.2}Mn_{0.3}O_2$ Cathode Material by Ultrathin ZrO_2 Coating. *J. Alloys Compd.* **2016**, *657*, 593–600. https://doi.org/10.1016/j.jallcom.2015.10.187.

(42) Han, C.-H.; Kim, J.-H.; Paeng, S.-H.; Kwak, D.-J.; Sung, Y.-M. Electrochemical Characteristics of $LiNiO_2$ Films Prepared for Charge Storable Electrode Application. *Thin Solid Films* **2009**, *517* (14), 4215–4217. https://doi.org/10.1016/j.tsf.2009.02.046.

(43) Xiang,Y.; Wu,X. Enhanced Electrochemical Performances of Li_2MnO_3 Cathode Materials by Al Doping. *Ionics* **2018**, *24*. https://doi.org/10.1007/s11581-017-2189-4.

(44) Chung, H.-T.; Myung, S.-T.; Cho, T.-H.; Son, J.-T. Lattice Parameter as a Measure of Electrochemical Properties of $LiMn_2O_4$. *J. Power Sources* **2001**, *97*, 454–457. https://doi.org/10.1016/S0378-7753(01)00685-1.

(45) Zhang, S. S.; Jow, T. R. Optimization of Synthesis Condition and Electrode Fabrication for Spinel $LiMn_2O_4$ Cathode. J. Power Sources 2002, 109 (1), 172–177.https://doi.org/10.1016/S0378-7753(02)00063-0

(46) Ryu, H.-H.; Kang, G.-C.; Ismoyojati, R.; Park, G.-T.; Maglia, F.; Sun,Y.-K. Intrinsic Weaknesses of Co- Free Ni–Mn Layered Cathodes for Electric Vehicles. *Mater. Today* **2022**, *56*. https://doi.org/10.1016/j.mattod.2022.03.005.

(47) Ju, S. H.; Kim, D.-W. Effect of Calcination Temperature on the Structure and Electrochemical Performance of $LiMn_{1.5}Ni_{0.5}O_4$ Cathode Materials. *Bull. Korean Chem. Soc.* **2013**, *34*. https://doi.org/10.5012/bkcs.2013.34.1.59.

(48) Li, L.; Chen, J.; Huang, H.; Tan, L.; Song, L.; Wu, H.-H.; Wang, C.; Zhao, Z.; Yi, H.; Duan, J.; Dong, T. Role of Residual Li and Oxygen Vacancies in Ni-Rich Cathode Materials. *ACS Appl. Mater. Interfaces* **2021**，*13* (36), 42554–42563. https://doi.org/10.1021/acsami.1c06550.

(49) Hua-jun, G.; Ru-fu, L.; Xin-hai, L.; Xin-ming, Z.; Zhi-xing, W.; Wen-jie, P.; Zhao, W. Effect of Calcination Temperature on Characteristics of $LiNi_{1/3}Co_{1/3}Mn_{1/3}O_2$ Cathode for Lithium Ion Batteries. *Trans Nonferrous Met Soc China* **2007**.

(50) Wei, G.-Z.; Lu, X.; Ke, F.-S.; Huang, L.; Li, J.-T.; Wang, Z.-X.; Zhou, Z.-Y.; Sun, S.-G. Crystal Habit-Tuned Nanoplate Material of $Li[Li_{1/3-2x/3}Ni_xMn_{2/3-x/3}]O_2$ for High-Rate Performance Lithium-Ion Batteries. *Adv. Mater.* **2010**, *22* (39), 4364–4367. https://doi.org/10.1002/adma.201001578.

(51) Wang, R.; He, X.; He, L.; Wang, F.; Xiao, R.; Gu, L.; Li, H.; Chen, L. Atomic Structure of Li_2MnO_3 after Partial Delithiation and Re-Lithiation. *Adv. EnergyMater.* **2013**, *3*(10), 1358–1367. https://doi.org/10.1002/aenm.201200842.

(52) Na, S.-H.; Kim, H.-S.; Moon, S.-I. Abs. 328, 206th Meeting, 2004 The Electrochemical Society, Inc.

(53) Lee, Y. S.; Yoon, C. S.; Sun,Y. K.; Yoshio, M. Structural Characterization of Mn-Based Materials Using γ-MnOOH Source. *Electrochem. Solid-State Lett.* **2001**, *5* (1), A1. https://doi.org/10.1149/1.1419702.

(54) Gallagher, K.; Nelson, P.; Dees, D. Simplified Calculation of the Area Specific Impedance for Battery Design. *Fuel Energy Abstr.* **2011**, *196*. https://doi.org/10.1016/j.jpowsour.2010.10.020.

(55) WebElements Periodic Table » Nickel » radii of atoms and ions. https://www.webelements.com/nickel/atom_sizes.html

(56) Bréger, J.; Jiang, M.; Dupré, N.; Meng, Y. S.; Shao-Horn, Y.; Ceder, G.; Grey, C. P. High-Resolution X- Ray Diffraction, DIFFaX, NMR and First Principles Study of Disorder in the Li_2MnO_3–$Li[Ni_{1/2}Mn_{1/2}]O_2$ Solid Solution. *J. Solid State Chem.* **2005**, *178* (9), 2575–2585. https://doi.org/10.1016/j.jssc.2005.05.027.

(57) Amalraj, S.; Sharon, D.; Talianker, M.; Julien, C.; Burlaka, L.; Lavi, R.; Zhecheva, E.; Markovsky, B.; Zinigrad, E.; Kovacheva, D.; Stoyanova, R.; Aurbach, D. Study of the Nanosized Li_2MnO_3: Electrochemical Behavior, Structure, Magnetic Properties, and Vibrational Modes. *Electrochimica Acta* **2013**, *97*, 259–270. https://doi.org/10.1016/j.electacta.2013.03.029.

(58) Boulineau, A.; Croguennec, L.; Delmas, C.; Weill, F. Reinvestigation of Li_2MnO_3 Structure: Electron Diffraction and High Resolution TEM. *Chem. Mater.* **2009**, *21* (18), 4216–4222. https://doi.org/10.1021/cm900998n.

(59) Baklanova, Ya. V.; Arapova, I. Yu.; Shein, I. R.; Maksimova, L. G.; Mikhalev, K. N.; Denisova, T. A. Charge Distribution and Mobility of Lithium Ions in Li_2TiO_3 from 6,7Li NMR Data. *J. Struct. Chem.* **2013**, *54* (1), 111–118. https://doi.org/10.1134/S002247661307010X.

(60) Park, H.; Park, H.; Song, K.; Song, S. H.; Kang, S.; Ko, K.-H.; Eum, D.; Jeon,Y.; Kim, J.; Seong,W. M.; Kim, H.; Park, J.; Kang, K. In Situ Multiscale Probing of the Synthesis of a Ni-Rich Layered Oxide Cathode Reveals Reaction Heterogeneity Driven by Competing Kinetic Pathways. *Nat. Chem.* **2022**, *14* (6), 614–622. https://doi.org/10.1038/s41557-022-00915-2.

(61) Mesnier, A.; Manthiram, A. Synthesis of $LiNiO_2$ at Moderate Oxygen Pressure and Long-Term Cyclability in Lithium-Ion Full Cells. *ACS Appl. Mater. Interfaces* **2020**, *12* (47), 52826–52835. https://doi.org/10.1021/acsami.0c16648.

(62) Chen, H.; Islam, M. S. Lithium Extraction Mechanism in Li-Rich Li_2MnO_3 Involving Oxygen Hole Formation and Dimerization. *Chem. Mater.* **2016**, *28* (18), 6656–6663. https://doi.org/10.1021/acs.chemmater.6b02870.

(63) Robertson,A. D.; Bruce, P. G. Mechanism of Electrochemical Activity in Li_2MnO_3. *Chem. Mater.* **2003**, *15* (10), 1984–1992. https://doi.org/10.1021/cm030047u.

(64) Reimers, J. N.; Fuller, E. W.; Rossen, E.; Dahn, J. R. Synthesis and Electrochemical Studies of $LiMnO_2$ Prepared at Low Temperatures. *J. Electrochem. Soc.* **1993**, *140* (12), 3396. https://doi.org/10.1149/1.2221101.

(65) Croy, J. R.; Kim, D.; Balasubramanian, M.; Gallagher, K.; Kang, S.-H.; Thackeray, M. M. Countering the Voltage Decay in High Capacity $xLi_2MnO_3 \bullet (1–x)LiMO_2$ Electrodes (M=Mn, Ni, Co) for Li^+-Ion Batteries. *J. Electrochem. Soc.* **2012**, *159* (6), A781–A790. https://doi.org/10.1149/2.080206jes.

(66) Jia,Y.; Ye, Y.; Liu, J.; Zheng, S.; Lin,W.; Wang,Z.; Li, S.; Pan, F.; Zheng, J. Breaking the Energy Density Limit of $LiNiO_2$: Li_2NiO_3 or Li_2NiO_2? *Sci. China Mater.* **2022**, *65* (4), 913–919. https://doi.org/10.1007/s40843-021-1827-x.

Chapter 4

Microwave-Assisted optimization of layered Li_2NiO_3 cathodes for LIBs

4.1 Introduction

The use of microwaves (MW) for the synthesis of inorganic compounds has become very important in recent years.[1,2] This innovative methodology can result in improved reaction yields and enhanced structural homogeneity of the product. Additionally, reactions can be carried out at lower temperatures compared to conventional synthesis methods.[2] The primary benefits of MW compared to conventional synthesis lie mostly in its superior heating characteristics. In contrast to conventional synthesis methods, microwave radiation directly interacts with the reaction components, resulting in selective heating of the sample and reduced energy consumption in the surrounding environment. As a result of the direct application of heat to the sample, materials heated by microwaves exhibit a temperature distribution that is the reverse of what is observed in traditional heating. This leads to a lower surface temperature compared to the inside temperature.[3,4] The instantaneous heating characteristic of MW results in a very rapid conversion of energy into heat, resulting in an extremely rapid temperature rise and fast reaction times that surpass those of traditional furnaces. Since the microwave heating process takes place directly in the sample, heating also occurs volumetrically. Within a homogeneous material, this implies that the process of heating is consistent and even over the entire sample. The temperature dependency of sample interaction with the MW field, sample inhomogeneities, and the MW field all contribute to a reduction in thermal uniformity in most real samples. Volumetric heating, in comparison to traditional heating, minimises the requirement for conductive heat transmission within the sample. This enables more

effective heating of relatively large samples and ensures a more uniform thermal history across the sample.[5] MW can be used to synthesize a variety of oxides such as $LiMn_2O_4$, $LiCoO_2$, $CuBi_2O_4$, and $Bi_4B_2O_9$, etc.[6-8]

Most chemical reactions triggered by MW rely on the heat effects generated by MW in various materials. The thermal effects primarily arise from the interaction between the electrical component of the microwave field and the charged particles present in the material. Electrostatic interactions produce motion in substances where coupled charges take the shape of dipoles until equilibrium is established. Generally, this mechanism dominates in solid materials and is known as conductive heating.[5]

It is generally accepted that energy is transferred from microwaves to materials through resonance or relaxation. Microwaves rapidly lose energy as they pass through dielectric materials, causing their electric fields to decay. The heating effect of materials exposed to microwave fields depends on the total electrical conductivity and the internal electric field. The greater the size, the higher the absorption of microwave energy by the material. Energy is readily transformed into chemical energy when it is absorbed to a sufficient degree because it accelerates the coupling material's diffusion and vibration and causes more activated species to form when reactants collide. Conversely, species that have been activated encourage diffusion within the crystal structure and between grain boundaries. This leads to a decrease in the energy required for diffusion, ultimately reducing the overall observed activation energy. Consequently, microwave irradiation can facilitate solid-state processes by reducing the required temperatures and reaction times.[9]

The absorbed power MW by the sample is directly related to the volume of the sample. Consequently, samples with very small volumes may not undergo a complete reaction. However, it

is important to take into account the penetration depth, as this indicates that very large samples are not suitable for obtaining products with high purity.[5] Therefore, the sample can react with high efficiency and increase purity for micron-sized lithium-rich and high-nickel oxides.

Therefore, as discussed in Chapter 3, we expect to optimize the sample under low-temperature MWconditions to achieve the purpose of improving structural uniformity and electrochemical performance.

4.2 Synthesis of Li_2NiO_3

The optimal conditions for synthesising Li_2NiO_3 can be achieved by employing low NH_3 $Ni(OH)_2$ with 3% Li excess under an oxygen environment, as covered in Chapter 3, and preheating at 300°C for 12 hours and at 550°C for 24 hours at a rate of 3°C/min.

Following the procedures in Chapter 3, the produced Li_2NiO_3 was placed into 10 ml alumina crucibles and ground in an Ar-filled glovebox (H_2O<0.1ppm, O_2<0.1ppm) (see Fig 4.1). Li_2NiO_3 in the alumina crucibles was placed in a Phoenix microwave muffle furnace from CEM (with a maximum output power of 1400 W and a microwave irradiation frequency of 2.45 GHz). The programme was set at 550°C for 1, 2, 3, 4, and 5 hours, with a heat/cool rate of 3°C/min from room temperature before being stored in the Ar filed glovebox. The samples of Li_2NiO_3 that were microwaved for 1, 2, 3, 4, and 5 hours are labeled as their MW-x numbers (x =1, 2, 3, 4, and 5 hours).

Fig 4.1 Reaction scheme used for the microwave-assisted optimization synthesis of Li_2NiO_3.

4.3 Microwave-Assisted optimization for Li_2NiO_3

4.3.1 SEM

According to Figure 4.2, the SEM images show that all the samples include particles of varied sizes and types. The samples in Fig4.1a), c), d), e), f), MW-1, 2, 3, 4, and 5 consist of agglomerations of multi- spherical secondary particles having a diameter of 5 μm. With an increase in microwave irradiation period, a minor rise in grain particle size was observed, reaching approximately 20 nm, which aligns with Kalyani's previous work.[10] However, compared to the pristine samples in Chapter 3, there is not a significant change. Miao's work on microwaved Li_2MnO_3 differs from our study due to variations in precursor selection and microwave conditions, resulting in uneven aggregation of 4-5 μm.[11] After calcining the pristine Li_2NiO_3, which can lessen the phenomena of uneven particle distribution and irregular agglomeration brought on by rapid microwave heating, we performed microwave-assisted optimization for Li_2NiO_3 in our tests.[11,12]

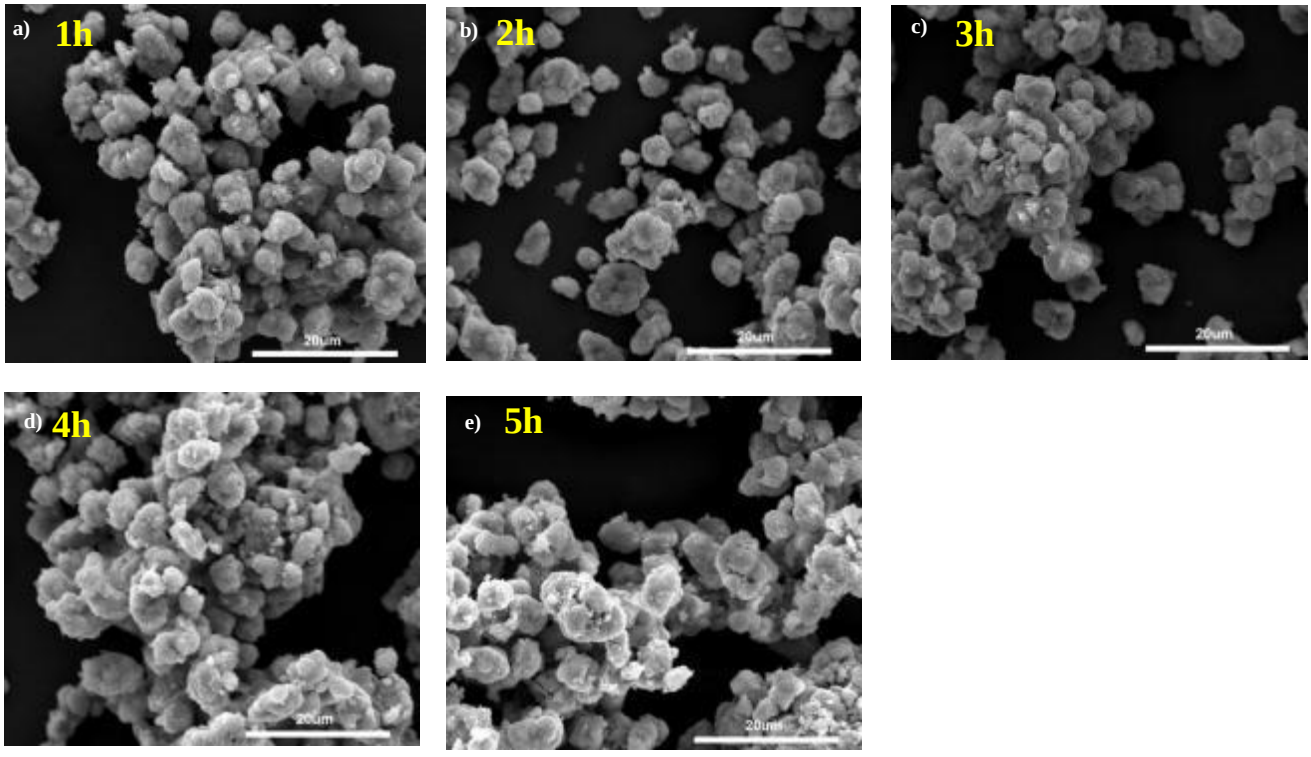

Fig 4.2 SEM images for MW-Li_2NiO_3 for (a)1h; (b) 2h; (c) 3h; (d) 4h; (e) 5h in 20 μm.

4.3.2 X-ray diffraction and Rietveld analysis

Based on the information provided in Figure 4.3, it can be shown that all the X-ray diffraction (XRD) patterns correspond to a monoclinic unit cell with the C2/m symmetry, which is characteristic of Li_2NiO_3.

The samples correspond to the ICSD standard data. However, even after microwave treatment, the impurity Li_2CO_3 remains present in the temperature range of 30-32° (as stated in Chapter 3). Furthermore, the amount of Li_2CO_3 tends to rise with longer exposure time, mostly due to prolonged contact with air (which contains CO_2) during the microwave process. As the temperature rises, there is no discernible change in the peak positions or intensity, in contrast to Bhat's discovery that the crystallinity is better.[13]

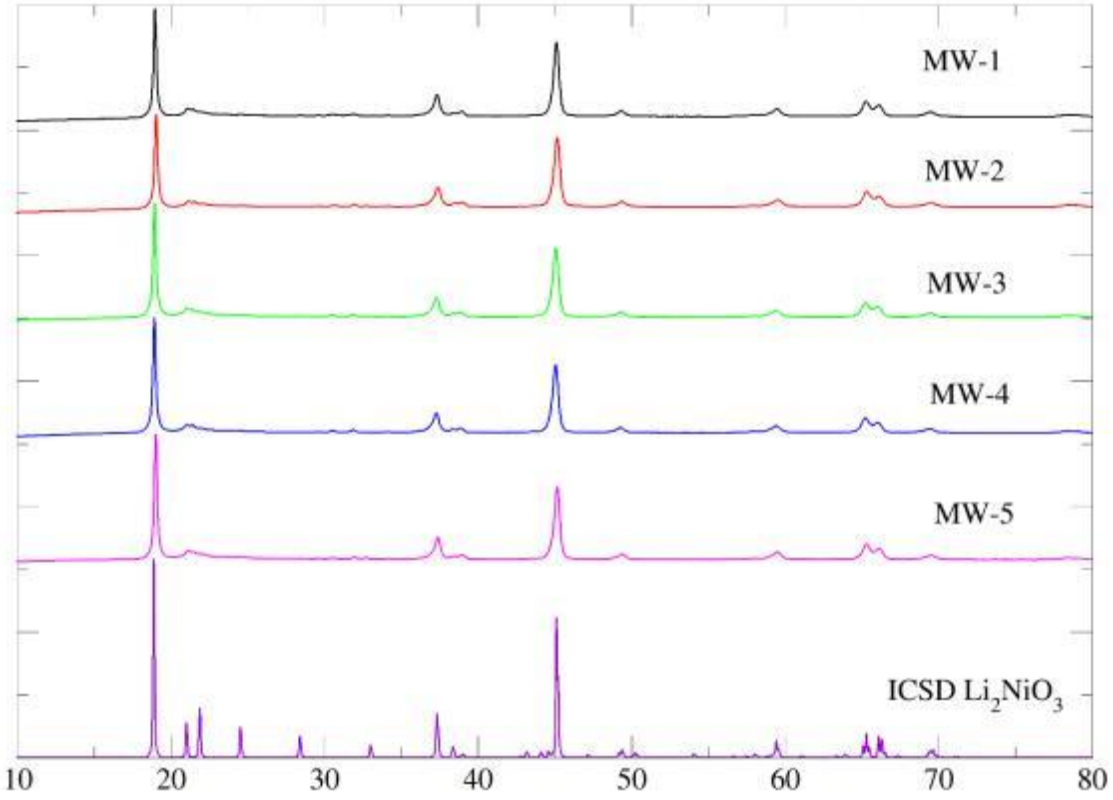

Fig 4.3 XRD comparison for MW-Li_2NiO_3 for a)1h, b) 2h, c) 3h, d) 4h, e) 5h.

The Rietveld refinement images, namely Fig S4.1, show that the synthesised MW samples exhibit distinct peaks at 2θ=65.3 and 65.8°, corresponding to (-1 3 3) and (-3 3 1), respectively. This indicates the presence of a well-developed monoclinic structure in the samples. In addition, the occurrence of the superlattice peak within the range of 20 to 30° is also a distinctive feature of Li_2NiO_3/Li_2MnO_3.[14-15] From Table S4.1, it is evident that the volume of the lattice experiences a slight increase as the microwave duration increases. This observation aligns with the behaviour described in Chapter 3. It is crucial to determine the ratio value of the peak intensity (I(110)/(020)) to identify stacking faults.[13,14] Apart from the stacking vector along the c-axis, there are two other stacking vectors to consider. A greater ratio value typically indicates fewer stacking faults, as demonstrated by Boulineau.[14] MW-2 sample exhibits a greater I(110)/(020) ratio compared to other samples, indicating a lower presence of stacking defects under these conditions. This results in a more stable structure, leading to better retention of capacity after 100 cycles, as depicted in Figure 4.3 b). Although the disappearance of peak (110) and the broadening of peak (020) are observed, there is no guarantee of maintaining the stacking order in the c direction or the shift from a layered structure to a disordered structure resembling spinel.[16] In the TableS4.1 b), the Ni occupancy increases at the sites 4g, 2b 4h and g_{total} when microwave time increases, indicating the Ni occupied the Li sites and lead to more serious cation mixing. Considering the radius of Li^+(0.76 Å), only Ni^{2+} exhibits a similar value (0.69Å). This means when Li is reinserted to the original sites during the discharge process, Ni^{2+} takes the sites and lower valence Ni(Ni^{2+}/Ni^{3+}) redox occurred.

4.3.3 Electrochemical testing

As depicted in Fig4.3 a), the initial discharge capacity of MW-Li_2NiO_3 rises a little to 300 $mAhg^{-1}$ falls to 250 $mAhg^{-1}$ and has a great increase to around 400 $mAhg^{-1}$ as the microwave time increases. It is clear that the initial charge curve can be mainly decomposed to two parts: a), The "S" section that appears from 2-4.4 V, including reactions of Ni^{2+} to Ni^{3+}/Ni^{4+} and delithiation of Li_2NiO_3.b), The "L" sector, which has a voltage range of 4.4 to 4.6 V, is where the activation of Li_2NiO_3 caused the release of Li_2O at the 4.4 V platform. Additionally, the active NiO_2 provided significant irreversible capacity and caused oxygen vacancies to arise.[17] When the voltage exceeds the range of 4.6 to 4.8 V, the Li_2NiO_3 phase tends to either disappear or undergo a transformation into a spinel structure.

All of the initial charge capacities above 500 $mAhg^{-1}$, except for MW-5 which has a capacity of roughly 450 $mAhg^{-1}$. This lower capacity is due to the irreversible loss of O^{2-} from the lattice at the oxidation threshold of 4.4 V in the reaction.[17,18] In other words, the irreversible capacity loss due to the lithium ions absence at sites in lithium layers during insertion because of O^{2-}vacancies occurring. The high coulomb efficiency of MW-5 (86.8%) can be explained by its longer microwave time compared to others, which is similar to higher temperatures. This longer microwave time helps prevent or delay the release of O_2 from the structure, allowing MW-5 to reach 4.4 V at around 160 $mAhg^{-1}$ and have a longer plateau before reaching 4.6 V, the point at which Li_2NiO_3 begins to disappear. However, MW-5 has a lower charge capacity for the initial cycle.[19]

When the electrode discharges, it encounters a plateau potential that steps down from 0.2 to 0.4 V. This phenomenon, known as voltage decay or fade, may be caused by the creation of an AB_2O_4 spinel-like structure during charge/discharge cycles.[20] Once the voltage drops to 3.6 V, some of the lithium ions are inserted into the transition metal (TM) ions' octahedral interaction

positions, leading to the production of layered $LiNiO_2$.[15,16] This mechanism also causes a disordered arrangement of cations between 3-3.6 V. The structure resembling a spinel is formed after 3 V when a rapid voltage decay takes place and a large number of lithium ions relocate into the original locations.[18] It is important to observe that in the MW-5, there is a delay in the voltage decay point from 3 to 2.5 V and another decay point at 0.8 V. These changes can be attributed to the formation of a more stable defect spinel phase and a reduction in the damage caused by O_2 loss.[16]

As depicted in Figure 4.3 b), MW-5 has the highest initial discharge capacity of approximately 400 $mAhg^{-1}$, while the others have capacities around 300 $mAhg^{-1}$ at the C/25 rate. However, throughout the first 20 cycles, the capacity of MW-5 decreases at a faster rate. MW-2 has a maximum capacity of 76 $mAhg^{-1}$ for the long cycle, with a Coulomb efficiency of 99.8% after 100 cycles. Following MW-5 with a capacity of 65 $mAhg^{-1}$, while the remaining options have capacities of around 50 $mAhg^{-1}$. All of the samples exhibit a similar declining trend, although MW-5 and MW-2 have more capacity before reaching a rate of C/5. This indicates that enhancing the performance during the initial 20 cycles is crucial. In other words, it is necessary to figure out the method to suppress the damage by oxygen removal. In addition, the decrease in capacity can be attributed to many causes such as changes in microstructure, electrolyte decomposition at high potential, and impedance.[17,21]

The plots of differential capacity versus voltage (dQ/dV) for five samples are collected and displayed in Figure 4.3 c) and d). The oxidation reaction of the MW-Li_2NiO_3 cathodes exhibits two prominent peaks at approximately 4.6 and 4.7 V, which correspond to the release of O_2 in the form of Li_2O from the active material component or by proton exchange.[16,18] There are two oxidation peaks observed at 3.7 and 3.8 V during the first charge process, suggesting that the layered phase transforms to a spinel-like phase in the initial charge process.[22] Compared with MW-1, other 4 samples nearly exhibit no peaks at 3.7 and 3.8 V, indicating longer microwave

time at high power can partially prevent the loss of O_2. In this instance, MW-1exhibits a reduced Coulomb efficiency of just 35.5% due to the high charge capacity resulting from the loss of Li_2O while Ni occupies the Li vacancies. Consequently, there is a lower discharge capacity since not all of the Li has the ability to be reinserted after extraction. During the first discharge process, a significant reduction peak is observed at around 4.1 V. This peak is mostly caused by the creation of $LiNiO_2$ by the lithiation of layered NiO_2.[23] According to Fig4.3 e), the reduction of Ni^{4+} in the layered NiO_2 component that occurs originally at 4.1 V, while in the subsequent discharge, it shifts to lower potentials but the magnitude increases, corresponding to the characteristic of a lithium rich oxide spinel-like phase.[24]

It is determined that the decrease in capacity and voltage in Li_2NiO_3 during charge/discharge cycles is caused by the stable structure in the defect spinel phase. This structure prevents lithium reinsertion due to oxygen loss and structural reorganisation and is accompanied by the activation of lower valence Ni(Ni^{2+}/Ni^{3+}) redox.

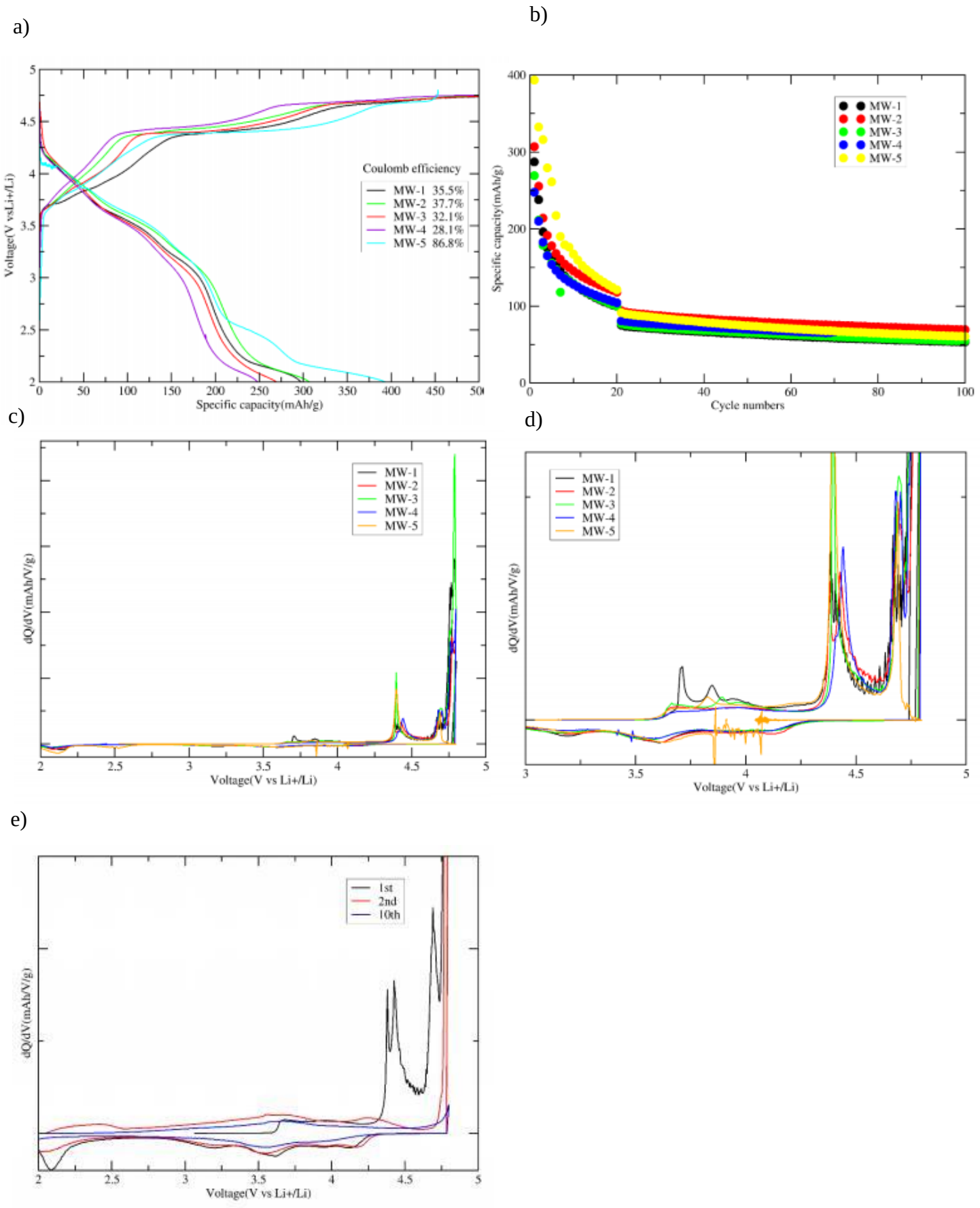

Fig4.4 The electrochemical performance of MW-Li_2NiO_3 made by five microwave times;(a) Charge/discharge voltage profiles of MW- Li_2NiO_3 electrodes; (b) Cycling performance; (c),

and (d) The differential capacity versus voltage(dQ/dV) curves of the MW-Li_2NiO_3 electrodes; (e) 1, 2, 10 cycles of dQ/dV for MW-2.

4.4 Conclusion and future works

Experimental results demonstrate a marginal increase in particle size following the microwave treatment, however, XRD patterns indicate that there has been no alteration in the phase. Microwaves inhibit or postpone the removal of oxygen from the electrode, particularly for MW-2 and MW-5, resulting in a higher capacity of 70 $mAhg^{-1}$ compared to the initial capacity of 57 $mAhg^{-1}$, representing ~ a 20% increase in capacity. Nevertheless, the phase shift remains present and the duration of microwave exposure is influenced by the air-sensitive nature of Li_2NiO_3. It is advisable to invest more effort in selecting the first electrode before commencing the microwave phase or consider enhancing the environment by conducting the microwave process under an oxygen gas atmosphere for future endeavours. Ultimately, the microwave method is effective for the monoclinic phase of Li_2NiO_3, and further investigation is warranted

Supporting information:

a)

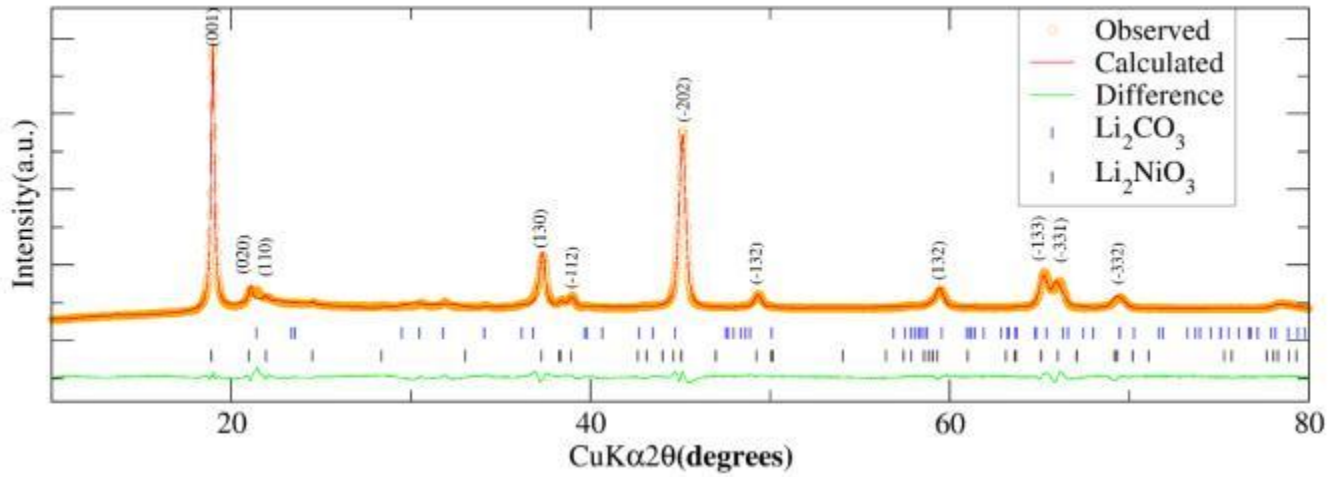

b)

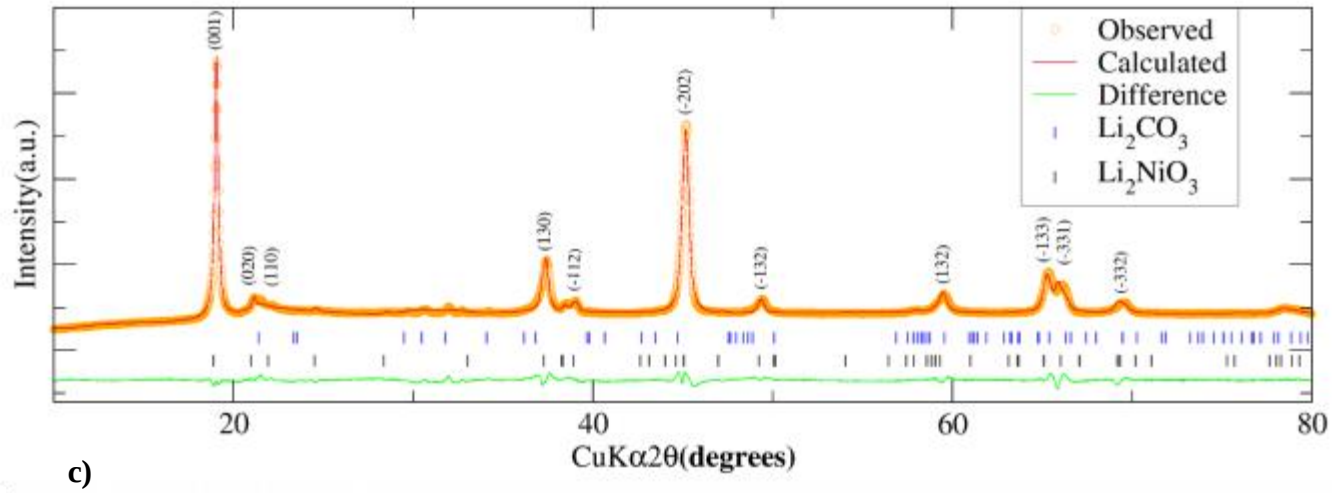

c)

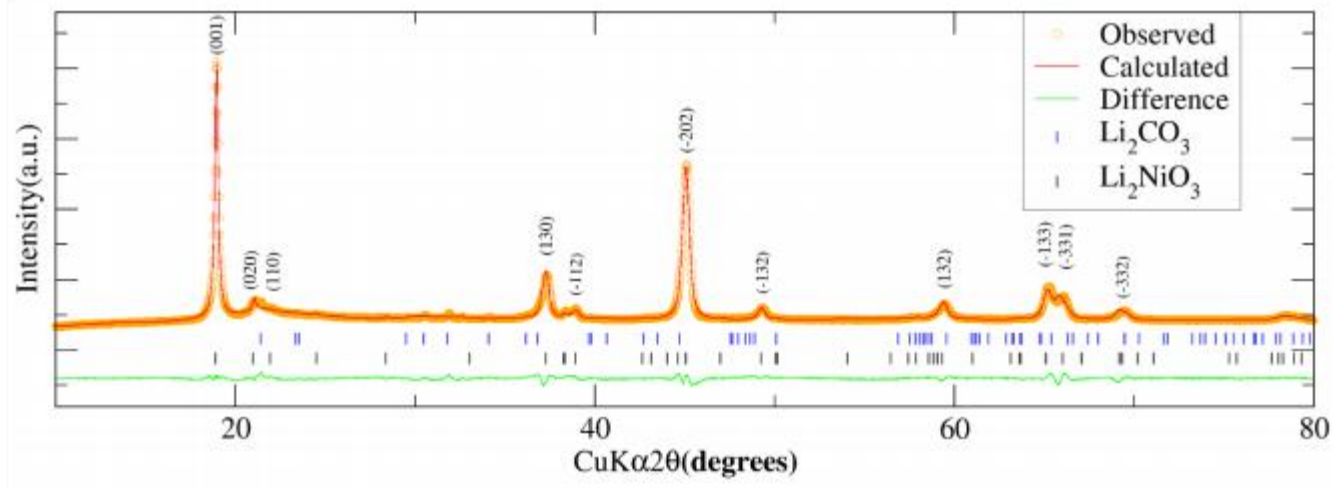

d)

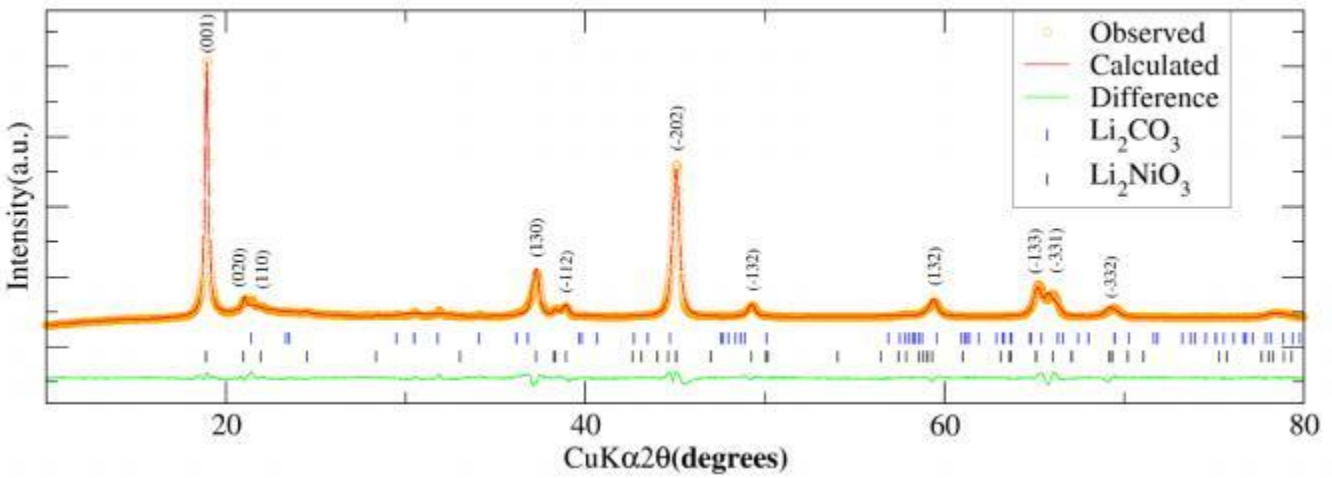

e)

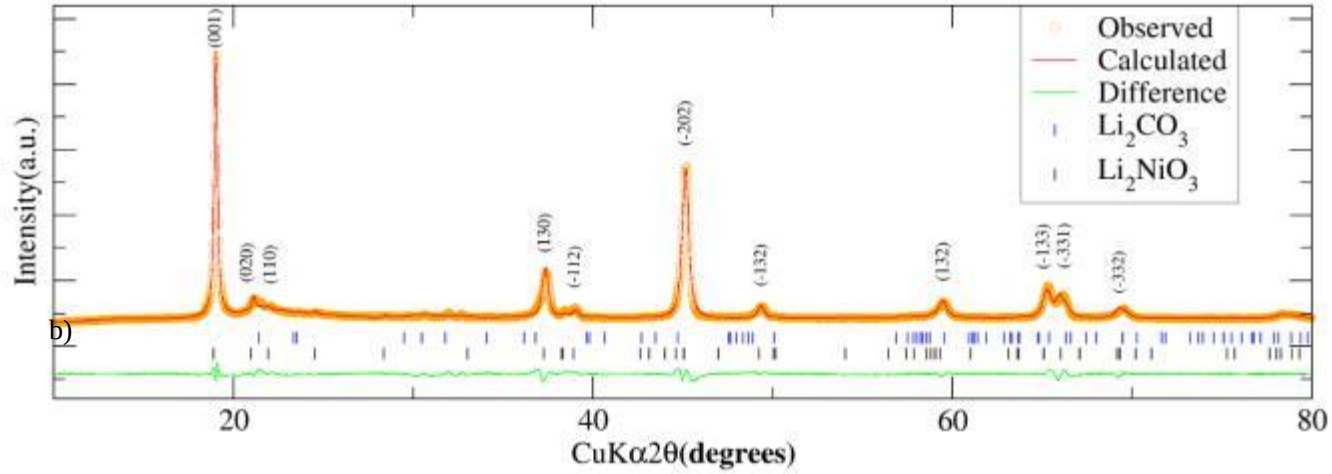

b)

FigS4.1 Rietveld refinements of lab PXRD data of MW- Li_2NiO_3 synthesised in condition a) MW-1, b) MW-2, c), MW-3, d) MW-4, e) MW-5. Orange dots represent observed data, red solid line is the calculated pattern and the green line represents the difference curve

Table S4.1

a) Lattice parameters and MW- Li_2NiO_3 phases

Sample	MW-1	MW-2	MW-3	MW-4	MW-5
a(Å)	4.921(5)	4.927(8)	4.927(1)	4.928(5)	4.922(5)
b(Å)	8.467(9)	8.473(2)	8.471(5)	8.471(1)	8.470(1)
c(Å)	4.981(1)	4.982(1)	4.981(1)	4.981(4)	4.981(2)
β (°)	109.22(5)	109.27(8)	109.24(9)	109.25(2)	109.24(3)
V($Å^{-3}$)	195.9(7)	196.3(4)	196.2(9)	196.3(4)	196.5(4)
R_{wp}	0.02913	0.02698	0.02874	0.03514	0.02864
X^2	7.31	4.65	3.58	2.879	3.265
I(110)/I(020)	0.83	0.85	0.77	0.73	0.76

b) Transition metal (Ni) occupancy(g) at each site and MW- Li_2NiO_3 calculated Ni per chemical formula

Sample	MW-1	MW-2	MW-3	MW-4	MW-5	Li_2NiO_3 standard
g_{4g}	0.714(6)	0.710(1)	0.700(6)	0.777(0)	0.7165(8)	0.78(2)
g_{2b}	0.612(6)	0.632(6)	0.633(2)	0.656(1)	0.572(5)	0.41(2)
g_{2c}	0	0	0	0	0	0
g_{4h}	0.086(1)	0.095(1)	0.061(0)	0.067(6)	0.025(3)	0.02(2)
g_{total}^a	0.738(6)	0.747(3)	0.718(6)	0.780(6)	0.684(6)	0.67(3)

g_{total}^a means transition metal (Ni) content per chemical fomula(1-x), calculated from equation $g_{total}=(2g_{4g}+g_{2b})/3+(g_{2c}+2g_{4h})/3$.[25]

References

(1) Mingos, D. M. P.; Baghurst, D. R. Tilden Lecture. Applications of Microwave Dielectric Heating Effects to Synthetic Problems in Chemistry. *Chem. Soc. Rev.* **1991**, 20 *(*1), 1. https://doi.org/10.1039/cs9912000001.

(2) Rao, K. J.; Ramakrishnan, P. A.; Gadagkar, R. Microwave Preparation of Oxide Bronzes. *J. Solid State Chem.* **1999**, *148* (1), 100-107. https://doi.org/10.1006/jssc.1999.8378.

(3) Singh, S.; Gupta, D.; Jain, V.; Sharma, A. Microwave Processing of Materials and Applications in Manufacturing Industries: A Review. *Mater. Manuf. Process.* **2014**, *IN PRESS*. https://doi.org/10.1080/10426914.2014.952028.

(4) Thostenson, E. T.; Chou, T.-W. Microwave Processing: Fundamentals and Applications. *Compos. Part Appl. Sci. Manuf.* **1999**, *30* (9), 1055-1071. https://doi.org/10.1016/S1359-835X(99)00020-2.

(5) Metaxas, A. Microwave Heating. *Power Eng. J.* **1991**, 5, 237 247.https://doi.org/10.1049/pe:19910047.

(6) Vaidhyanathan, B.; Rao, K. J. Synthesis of Ti, Ga, and V Nitrides: Microwave-Assisted Carbothermal Reduction and Nitridation. *Chem. Mater.* **1997**, *9* (5), 1196-1200. https://doi.org/10.1021/cm9605835.

(7) Baghurst, D. R.; Chippindale, A. M.; Mingos, D. M. P. Microwave Syntheses for Superconducting Ceramics. *Nature* **1988**, *332* (6162), 311-311. https://doi.org/10.1038/332311a0.

(8) Kladnig, W. F.; Horn, J. E. Submicron Oxide Powder Preparation by Microwave Processing. *Ceram.Int.* **1990**, *16* (2), 99-106. https://doi.org/10.1016/0272-8842(90)90079-U.

(9) Liu, Y.-F.; Liu, X.-Q.; Meng, G.-Y. A Novel Route of Synthesizing $La_{1-x}Sr_xCoO_3$ by Microwave Irradiation. Mater. Lett. **2001**, 48 (3–4), 176–183. https://doi.org/10.1016/S0167-577X(00)00299-8.

(10) Kalyani, P.; Kalaiselvi, N.; Renganathan, N. G. Microwave-Assisted Synthesis of $LiNiO_2$—a Preliminary Investigation. *J. Power Sources* **2003**, *123* (1), 53-60. https://doi.org/10.1016/S0378- 7753(03)00458-0.

(11) Miao, X.; Yan, Y.; Wang, C.; Cui, L.; Fang, J.; Yang, G. Optimal Microwave-Assisted Hydrothermal Synthesis of Nanosized $xLi_2MnO_3 \cdot (1 - X)LiNi_{1/3}Co_{1/3}Mn_{1/3}O_2$ Cathode Materials for Lithium Ion Battery. *J. Power Sources* **2014**, *247*, 219-227. https://doi.org/10.1016/j.jpowsour.2013.08.097.

(12) Fu, Z.; Chen, C. Synthesis and Preparation of Li_2MnO_3 Microwave Dielectric Ceramics.*Ferroelectrics*,**2023**,*606*(1), 80-86. https://doi.org/10.1080/00150193.2023.2189826.

(13) Bhat, M. H.; Chakravarthy, B. P.; Ramakrishnan, P. A.; Levasseur, A.; Rao, K. J. Microwave Synthesis of Electrode Materials for Lithium Batteries. *Bull. Mater. Sci.* **2000**, *23* (6), 461-466. https://doi.org/10.1007/BF02903884.

(14) Boulineau, A.; Croguennec, L.; Delmas, C.; Weill, F. Structure of Li_2MnO_3 with Different Degrees of Defects. *Solid State Ion.* **2010**, *180* (40), 1652-1659. https://doi.org/10.1016/j.ssi.2009.10.020.

(15) Bianchini, M.; Schiele, A.; Schweidler, S.; Sicolo, S.; Fauth, F.; Suard, E.; Indris, S.; Mazilkin, A.; Nagel, P.; Schuppler, S.; Merz, M.; Hartmann, P.; Brezesinski, T.; Janek, J. From $LiNiO_2$ to Li_2NiO_3 : Synthesis, Structures and Electrochemical Mechanisms in Li-Rich Nickel Oxides.*Chem.Mater.***2020**,*32* (21), 9211-9227. https://doi.org/10.1021/acs.chemmater.0c02880.

(16) Chen, H.; Islam, M. S. Lithium Extraction Mechanism in Li-Rich Li_2MnO_3 Involving Oxygen Hole Formation and Dimerization. *Chem. Mater.* **2016**, *28* (18), 6656-6663. https://doi.org/10.1021/acs.chemmater.6b02870.

(17) Shen, C.-H.; Wang, Q.; Fu, F.; Huang, L.; Lin, Z.; Shen, S.-Y.; Su, H.; Zheng, X.-M.; Xu, B.

B.; Li,J.T.; Sun, S.-G. Facile Synthesis of The Li-Rich Layered Oxide $Li_{1.23}Ni_{0.09}Co_{0.12}Mn_{0.56}O_2$ with Superior Lithium Storage Performance and New Insights into Structural Transformation of the Layered Oxide Material during Charge-Discharge Cycle: In Situ XRD Characterization. ACS Appl. Mater.Interfaces 2014, 6 (8), 5516–5524. https://doi.org/10.1021/am405844b.

(18) Robertson, A. D.; Bruce, P. G. Mechanism of Electrochemical Activity in Li_2MnO_3. *Chem. Mater.* **2003**, *15* (10), 1984–1992. https://doi.org/10.1021/cm030047u.

(19) Ju, S. H.; Kim, D.-W. Effect of Calcination Temperature on the Structure and Electrochemical Performance of $LiMn_{1.5}Ni_{0.5}O_4$ Cathode Materials. *Bull. Korean Chem. Soc.* **2013**, *34*. https://doi.org/10.5012/bkcs.2013.34.1.59.

(20) Mohanty, D.; Kalnaus, S.; Meisner, R. A.; Safat, A. S.; Li, J.; Payzant, E. A.; Rhodes, K.; David L. Wood, I. I. I.; Daniel, C. Structural Transformation in a $Li_{1.2}Co_{0.1}Mn_{0.55}Ni_{0.15}O_2$ L ithium-Ion Battery Cathode during High-Voltage Hold. *RSC Adv.* **2013**, *3* (20), 7479–7485. https://doi.org/10.1039/C3RA40510A.

(21) Wu, Y.; Manthiram, A. Effect of Surface Modifications on the Layered Solid Solution Cathodes $(1-z)\,Li[Li_{1/3}Mn_{2/3}]O_2-(z)Li[Mn_{0.5-y}Ni_{0.5-y}Co_{2y}]O_2$. *Solid State Ion.* **2009**, *180* (1), 50–56. https://doi.org/10.1016/j.ssi.2008.11.002.

(22) Reimers, J. N.; Fuller, E. W.; Rossen, E.; Dahn, J. R. Synthesis and Electrochemical Studies of $LiMnO_2$ Prepared at Low Temperatures. *J. Electrochem. Soc.* **1993**, *140* (12), 3396. https://doi.org/10.1149/1.2221101.

(23) Croy, J. R.; Kim, D.; Balasubramanian, M.; Gallagher, K.; Kang, S.-H.; Thackeray, M. M. Countering the Voltage Decay in High Capacity $xLi_2MnO_3 \bullet (1-x)LiMO_2$ Electrodes (M= Mn ,Ni, Co) for Li^+ - Ion Batteries. *J. Electrochem. Soc.* **2012**, *159* (6), A781–A790. https://doi.org/10.1149/2.080206jes.

(24) Xiang, Y.; Wu, X. Enhanced Electrochemical Performances of Li_2MnO_3 Cathode Materials by Al Doping. *Ionics* **2018**, *24* (1), 83–89. https://doi.org/10.1007/s11581-017-2189-4.

(25) Tabuchi, M.; Kuriyama, N.; Takamori, K.; Imanari, Y.; Nakane, K. Appearance of Lithium-Excess $LiNiO_2$ with High Cyclability Synthesized by Thermal Decomposition Route from $LiNiO_2$ - Li_2NiO Solid Solution. J. Electrochem. Soc. 2016, 163 (10), A2312 A2317.https://doi.org/10.1149/2.0861610jes.

Chapter 5
Conclusions and Future Work

5.1 Conclusions

We have employed a solid-state technique to synthesise a Li-rich, Ni-rich cathode material known as Li_2NiO_3. Besides, this study thoroughly examined the impact of the synthesis conditions on the performance of Li_2NiO_3. The influence of precursor selection, lithium excess, cooling/heating rate, and calcination temperature on the electrochemical performance was examined. It was established that the calcination temperature had the most significant effect. The advanced method for manufacturing Li_2NiO_3 involves synthesising the materials under certain conditions: preheating at 300°C for 12 hours and then at 550°C for 24 hours, with a heating/cooling rate of 3°C/min; Additionally, a low concentration NH_3 precursor is used, with a 3% excess of Li. A combination of XRD, SEM and electrochemical performance was employed to validate the conditions required. Extreme temperatures can cause phase transformations.

Furthermore, the addition of microwaves during sysnthesis has been utilised and shown to enhance the sample to achieve a 20% improvement in capacity after 100 cycles.

This study demonstrates additional characteristics of Li_2NiO_3 and provides evidence that the calcination temperature not only enhances the crystallinity but also expedites the phase transformation. This study utilises a combination of solid- state synthesis and microwave techniques to demonstrate that microwaves can stimulate the activity and enhance the capacity of Li_2NiO_3. Although this work offers preliminary findings on a new technique of synthesis, it is crucial to carry out additional research to ascertain the most favourable synthesis conditions in terms of cost, safety, and electrochemical performance.

5.2 Future Works

Li_2NiO_3 undergoes a phase change at high temperatures, although the redox mechanism remains unknown. The utilisation of XAS, XPS, and RIXS techniques is recommended to investigate the O_2 oxidation process during both charge and discharge.

To enhance the structural stability and electrochemical performance of Li_2NiO_3, a Li-rich layered oxide analogous to Li_2MnO_3, cation doping has been extensively investigated. Inspired by the beneficial effects observed in Li_2MnO_3, doping strategies involving Mg^{2+}, Al^{3+}, Ti^{4+}, and Zr^{4+} ions have been considered for Li_2NiO_3 to suppress irreversible oxygen release, stabilize the layered structure, and inhibit transition metal migration. For instance, Mg doping in Li_2MnO_3 has been shown to significantly reduce oxygen evolution and Mn migration, contributing to enhanced structural stability during cycling.[1] Zr^{4+} doping into Ni-rich layered oxides, including those structurally similar to Li_2NiO_3, improves the cycling performance by acting as a pillar ion that enhances the interlayer spacing and suppresses phase transitions.[2] Ti^{4+} and Al^{3+} doping have also been employed to suppress oxygen vacancy formation and improve rate performance by enhancing lithium diffusion kinetics and electronic conductivity.[3-4] These insights suggest that similar multivalent doping strategies could be effectively extended to Li_2NiO_3 to mitigate its structural degradation during electrochemical cycling.

In addition to doping, surface coating has proven to be an effective method for further improving the interfacial stability of Li-rich materials. Coating techniques such as wet-chemical methods, sol–gel, and atomic layer deposition (ALD) are widely used. For example, ultrathin Al_2O_3 coatings applied via ALD or sol–gel processes provide conformal, nanometer-thick films that suppress surface side reactions and improve capacity retention.[5] TiO_2-coated Li_2MnO_3 electrodes demonstrated reduced charge-transfer resistance and improved cycling stability by mitigating Mn dissolution and surface reconstruction.[6] Furthermore, amorphous Li–Zr–O coatings on high-Ni cathodes have shown the ability to enhance interfacial stability and lithium-ion transport, while

suppressing parasitic reactions and metal ion dissolution.[7] These coating strategies are promising for application in Li_2NiO_3, offering a synergistic approach with doping to enhance its practical applicability in high-energy-density lithium-ion batteries.

In summary, our future work will focus on optimizing Li-rich Ni-based oxides through synergistic doping and coating modifications, coupled with comprehensive characterization techniques including XPS, HRTEM, EIS, and ICP-OES.

Reference

(1) Luo, C.; Hu, E.; Jiang, Y.; Zhang, L.; Zhao, Q.; Yu, X.; Li, H.; Yang, X.-Q. Stabilization of Li_2MnO_3 Phase by Mg Doping Suppressing Irreversible Oxygen Loss and Mn Ions Migration. J. Mater. Sci. Technol. **2023**, 157, 93–102. https://doi.org/10.1016/j.jmst.2023.03.040.

(2) Xu, Y. N.; Zhang, C. Y.; Yu, H.; Fu, R. H.; Zhao, Y. F. Understanding the Role of Zr^{4+} Cation in Improving the Cycleability of $LiNi_{0.8}Co_{0.15}Zr_{0.05}O_2$ Cathodes for Li Ion Rechargeable Batteries. J. Alloys Compd. **2009,** 478 (1–2), 370–373. https://doi.org/10.1016/j.jallcom.2008.12.129.

(3) Bai, J.; Yuan, X.; Wang, Q.; Sun, Y.; Gao, S. Doping Strategies for Stabilizing Lithium-Rich Layered Oxides: A Review. J. Energy Chem. **2022**, 71, 139–158. https://doi.org/10.1016/j.jechem.2022.03.042.

(4) Wang, L.; Yu, Y.; Chen, D.; Zhou, J.; Wang, Y.; Sun, Y. Effects of Al and Ti Co-Doping on the Structure and Electrochemical Properties of Li_2MnO_3-Based Cathode Materials. J. Alloys Compd. **2023**, 969, 172659. https://doi.org/10.1016/j.jallcom.2023.172659.

(5) Kim, D.; Mohanty, D.; Payzant, E. A.; Huq, A.; Wood, D. L.; Daniel, C. Ultra-thin Al_2O_3 Coating on the Acid-Treated $0.3Li_2MnO_3{\cdot}0.7LiMn_{0.60}Ni_{0.25}Co_{0.15}O_2$ Electrode for Li-ion Batteries. J. Alloys Compd. **2014**, 615, 972–978. https://doi.org/10.1016/j.jallcom.2014.07.204.

(6) Zhang, X.; Zhao, Y.; Ren, D.; Han, C.; Li, X.; Qiu, X. Highly Stable TiO_2 Coated Li_2MnO_3 Cathode Materials for Lithium-Ion Batteries. J. Power Sources **2016**, 302, 67–73. https://doi.org/10.1016/j.jpowsour.2015.10.103.

(7) Zheng, J.; Yan, P.; Mei, D.; Estevez, L.; Wang, C.; Zhang, J.-G.; Xu, W. Amorphous Li–Zr–O Layer Coating on the Surface of High-Ni Cathode Materials for Lithium Ion Batteries. Electrochim. Acta **2018**, 268, 297–305. https://doi.org/10.1016/j.electacta.2018.02.090.